

QUANTIFYING VOLUMETRIC DISTRIBUTION OF FUEL MASS IN A TRANSIENT  
HIGH PRESSURE REACTING SPRAY VIA THE APPLICATION OF RAINBOW  
SCHLIEREN DEFLECTOMETRY

by

ROSS THOMAS DEPPERSCHMIDT

JOSHUA A. BITTLE, COMMITTEE CHAIR  
AJAY K. AGRAWAL  
CHIH-HSIUNG CHENG

A THESIS

Submitted in partial fulfillment of the requirements  
for the degree of Master of Science  
in the Department of Mechanical Engineering  
in the Graduate School of  
The University of Alabama

TUSCALOOSA, ALABAMA

2019

Copyright Ross Thomas Depperschmidt 2019  
ALL RIGHTS RESERVED

## ABSTRACT

The fuel atomization, evaporation and subsequent mixing process with ambient air during fuel injection in a direct injection internal combustion (IC) engine are crucial to subsequent combustion and engine performance. Optimization of the fuel injection mechanism has been continuously explored with the advancement of the IC engine. This is especially true regarding direct injection involved with diesel engines where there is very minimal time for the fuel and compressed air to mix. With accumulative precedence being placed on increasing fuel efficiency and decreasing toxic emissions such as nitric oxides and carbon monoxides, research has been focused on ensuring the combustion processes comply with government or otherwise issued regulations. In order to investigate the intricate physical phenomena following the start of injection (SOI) that dictate how eventual combustion occurs, local quantitative characterization of the spray is necessary.

In this thesis, the Rainbow Schlieren Deflectometry (RSD) technique is employed to provide local quantitative measurements during the transient fuel-air mixing process by examining a reacting n-heptane fuel spray injected into ambient air at 28 bar and 825 K. An optically accessible constant pressure flow vessel (CPFV) and common rail diesel injector allows for the capturing of high-speed, instantaneous RSD images and subsequent ensemble averaging of the data for repeated injections in immediate succession. From this, the average mixture temperature and equivalence ratio distribution downstream of the liquid length are determined

for the entire radial span of the spray, along with the liquid and vapor boundaries. The two-dimensional spray data is then converted into a spray volume and the low temperature heat release (LTHR) region is identified. Next, the fuel mass distribution is obtained in this LTHR region with a corresponding mixture temperature and equivalence ratio. The adiabatic flame temperatures in the LTHR region are calculated by a chemical equilibrium solver via ANSYS Chemkin. Experimental results reveal local equivalence ratio, temperature, and fuel mass distributions for the entire spray volume downstream of the liquid length, along with quantification of the conditions of the mixture in the region that ultimately exhibits low temperature heat release prior to and during the main ignition event.

## LIST OF ABBREVIATIONS AND SYMBOLS

aSOI	After Start of Injection
CI	Compression Ignition
CDAQ	Control and Data Acquisition
CPFV	Constant Pressure Flow Vessel
D	Diameter
EGR	Exhaust-Gas Recirculation
EOI	End of Injection
HSI	Hue, Saturation, and Intensity
IC	Internal Combustion
LEA	Laser Extinction/Absorption
LED	Light Emitting Diode
LIEF	Laser Induced Exciplex Fluorescence
LIF	Laser Induced Fluorescence
LRS	Laser Rayleigh Scattering
LTC	Low Temperature Combustion
LTHR	Low Temperature Heat Release
RGB	Red, Green, and Blue
RSD	Rainbow Schlieren Deflectometry
SOI	Start of Injection
SRS	Spontaneous Raman Scattering

$\lambda$       Wavelength

$\phi$       Equivalence ratio

## ACKNOWLEDGMENTS

The University of Alabama has provided me with invaluable opportunities in pursuing both my undergraduate and Masters degree, and for that I am extremely grateful. Thank you to my committee members, Dr. Agrawal, Dr. Bittle, and Dr. Cheng for their time and teachings, without which I would not be in the position I am today. I would like to especially express my gratitude to Dr. Bittle, who has been exceedingly helpful and instrumental in my development as a graduate student and overall person during my time here. It was a blessing having him take me on as a research assistant, and this would not have been possible without his influential guidance the last few years.

Through a challenging curriculum and a demanding research position, the support of friends and family helped me through it all. Thank you to my mom and dad, Noelle and Joel Depperschmidt, and my brother Danny who has been here with me every step along the way. To all the other research assistants under Dr. Agrawal and in the graduate office: Yasin Gokmen, Zach Harris, Mitch Johnson, John Kornegay, Allen Loper, Rob Miller, Shawn Reggeti, Eric Schultz, Jonathan Tobias, Nathan Vardaman, Taber Wanstall, and Cooper Welch, thank you all for creating a positive work environment and for memories I will forever cherish.

Lastly, I'd like to recognize all the people behind the scenes who make our lives easier as graduate students. Betsy Singleton, Lisa Hinton, and Lynn Hamric in the mechanical engineering

office, as well as all the machine shop employees, have offered great assistance and understanding as they're patience is tested daily with the amount of responsibilities on their plates. While my time at the University of Alabama was a rewarding one in many aspects, I look forward to applying what I've learned here to the next chapter in my life. Roll Tide!

## CONTENTS

ABSTRACT .....	ii
LIST OF ABBREVIATIONS AND SYMBOLS .....	iv
ACKNOWLEDGMENTS .....	vi
LIST OF TABLES .....	x
LIST OF FIGURES .....	xi
CHAPTER 1 INTRODUCTION .....	1
1.1 Motivation .....	1
1.2 Previous Related Work .....	2
1.3 Previous Rainbow Schlieren Work .....	8
CHAPTER 2 EXPERIMENTAL SETUP .....	19
2.1 Constant Pressure Flow Vessel (CPFV) .....	19
2.2 Experimental Procedure .....	19
2.3 Optical System .....	22
2.4 Hue, Saturation and Intensity (HSI) Model .....	26
2.5 Rainbow Schlieren Deflectometry Analysis Procedure .....	27
2.6 Projected Three-Dimensional Fuel Mass Calculations.....	34
CHAPTER 3 EXPERIMENTAL RESULTS AND DISCUSSION .....	42
3.1 Overview .....	42
3.2 Spray Evolution .....	43
3.3 Transient Fuel-Air Mixing .....	45

3.4 Fuel Mass Analysis Procedure .....	46
3.5 Low Temperature Heat Release Zone Analysis Procedure .....	48
3.6 Fuel Mass Measurements .....	50
CHAPTER 4 CONCLUSIONS AND RECOMENDATIONS .....	67
REFERENCES .....	70
APPENDIX A .....	73
APPENDIX B .....	79
APPENDIX C .....	86
APPENDIX D .....	93
APPENDIX E .....	100

## LIST OF TABLES

<i>Table 2.1</i>	Fuel properties of n-heptane. ....	21
<i>Table 2.2</i>	Fuel injector specifications. ....	21
<i>Table 3.1</i>	Test conditions. ....	43

## LIST OF FIGURES

<i>Figure 1.1</i>	Illustration of fluid mixing mechanisms during fuel injection process.....	11
<i>Figure 1.2</i>	Visualization of a diesel injection using Mie-scatter (left) and laser Rayleigh scattering (right) to detect the liquid and vapor portions of the spray, respectively [10]. .....	12
<i>Figure 1.3</i>	Schematics of the optical arrangements for the shadowgraphy (left) and traditional schlieren (right) techniques [5]. .....	12
<i>Figure 1.4</i>	Mie-scattered images superimposed on schlieren images for qualitative analysis at various ambient gas densities [6]. .....	13
<i>Figure 1.5</i>	Representation of idealized diesel jet model for Siebers’s scaling law [7]. .....	13
<i>Figure 1.6</i>	Representation of transient idealized diesel jet model developed by Musculus and Kattke [8]. .....	14
<i>Figure 1.7</i>	Transient jet model predictions compared with experimental results of mixture fractions along the centerline (top) and radial profiles at axial locations of 25 mm and 45 mm (bottom) found by Pickett et al. [9]. .....	14
<i>Figure 1.8</i>	Mean fuel-to-ambient number density contours for a transient fuel spray [10]. Quantitative data acquired via Laser Rayleigh Scattering (LRS) technique by Pickett et al. ....	15
<i>Figure 1.9</i>	Mie-scatter and soot luminosity (left) coupled with shadowgraph technique (right) employed to characterize a reacting transient fuel injection [12]. The “cool-flame” region of the jet is noticeable as the liquid length outlined by mie-scatter recognition recedes in antecedent frames to combustion occurring. ....	16
<i>Figure 1.10</i>	Amount of fuel mass present at corresponding equivalence ratios in fuel spray for different levels of oxygen in the ambient air [13]. .....	17
<i>Figure 1.11</i>	Traditional schlieren (left) and rainbow schlieren (right) images of a stable acetylene flame obtained by Howes et al. [16]. .....	17
<i>Figure 1.12</i>	Image of the first rainbow schlieren continuous spectrum color filter for quantitative measurements employed by Greenberg et al. [17] .....	18
<i>Figure 2.1</i>	Constant pressure flow vessel (CPFV) illustration. ....	36
<i>Figure 2.2</i>	Schematic of experimental apparatus (not to scale). .....	37
<i>Figure 2.3</i>	Schematic of light collection system on the collimating side of the RSD apparatus (not to scale). .....	37
<i>Figure 2.4</i>	Schematic of RSD optical configuration (not to scale). .....	38

<i>Figure 2.5</i>	Symmetric rainbow filter.....	38
<i>Figure 2.6</i>	Rainbow filter calibration curve with hue range from 20° to 300°. Error bars represent a $\pm 2\sigma$ deviation in the 100x100 pixel imaging region. ....	39
<i>Figure 2.7</i>	Hue color wheel with corresponding values [28] .....	39
<i>Figure 2.8</i>	Visual representation of Hue, Saturation, and Intensity color model [27].....	40
<i>Figure 2.9</i>	Illustration (not to scale) of a deflected light ray transversely displaced on color filter. Solid red line represents a light ray deflected by the test media whereas the dashed red line represents the path of an undeflected light ray crossing the center of the color filter. ....	40
<i>Figure 2.10</i>	Geometrical representation of a deflected light ray passing through an axisymmetric inhomogeneous refractive index field of radius $r$ . Light rays are deflected in the transverse or $x$ direction at an angle $\varepsilon(x_i)$ based on the refractive index difference $\delta(r_i)$ of the path the rays pass through. ....	41
<i>Figure 2.11</i>	Equilibrium thermodynamic mixing relating the normalized refractive index difference to equivalence ratio and mixture temperature. ....	41
<i>Figure 3.1</i>	Effect of amount of image samples on average deflection angle at specific locations. ....	59
<i>Figure 3.2</i>	Instantaneous RSD images tracking the spray evolution from five separate fuel injections for comparison. ....	60
<i>Figure 3.3</i>	Instantaneous RSD images illustrating the spray evolution for a single injection, displaying the measured hue as color. The raw images (left) and the images with maximized intensity and saturation values (right) are shown for visual comparison. For each image the injector (left) and thermocouple (top-left) are blacked-out.....	61
<i>Figure 3.4</i>	Equivalence ratio (left) and temperature (right) contours of jet evolution up to maximum penetration (0.75 ms aSOI) and for the LTHR zone .....	62
<i>Figure 3.5</i>	Example of liquid boundary detection using relative intensity threshold procedure [26] .....	62
<i>Figure 3.6</i>	Fuel mass present at corresponding equivalence ratios for different time steps of the spray evolution. ....	63
<i>Figure 3.7</i>	Contour map relating the amount of relative fuel mass concentration to equivalence ratio and mixture temperature (K) at different time steps in the spray evolution....	64
<i>Figure 3.8</i>	Contour plot relating the relative fuel mass concentration to equivalence ratio and mixture temperature (K) in the LTHR zone. Pre-ignition (left) refers to the calculated fuel mass in the LTHR zone and post-ignition represents the adiabatic flame temperature results via ANSYS Chemkin. ....	65
<i>Figure 3.9</i>	Instantaneous optical images of flame combustion and flame propagation at similar experimental conditions: <i>n</i> -heptane injected into 33 bar, 785K air .....	66

# CHAPTER 1

## INTRODUCTION

### 1.1 Motivation

The significance placed on emission regulations, societal need for energy, and limited available natural resources has led the combustion and engine community to focus its research on making reacting fuel sprays more energy efficient and environmentally friendly. Based on these efforts, diesel engines are becoming a more viable option in comparison to traditional gasoline engines because they operate at higher compression ratios (14:1 to 25:1) than gasoline engines (8:1 to 12:1), resulting in better overall thermal efficiency. While this is beneficial in increasing fuel efficiency, diesel engines are also prone to producing higher levels of toxic emissions such as nitric oxides ( $\text{NO}_x$ ), soot and other particulates, unburned hydrocarbons (UHC), and carbon monoxide (CO) without the ability to use a three-way catalytic converter as in a stoichiometrically operated gasoline engines. The result is the need for costly aftertreatment systems on diesel engines to bring the emissions levels to acceptably low levels. Thus, an even better understanding of what is occurring at a fundamental level during diesel fuel injection is necessary to continue optimizing this process.

The importance of optical diagnostic techniques comes to the forefront in efforts to capture the fluid behavior during the pre-ignition fuel and air mixing process. Even more so, the ability to identify and measure local properties of the heterogeneous combustion process involved in a compression ignition (CI) engine is required to expand our knowledge of how the mixture will

eventually react. The complex fuel injection process, illustrated graphically in Figure 1.1, includes cavitation inside the injector, primary breakup after the fuel leaves the injector, atomization, secondary breakup, vaporization, fuel and air mixing, and eventual ignition occurring in the span of less than a millisecond and over only a few centimeters. Therefore, in order to study these processes experimentally, high-speed imaging capabilities with sufficient temporal and spatial resolution is required to capture these transient developments in order to enable the future development of better controls and designs of future injection systems. Much of the current and past diagnostic techniques investigating the transient fuel injection process have been limited by cross sensitivity in portions of the spray containing both liquid and vapor phases. This is problematic for attempts to obtain accurate quantitative local measurements in these regions of the fuel spray. The Rainbow Schlieren Deflectometry (RSD) technique applied in this study permits quantitative measurements of the mixing regions near the liquid core of the spray due to its lack of cross sensitivity problems.

## 1.2 Previous Related Work

Various optical diagnostic techniques have been employed in previous work to observe and quantify what is occurring throughout the transient fuel injection process. These diagnostics and associated modeling efforts have led to the conceptual picture shown in Figure 1.1. The complex heterogeneous in-cylinder combustion processes consisting of fuel injection, entrainment and mixing with the ambient air, atomization and vaporization of the injected fuel, and eventual autoignition and combustion involved in CI of diesel sprays makes it difficult to precisely apprehend the fluid behavior.

Mie-scattering refers to the elastic scattering of light as it interacts with a substance that has a diameter that is the same or greater than the wavelength of the incident light (i.e. liquid droplets).

Laser Rayleigh scattering (LRS), also elastic, involves the scattering of light of from gaseous molecules with diameters much smaller than the wavelength of the incident light ( $d/\lambda < 0.1$ ). One major difference between the two techniques is that Mie-scattering is not sensitive to incident wavelength of light whereas LRS is. Experiments for Mie-scattering and LRS are conducted by forming a thin laser sheet at the plane of interest (centerline of the injector for most fuel spray scenarios) via the laser source output, with respective wavelengths for each diagnostic technique, and a combination of lenses described by Davy and Williams [1]. The camera then captures images perpendicular to the laser sheet plane to detect the orthogonally scattered light. The scattering occurs due to molecular dipole moments oscillating once excited by the incident light [2]. Since there is no net energy exchange between the incident light and the particles, the incident light has the same wavelength as the scattered light [3]. LRS is able to identify the gas density and therefore fuel concentration because the scattered light intensity is proportional to the number density of gas molecules [4]. While LRS is a strong form of molecular light scattering and is well suited for density measurements at low gas densities, it also has drawbacks. Since both LRS and Mie-scattering are elastic processes, they are not species-specific and require essentially a particle-free environment to avoid laser light interference [4]. Figure 1.2 illustrates qualitative images of these diagnostic techniques.

Shadowgraphy and traditional schlieren are both line-of-sight integrating optical systems that traditionally use a pinhole aperture to project qualitative images of the test media data onto a focal plane of some sort. Both of these techniques decipher the vaporized fuel boundary from the ambient gas background in diesel fuel injection applications. Shadowgraphy projects a shadow caused by the displacement light rays experience due to deflections from inhomogeneities in the test media onto a screen [5]. With no test media present, the focal screen would be consistently

illuminated with the collimated light from the aperture. However as light rays travel through a test media comprised of varying refractive indices than the ambient gas, they are bent, refracted or overlapped leaving parts of the screen more or less illuminated.

Schlieren projects a coupled optical image of the test media formed by a lens combination and requires a cutoff or “stop” (traditionally a knife edge) to block some of the light rays that were deflected in response to the refractive index of the test media [5]. With no test media present in the path of the collimated light rays, the undeflected light rays will travel to the decollimating lens undisturbed and be focused on top of each other at the focal plane. Deflected light rays will be focused at positions displaced both axially and transversely at the focal plane. The knife edge placed at the focal plane is initially arranged to block half of the focused light intensity as just before the knife edge when there is no test media present. When the light rays are deflected as they pass through the test media and projected at different locations on the focal plane, it allows for the difference in light intensity at each location in the test media to be measured. However, the diminishment in light intensity at the focal plane cannot be assumed to be solely due to the knife edge blockage as there is absorption, reflection and scattering of light as the rays pass through the test media. The traditional schlieren method is therefore, like shadowgraphy, limited to a being qualitative diagnostic technique. The schematic in Figure 1.3 illustrates optical arrangements of each of these diagnostic techniques.

Other techniques used for measuring local fuel vapor concentrations include spontaneous Raman scattering (SRS) and Laser induced fluorescence (LIF). SRS involves the inelastic exchange of energy between photons and scattering molecules, however is inhibited by having a weak signal-to-noise ratio. LIF is an electronic emission and absorption process in which the fluorescence intensity measurement produced can be directly proportional to molecular

concentration. These fluorescent signal intensities can be easily impacted by the quenching common in inelastic collisions though, making it difficult to acquire quantitative measurements [4]. Laser induced exciplex fluorescence (LIEF) and Laser extinction/absorption (LEA) have the ability to decipher between liquid and vapor states in order to visualize fuel atomization and vaporization. However, LIEF faces drawbacks of quenching issues and the inability to determine droplet size, and LEA experiences troublesome sensitivity complications with dual wavelength lasers [4].

Increased understanding of the role that mixture formation embodies in governing the ensuing combustion process and pollutant production in IC engines has provided applications for these optical diagnostic techniques. Accurate characterization of the in-cylinder mixing behavior allows for model generation, with which results can be predicted based on test parameters and subsequent experiments can be manipulated to optimize the injection process. Some of the influential models describing mixture behavior, achieved through application of the previously detailed optical diagnostic techniques, are discussed next along with what analyses were made possible through the implementation of the injection characterization process.

Siebers applied Mie-scattering [6] for liquid droplet illumination along with the traditional schlieren technique to illustrate the effects that certain parameters have on the spray spreading angle and steady-state liquid length of an evaporating spray, as well as air entrainment controlling vaporization in a diesel spray. Qualitative results of his experiments are shown in Figure 1.4 as superimposition is employed to display time-averaged schlieren and Mie-scatter images for sprays at various ambient gas densities. Compounding on this work, Siebers then developed a liquid length scaling law for idealized diesel sprays by incorporating the principles of conservation of mass, energy and momentum [7]. Although there are simplifications and

assumptions made in this steady-state one-dimensional idealized model, such as the flow being locally homogeneous, it being valid only for single-component fuels, and perfect mixing occurring within the spray boundaries, it is able to accurately predict liquid length and the effects that altering certain parameters have on it. Figure 1.5 displays a schematic of the model Siebers employed in producing the liquid length scaling law.

Musculus and Kattke [8] expanded on the one-dimensional diesel jet model by accounting for jet velocity varying with time at any axial location to capture the fluid behavior during unsteady injections. In order to do this the Siebers model spray domain was axially discretized into control volumes and transient relations were applied for fuel mass transport and jet momentum for each control volume. A schematic of the one-dimensional discretized transient jet model is shown in Figure 1.6. With the added element of transient analysis, Musculus and Kattke were able to confirm observations made in experiments of an apparent entrainment wave occurring after the end of injection. During this wave after end of injection, the entrainment rate of the ambient gas increase by nearly a factor of three after end of injection (EOI), adding insight to the importance of the role entrainment plays in creating leaner mixtures for combustion if autoignition can be delayed until after EOI.

Pickett et al. tested the Musculus and Kattke variable radial profile model (shown in Figure 1.6) by comparing the model predictions of mixture fractions to ensemble averaged experimental results obtained through the usage of LRS [9]. They were able to tune the model to give good agreement with the experimental results over a range of ambient and fuel densities, injection pressures, nozzle dimensions, and fuel types. The model accounting for the entrainment effect based on penetration distance proved to incorporate valid physical relations when determining the fuel-air mixing during diesel injection. An example of the model prediction to

experimental results comparison is displayed in Figure 1.7, with the model prediction falling between the experimental uncertainty of the ensemble averaged data at the spray centerline and other radial locations. Pickett [10] had previously justified the experimental procedure of LRS to gather transient quantitative fuel concentration measurements in diesel spray through simultaneous Rayleigh intensity analysis of both the ambient and diesel jet (results in Figure 1.8). He also performed qualitative analysis in combining the usage of Mie-scattering with Shadowgraphy [11] to show the impact of early-injection low temperature combustion (LTC) strategies and the effect on maximum liquid penetration distance. The Mie-scatter and shadowgraph imaging techniques were then coupled with chemiluminescence imaging and jet luminosity measurements by photodiode to spatially and temporally characterize a developing reacting and non-reacting diesel spray [12]. Through this study, Pickett et al. provided image background correction to account for undesirable ambient gas refractive index variations unrelated to the injection process, identified cool-flame (or pre-ignition) regions in which the jet visually disappears due to heat release during fuel breakdown to the point that it matches the refractive index of the ambient gas, and located high-temperature combustion products along with soot formation. Results can be seen in Figure 1.9.

In an investigation of the effects that exhaust-gas recirculation (EGR) has on combustion emissions in a diesel engine, Pickett and Idicheria sought to obtain a more realistic assessment of the spray by applying the two-dimensional data from LRS to a three-dimensional model [13]. An axisymmetric assumption allowed for the top and bottom portions of the spray to each be converted into a jet volume via a  $180^\circ$  sweep about the centerline downstream of the lift-off length. The fuel mass for corresponding equivalence ratios was then calculated using the ideal gas law at each pixel location and the information was accumulated to create a histogram to more

accurately characterize the amount of fuel in the premixed ignition region. Results from their findings at different EGR levels are shown in Figure 1.10.

An analysis similar to what Pickett and Idicheria utilized is employed in this study from acquired Rainbow Schlieren Deflectometry measurements. The vapor portion of the fuel-air jet is identified downstream of the liquid length throughout the injection evolution and is projected into a jet volume on a pixel by pixel basis. Ensemble-averaged data for each pixel location in the RSD images is purposed to calculate fuel mass distribution throughout the vapor jet. This fuel mass distribution is then related to equivalence ratios and mixture temperatures to characterize the transient fuel mixing process, and adiabatic flame temperatures are computed based on the jet data via ANSYS Chemkin equilibrium solver. The details of this diagnostics, experimental setup, and data processing algorithms are presented in the next sections. This is followed by results and discussion before conclusions and future work complete this thesis document.

### 1.3 Previous Rainbow Schlieren Work

The aforementioned optical diagnostic techniques entail some of the advanced past and current work when characterizing the fuel injection process. While these techniques have been proven to be effective, they do suffer from limitations described above that leaves room for improvement. The Rainbow Schlieren Deflectometry (RSD) technique has evolved over time to address some of these limitations and provide a solution to the issues that other techniques have faced. While not without its own limitations, applying RSD to fuel spray mixing will provide new insights into the complex fuel injection process and ultimately offer opportunity for increasing energy efficiency while reducing toxic emissions.

The first quantitative use of a schlieren apparatus that produced colored images was employed by Schardin [15], expanding on Toepler's previous findings, in which a lattice filter containing transparent color bands replaced the traditional knife-edge, relating the magnitude of light refraction to corresponding colors. Some 50 years later Howes [16] introduced the "rainbow schlieren" terminology and illustrated the advantage of the continuous spectrum colored filter detecting refractive index nonuniformities in greater detail than the black-and-white knife-edge schlieren approach. Howes applied a concentric, annular, radially symmetric colored filter with a continuous spectrum, as opposed to discrete bands used by Schardin, to achieve better resolution of measured displacements caused by light ray refractions. Rainbow schlieren images of both a stable (Figure 1.11) and unstable acetylene torch, a hot plate, a glycerin-water mixture, and sheet metal revealed that quantification of these refractions, even with turbulent structures, is not only possible but requires relatively simple relations. Greenberg et al. [17] advanced the work of Howes by introducing a filter (Figure 1.12) that provided a color transmission function for any spatial point that would alleviate any discontinuities leading to unwanted diffraction not directly related to inhomogeneities in the test media. Through the hue-saturation-intensity model (HSI), Greenberg et al. eliminated issues due to intensity fluctuations and light absorption or scattering in the test media by transformation of the traditional red-green-blue (RGB) color values that most conventional color video systems capture. This application was instrumental in leading to the digitization of RSD images and the ability to automatically gather quantitative deflection measurements using colorimetry [18].

Agrawal et al. amplified the prevalence of computer-automated quantitative RSD by applying it to a multitude of flow experiments. RSD was purposed to obtain nonintrusive measurements of oxygen concentrations in an isothermal, axisymmetric laminar helium jet

across a full field-of-view which agreed very well with probe measurements taken [19]. Coupled with tomography, RSD was able to quantify the temperature field of a three-dimensional gas flow by measuring beam deflections from multiple viewing angles and applying a tomographic algorithm to reconstruct temperature distributions [20]. Quantification of the transient temperature distributions and flame oscillations of a hydrogen gas-jet diffusion flame flow field at linearly varying operating pressures [21] along with vortex convection velocity profiles at various acquisition rates and high spatial and temporal resolutions [22] was achieved by Agrawal et al. using RSD. Through this, experimental error was seen to decrease at higher image acquisition rates when characterizing the temperature field and oscillations of the flame structure. The scope of quantitative RSD was then broadened via application of miniature RSD when analyzing the scalar flow properties of microjets and flames such as species concentration and temperature data at a remarkable 4  $\mu\text{m}$  spatial resolution [23], as well as full field density measurements and centerline pressure, temperature and Mach number profiles of a supersonic microjet with shock wave interaction [24]. More recently, quantitative RSD was applied to obtain full-field local equivalence ratio measurements [25] and temperatures [26] along with penetration lengths and angles for transient diesel fuel injections at engine-like temperatures and pressures. This work demonstrated the robust capabilities of quantitative RSD to successfully characterize a heterogeneous flow field that hinders many other diagnostic techniques.

The rainbow schlieren apparatus provides solutions to issues other optical diagnostic techniques face when attempting to quantify flow inhomogeneities. The continuous nature of the color filter eliminates concerns of diffraction by the source image. Measurements of refractive-index differences based on color gradations as opposed to irradiance distributions discards the impact of sporadic light absorption and scattering by the test medium. Unlike interferometric

methods in which phase shifts are limited to a relatively narrow range due to their dependence on the illumination wavelength, the Fourier shift theorem implemented for deflection measurements at the filter plane allows for a large dynamic range based on the measurement sensitivity being directly proportional to the focal length of the decollimating lens. For these reasons along with complications listed previously with regards to other optical diagnostic techniques, the ability of RSD to obtain reliable quantitative heterogeneous flow data with relative ease of system implementation proves it to be a viable technique for this application.

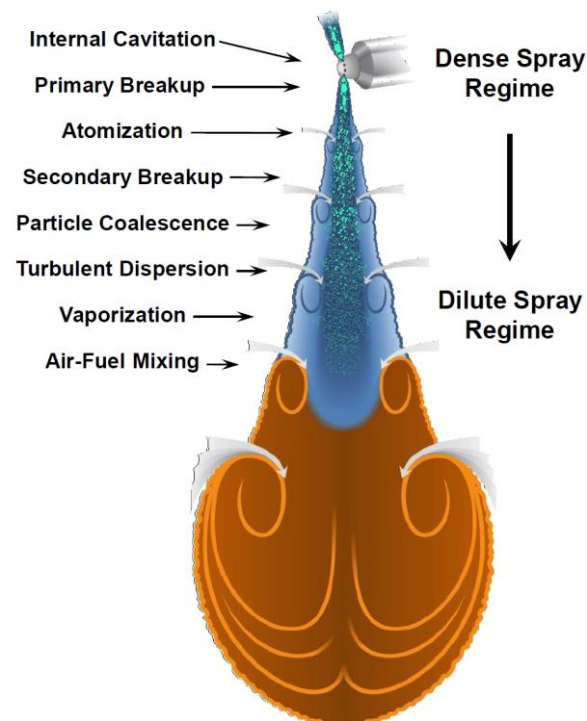


*Figure 1.1.* Illustration of fluid mixing mechanisms during fuel injection process [27].

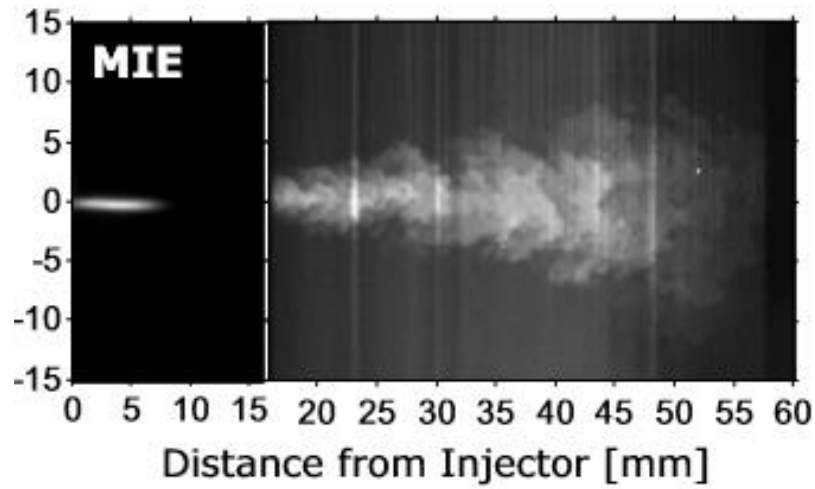


Figure 1.2. Visualization of a diesel injection using Mie-scatter (left) and laser Rayleigh scattering (right) to detect the liquid and vapor portions of the spray, respectively [10].

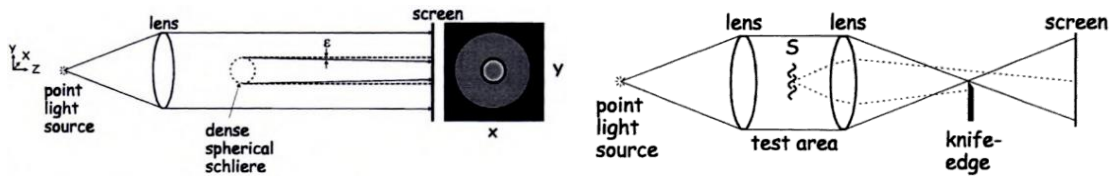


Figure 1.3. Schematics of the optical arrangements for the shadowgraphy (left) and traditional schlieren (right) techniques [5].

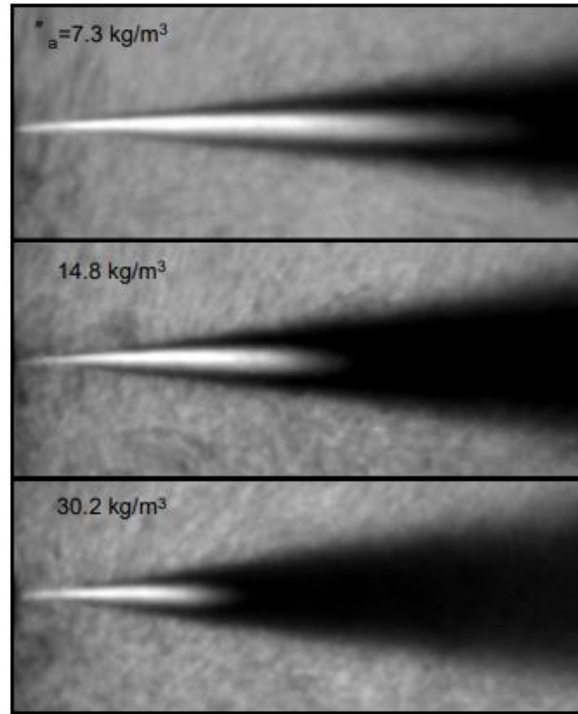


Figure 1.4. Mie-scattered images superimposed on schlieren images for qualitative analysis at various ambient gas densities [6].

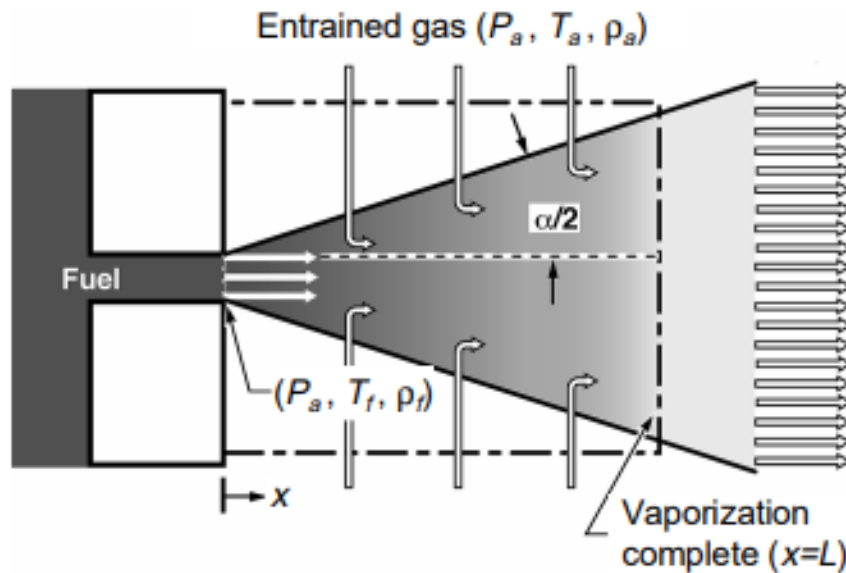


Figure 1.5. Representation of idealized diesel jet model for Siebers's scaling law [7].

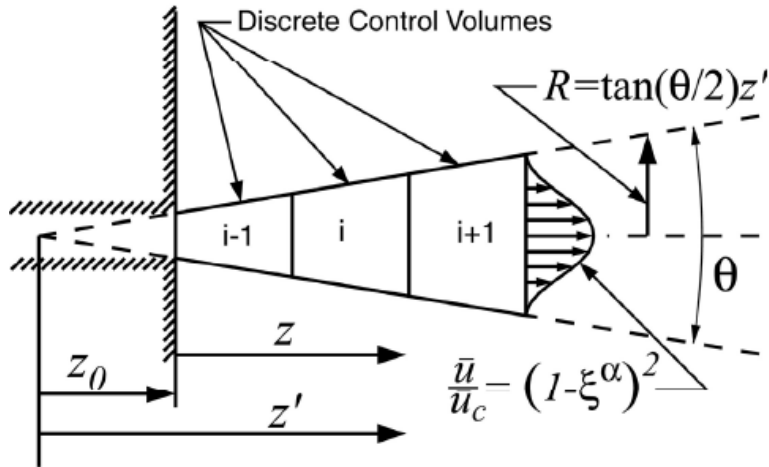


Figure 1.6. Representation of transient idealized diesel jet model developed by Musculus and Kattke [8].

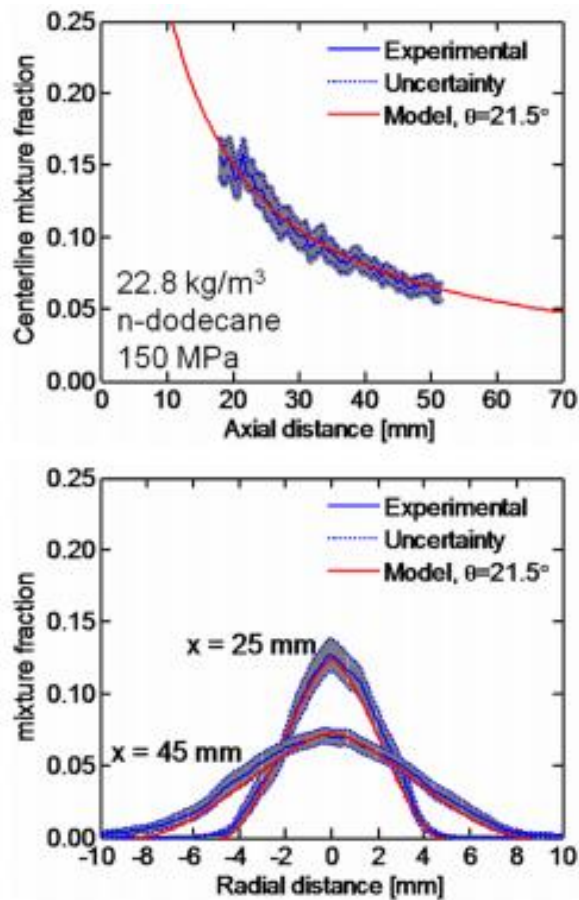


Figure 1.7. Transient jet model predictions compared with experimental results of mixture fractions along the centerline (top) and radial profiles at axial locations of 25 mm and 45 mm (bottom) found by Pickett et al. [9].

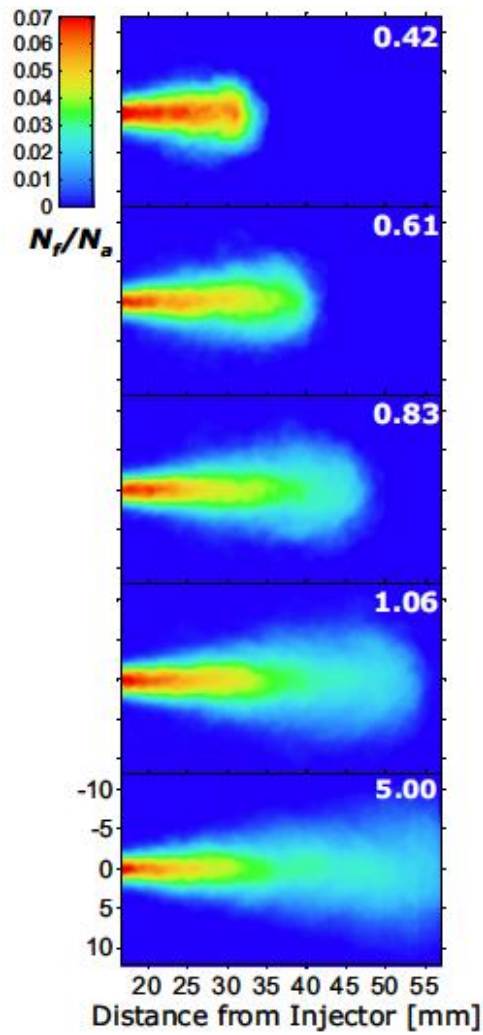
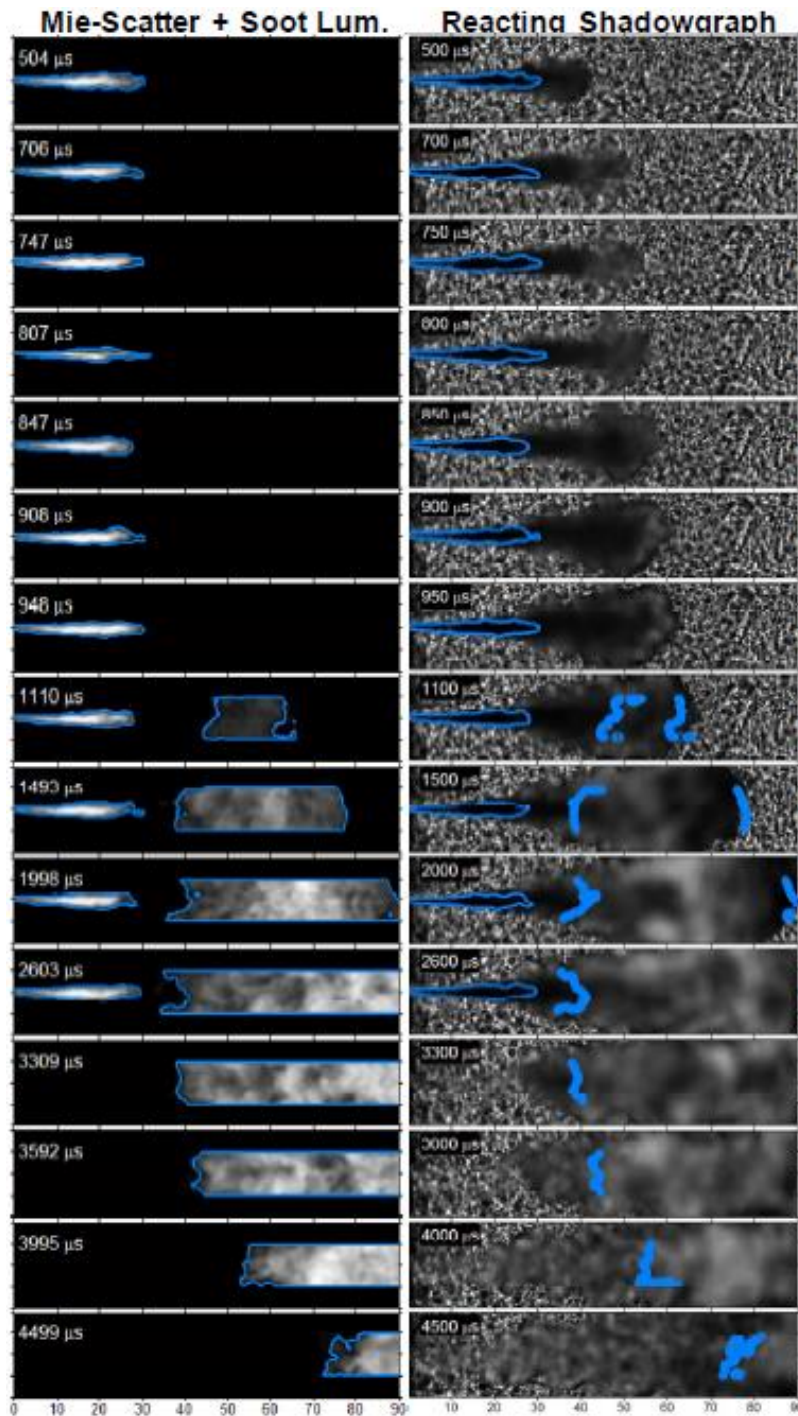


Figure 1.8. Mean fuel-to-ambient number density contours for a transient fuel spray [10]. Quantitative data acquired via Laser Rayleigh Scattering (LRS) technique by Pickett et al.



*Figure 1.9.* Mie-scatter and soot luminosity (left) coupled with shadowgraph technique (right) employed to characterize a reacting transient fuel injection [12]. The “cool-flame” region of the jet is noticeable as the liquid length outlined by mie-scatter recognition recedes in antecedent frames to combustion occurring.

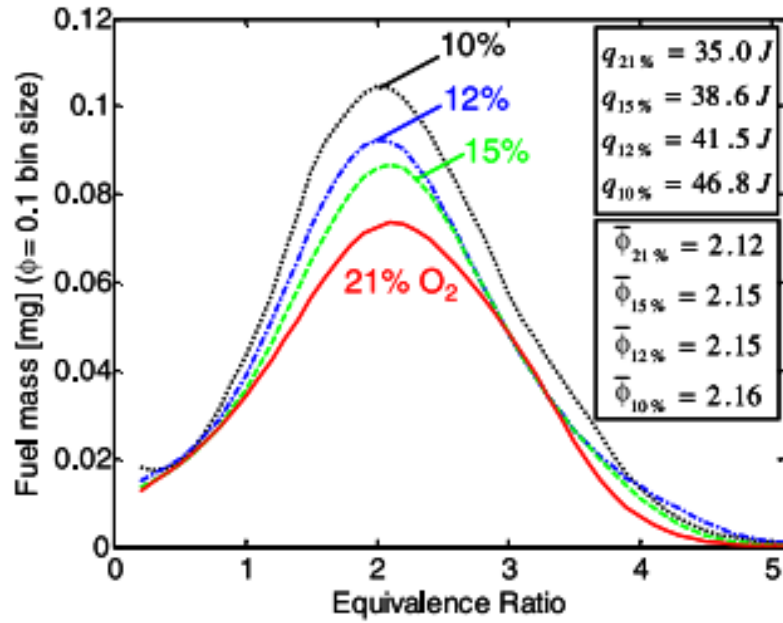


Figure 1.10. Amount of fuel mass present at corresponding equivalence ratios in fuel spray for different levels of oxygen in the ambient air [13].

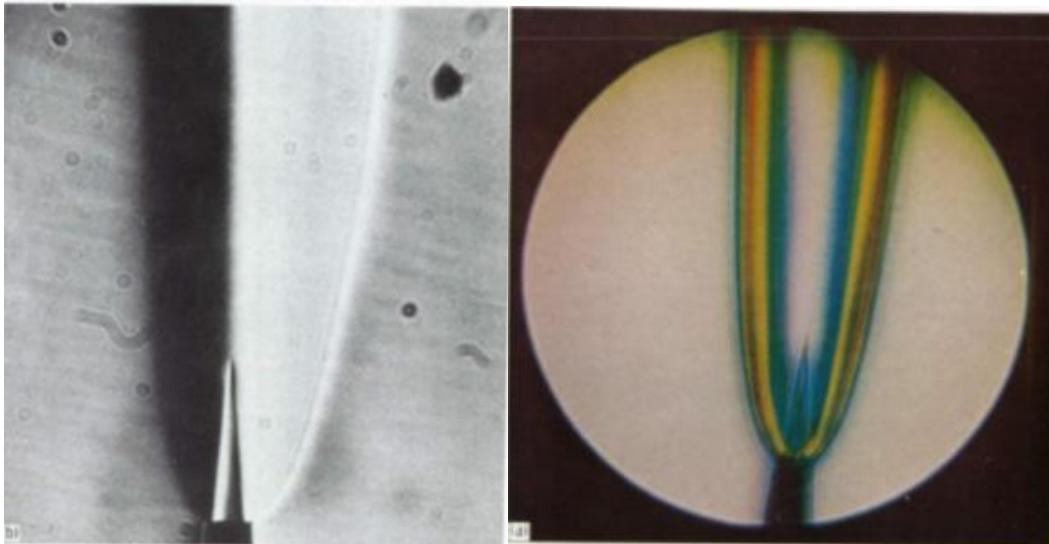
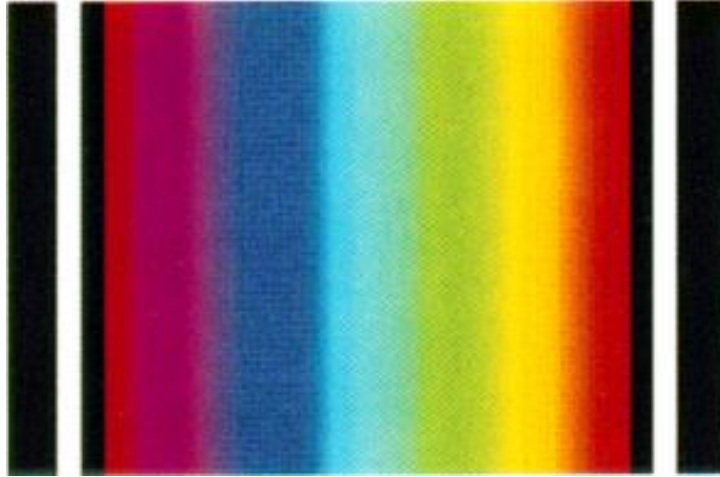


Figure 1.11. Traditional schlieren (left) and rainbow schlieren (right) images of a stable acetylene flame obtained by Howes et al. [16].



*Figure 1.12.* Image of the first rainbow schlieren continuous spectrum color filter for quantitative measurements employed by Greenberg et al. [17].

## CHAPTER 2

### EXPERIMENTAL SETUP

#### 2.1 Constant Pressure Flow Vessel (CPFV)

In order to capture the convoluted mixing processes inherent to diesel injections accurately and efficiently, a spray chamber capable of withstanding elevated pressures and temperatures is necessary to replicate engine-like conditions. The constant pressure flow vessel (CPFV) used in this study is able to endure pressures up to 50 bar and temperatures up to 800°C. A computer model displaying a section view of the CPFV, generated in SolidWorks, is shown in Figure 2.1. The vessel is vertically oriented with a counterflow between compressed air entering upward from the bottom of the vessel and the fuel spray directed downward from the top of the vessel. On the sides of the vessel, there are two parallel quartz windows 100mm in diameter for optical access of the full field spray. One main benefit of the CPFV is the capability to perform multiple injections with minimal time between sequential injections, since the fuel from the previous injection is swept from the test section within a matter of seconds and the ambience returns to the desired state.

#### 2.2 Experimental Procedure

A schematic of the experimental apparatus is presented in Figure 2.2. The desired test conditions are achieved by continuously flowing high-pressure air from a Sauer WP33LB air compressor, which is electrically heated before entering the CPFV. A dome-loaded regulator

located before the heater establishes the air pressure in the CPFV and uses pressurized Nitrogen gas as a pilot to reduce previously encountered pressure fluctuations when using a spring-based regulator. A control valve is also installed downstream of the CPFV to monitor the air flow through the system. The compressed air arrives from the bottom of the vertically oriented CPFV and passes through a “flow straightener” consisting of a 3 cm thick stack of 5-micron metal meshes to create a more uniform ambience void of large vortical structures. The air then exits the chamber through four 3 mm diameter holes at the top of the vessel symmetrically aligned around the injector tip and coolant cup. The air velocity ( $< 0.5$  m/s) being at least two orders of magnitude less than the counterflowing fuel inlet velocity ( $> 100$  m/s) renders the air virtually stagnant and does not impact the penetration of the injected fuel [14]. Thermocouples located near the injector tip and at the boundary of the vessel, along with a pressure transducer, provide instant thermodynamic intensive properties of the system. Insulation jackets are also wrapped around the chamber and injector flange for thermal stability and consistency. The system is considered to be in a steady state when the boundary and near-injector air temperatures are within 20 K of each other - this warm up process takes approximately three hours.

The fuel used in this experiment, *n*-heptane, is supplied from a fuel cart created by Exergy Engineering LLC, and incorporates a pneumatic pressure multiplying pump to deliver high-pressured fuel to the injector. Properties of *n*-heptane are shown in Table 2.1. The fuel pump serves as the primary limit to the dwell between subsequent injections in this experiment. If injections are repeated too quickly it could result in erratic fuel injection pressures. For this reason, the injections are performed every 5 seconds to ensure reliable repeatability throughout the experiment. The fuel is injected through a Bosch CRIN3-18 injector capable of injection pressures up to 1800 bar that is altered to have a single 100  $\mu\text{m}$  hole in the tip to allow for a

single spray down the center of the vessel. The fuel injector specifications are listed in table 2.2. Surrounding the injector body is a “coolant cup” purposed to maintain a desired fuel temperature (90°C in this study) and prevent overheating of the injector. A mixture of coolant and water is pumped from an insulated reservoir containing an immersion heater through insulated tubing to the coolant cup, then from the coolant cup through a heat exchanger and eventually returning to the reservoir. Thermocouples in the reservoir and coolant cup determine whether actuated fans on the heat exchanger along with the immersion heater in the reservoir are activated.

---

**Table 2.1. Fuel Properties of n-heptane.**

---

IUPAC name	heptane
CAS #	142-85-5
Liquid density	684 kg/m <sup>3</sup>
Cetane number	52.5-56
Boiling Point	98.4°C
Enthalpy of Vaporization	316.88 kJ/kg
*Data obtained from NIST [34]	

---



---

**Table 2.2. Fuel injector specifications.**

---

Injector type	Bosch solenoid-driven common-rail
Injector model	CRIN3-18
Nozzle style	Single-orifice
Hole diameter	100 μm

---

Conducting high-speed fuel-spray visualization experiments is reliant upon concurrent regulation of test conditions in the vessel, of the fuel supply and injection triggering, and of the image-capturing system. All thermocouple and pressure transducer analog signals for data post-processing and system monitoring are relayed to a control and data acquisition (CDAQ) system including two National Instruments modules, a CompactDAQ and CompactRIO. A Stanford DG645 digital delay/pulse generator is used in conjunction with the CDAQ, Phantom v611, and

light source to provide precise synchronization between the millisecond injection event and the camera recording. The frequency and number of pulses is set on the pulse generator to determine the image frequency and number of images captured for each injection. A LabVIEW program is installed to remotely control necessary temperature adjustments and injection timings for the system. The number of injections and period between successive injections is specified via LabVIEW. A National Instrument Injector Driver system including the CompactRIO controller, an NI 9751 Direct Injector driver module, and an NI 9411 digital input module is used to send a single command pulse and trigger a fuel injection. For each experiment, the LabVIEW program provides autonomous control over the experiment by simultaneously communicating to the CDAQ system for the DI driver to send a high current electrical signal to drive the injector solenoid and actuate the injector, as well as to the pulse generator. When the pulse generator receives a signal, it sends triggers to pulse the light source and to activate the camera for acquisition of high-speed images and spray data. Phantom software is utilized to record the image/movie files. Electrical signals are also coordinated with the CDAQ system and monitored with LabVIEW to control the electrical air heater, the immersion heater in the coolant reservoir, and the actuated fans on the heat exchanger.

### 2.3 Optical System

The optical configuration of the Rainbow Schlieren Deflectometry apparatus requires attentive consideration for each component in the system. Optics are sensitive to minute alterations and care must be taken throughout each experiment to ensure accurate measurements within the test media is acquired. This section explains the optical system design and hardware involved in this experiment.

Deflection angle measurements in RSD are based on the Fourier shift theorem in relating spatial shifts at the filter plane due to ray deflections from refractive index inhomogeneities to respective wavelengths of the color filter [17]. Therefore, a broadband white light source is required because contains all wavelengths of the spectrum present in the color filter. The light source in this experiment is a white light emitting diode (LED) pulsed at a rate of 40 kHz with 3  $\mu$ s duration (effectively the exposure time) for each fuel injection. Maximizing light input at the source aperture is critical for the spray visualization as it impacts the spatial resolution, framing rate, field of view, and exposure time of the camera. Hence, as much light as possible must be focused on the aperture from the light source. Since LEDs often emit light with large divergence angles, a light collecting system is implemented in this system in which an achromatic collimating lens 50 mm in diameter with a 75 mm focal length is placed in front of the LED to collect the diverging light rays and direct them in a parallel path to a decollimating lens with the same properties. The decollimating lens focuses the light rays onto the rectangular slit aperture to maximize light throughput into the system as seen in Figure 2.3.

The sensitivity and resolution of an RSD configuration are highly dependent on the source aperture size and ray displacement at the color filter plane. A smaller aperture size and larger ray displacements are optimal when obtaining quantitative measurements. The aperture used in this experiment is a 3 mm x 100  $\mu$ m rectangular aperture with the smaller dimension, or width, oriented to be parallel with the transverse (or radial) direction of the test media to obtain transverse deflection angle measurements. Note that the deflection angles in the transverse direction and not in the axial direction is the measurement of interest in this experiment. This is based on the fact that density gradients in the transverse/radial direction are much larger than those in the axial direction.

The light then travels 250 mm (focal length of collimating lens) from the source aperture to a 75 mm diameter collimating lens. The collimated light moves through the test section from left to right in Figure 2.4 and the light rays, undeflected and deflected alike, reach the 75 mm diameter decollimating lens after passing through the test section where they are focused on the filter plane at the focal length of the decollimating lens (250 mm). The decollimating lens is placed directly outside the CPFV window to maximize the capturing of deflected light rays. All lenses in the RSD apparatus are achromatic doublet lenses to avoid light rays being spectrally differentiated before reaching the filter plane. The diameters of the lenses are both greater than the field of view of the test section to acquire full-field data. A schematic of the optical system for the RSD apparatus is displayed in Figure 2.4.

Each ray originating from the source aperture contains the height and width of the aperture and forms an image of the aperture at the filter plane. The size of the image at the filter plane however is dependent on the magnification factor,  $M$ , of the lens setup which is defined in Equation 1. A magnification factor of unity (identical focal lengths) is preferred as an altered ‘ $M$ ’ will impact ray displacement directly and color resolution inversely.

$$M = \frac{f_2}{f_1} \quad 2.1$$

The symmetric rainbow filter at the focal plane of the decollimating lens is 5 mm wide with a continuous color spectrum of hues spanning 20° to 300°. The filter is generated as a digital color image first then is printed on a 35 mm slide film. While the height of the filter is not critical because it plays no role in determining the color scheme, the filter width must be larger than the greatest light ray displacement at the filter plane to encompass all deflected rays passing through the test media. A filter width too large reduces the color range appearing in the schlieren image or sensitivity, while too small a filter width results in a lack of obtaining all relevant data.

The filter then serves as a fine color coder as it rejects all colors except for that which a transversely displaced light ray passes through and corresponds each specific hue to an angular deflection value (discussed in further detail later). Since the LED light source emits broadband light, it contains all wavelengths of visible light and therefore sets no limitations on the hue range. The LED spectral intensity does vary with wavelength, however the RSD technique does not depend on intensity of the signal, only the color as described below. With the rainbow filter containing a continuous color spectrum, the hue at a value of  $0^\circ$  and  $360^\circ$  are equivalent in representing the color red. The hue range is therefore set at  $20^\circ$  to  $300^\circ$  to avoid differentiation inaccuracies of values at the extrema. The printed filter color sensitivity is  $4.2 \mu\text{m}$  per row of color with linearly distributed hue values. A digital version of the color filter is presented in Figure 2.5.

A symmetric filter is advantageous over an asymmetric filter in that it contains twice the amount of colors and therefore twice the color sensitivity, however lacks the ability to decipher whether a light ray is deflected in the positive or negative direction or towards or away from the background filter plane location, respectively. Theoretically, the actual filter used in the RSD experiments would have the same hue distribution as the digitally generated filter, however this is never the case in practice due to the printing and processing of the film and various hardware shortcomings. A prudent filter calibration process is therefore performed prior to the experiments and importance is placed in not altering the system between the calibration and subsequent tests. The calibration process entails adjusting the filter height until the source image is formed directly at the symmetry plane then traversing the filter width in the absence of the test media to obtain a background image for each position of the filter. The filter is traversed in  $25 \mu\text{m}$  intervals via an automated stepper motor synchronized with the image capturing system. A  $100 \times 100$  pixel region

was used in average to assign a hue value to each filter location, accounting for non-uniformities along filter locations due to potential minor optical misalignments, spatial variations in the camera sensor sensitivity, etc. In the analysis procedure, each pixel location in a schlieren image has a measured hue value,  $H$ , that is converted to a transverse position,  $X$ , on the filter plane. These positions are dependent on the filter calibration and the relation is given by Equation 2.2, where  $i$  and  $i+1$  refer to the filter calibration coordinates closest to the measured hue value [24].

$$X(H) = X_i + \frac{X_{i+1} - X_i}{H_{i+1} - H_i} (H_{i+1} - H), \quad 2.2$$

Figure 2.6 displays the filter calibration curve with measured hue values for corresponding transverse displacements. The error bars illustrate the hue variation at each position of the background image. The hue value at the center of the filter is approximately  $25^\circ$  and at the edges of the filter approximately  $300^\circ$ . The mean hue uncertainty in transverse displacement, found from the standard deviation of the measured hue values in the calibration procedure, is  $20 \mu\text{m}$  which is equivalent to less than 1% of the filter width on either side of the symmetry plane. A Phantom v611 digital color camera is used to acquire filtered images throughout the experiment. The size of the images are  $608 \times 200$  pixels containing a  $0.1 \text{ mm}$  per pixel spatial resolution. A  $50 \text{ mm}$  camera lens is used to capture full-field measurements of the spray at a  $3 \mu\text{s}$  exposure time and  $40 \text{ kHz}$  framing rate ( $25 \mu\text{s}$  per frame).

#### 2.4 Hue, Saturation, and Intensity Model

The default imaging method provided by most conventional color video systems involves the red, green, and blue (RGB) representation in which a perceived color consists of some prescribed combination of the tristimulus values [17]. However, the RGB values are all dependent on absolute optical intensities, which allows measurements to be affected by source

intensity fluctuations, scattering and absorption by the test media, etc. In order to rid the color-based filtering process of dependence on optical intensities, Greenberg et al. introduced the hue, saturation, and intensity (HSI) color model that is able to provide a unique color value (hue) at any spatial location on the filter. This differs from the RGB model in which a certain color could be comprised of multiple combinations of the RGB values. The hue refers to the wavelength or frequency of light and is represented on a 0° to 360° scale with both of these extrema referring to the color red, 120° corresponding to green, and 240° representing blue with continuous color gradations between them (see Figure 2.7). Saturation refers to the relative purity of the color or how vivid a color is and is dependent on the intensity value, which represents the brightness or amplitude of the color. Both saturation and intensity are measured on a 0:1 scale where a saturation = 0 would be grayscale and its maximum value is equivalent to the existing intensity value. Equations 2.3-2.5 [17] describe the HSI relations and Figure 2.8 provides a visual representation of how the three values are intertwined. The color values are converted from RGB to HSI through a built-in Matlab function in these experiments.

$$H = \cos^{-1} \left\{ \frac{\%[(R-G)+(R-B)]}{[(R-G)^2+(R-B)(G-B)]^{\left(\frac{1}{2}\right)}} \right\} \quad 2.3$$

$$S = 1 - \frac{\min(R, G, B)}{I} \quad 2.4$$

$$I = \frac{R + G + B}{3} \quad 2.5$$

## 2.5 Rainbow Schlieren Deflectometry Analysis Procedure

Rainbow schlieren images allocate a specific hue value for each location in the image based on the HSI color model. The transverse displacement of a light ray is a function of the hue value measured at a pixel location in the schlieren image and the relation between the two is determined by the filter calibration process. To begin the RSD analytical procedure, reference Figure 2.9 of a deflected light ray passing through the test media and being focused onto the color filter by the decollimating lens.

The rainbow schlieren technique involves obtaining measurements of an integrated quantity, transverse deflection angle of a light ray, along a line-of-sight ( $y$  direction). The transverse deflection angle,  $\varepsilon(x)$ , determines the ray displacement in the transverse or  $x$  direction at the filter plane and is related to the refractive index field in the test media through Equation 2.6. Note that the coordinate system is provided in Figure 2.1, with  $z$  representing the axial direction of the spray,  $y$  representing the direction from the light source to the camera, and  $x$  representing the transverse direction.

$$\varepsilon(x) = \frac{1}{\eta_0} \int_{-\infty}^{\infty} \frac{\partial \eta(x, y)}{\partial x} dy \quad 2.6$$

The normalized refractive index difference is defined as

$$\delta = \frac{(\eta - \eta_0)}{\eta_0} \quad 2.7$$

allowing for Equation 2.6 to be rewritten as

$$\varepsilon(x) = \int_{-\infty}^{\infty} \frac{\partial \delta(x, y)}{\partial x} dy \quad 2.8$$

where  $\eta$  is the refractive index of the test media,  $\eta_0$  is the refractive index of the surrounding gas with no test media present, and  $\delta$  is the normalized refractive index difference. The index of refraction can be related to deflections in the transverse or axial directions, so only one component (transverse in this case) is necessary for acquiring quantitative information. Figure

2.10 reveals the coordinate system of ray trajectories experiencing deflections due to the refractive index field. As discussed in the next section, the refractive index field must be axisymmetric (i.e. only a function of radius). As a result, while the deflection angle is measured in the transverse direction as  $\varepsilon(x)$ , the refractive index difference field shown in Figure 2.9 is  $\delta(r)$  rather than  $\delta(x,y)$ .

An Abel transform can then be used to relate the transverse deflection angles to refractive index gradients at radial locations in the fuel spray. This is done by projecting the field variable, in this case the normalized refractive index difference, from its one-dimensional information [29]. Figure 2.9 illustrates  $\varepsilon$  representing the angle a deflected light ray takes on its path (solid red line) that deviates from the path of an undeflected light ray (dashed red line). A small angle assumption is valid in this setup which allows, for example,  $\tan(\varepsilon) = \frac{\Delta x}{p} = \varepsilon$ . This assumption is applied to all angles in this setup resulting in the following relations.

$$\varepsilon = \frac{\Delta x}{p}, \quad \beta = \frac{\Delta x}{f}, \quad \varepsilon' = \frac{d}{f}, \quad \alpha = \frac{\Delta x}{q} \quad 2.9$$

Then through geometrical relations, it can be seen that

$$\varepsilon' = \beta - \alpha = \Delta x \left( \frac{1}{f} - \frac{1}{q} \right) = \frac{\Delta x}{p} = \varepsilon, \quad 2.10$$

and the deflection angle can then be defined as [29]

$$\varepsilon(x) = \frac{d(x)}{f} = \frac{X(H) - X(H_B)}{f}, \quad 2.11$$

where  $X(H) - X(H_B)$  describes the transverse distance between the measured hue value position on the color filter of a ray passing through the test media and the position of the measured background hue when no test media is present. The derivation of the schlieren optical relations are provided in more detail by Goldstein and Kuehn [30].

After determining the deflection angle of a light ray based on its transverse displacement at the filter plane, the next step is to relate the angular deflection of light to the refractive index field caused by inhomogeneities in the test medium. This relation under an axisymmetric assumption is given as [31]

$$\varepsilon(x) = 2 \int_0^\infty \frac{\partial \delta}{\partial r} \frac{\partial r}{\partial x} dr \frac{\partial y}{\partial r} = 2x \int_x^R \frac{\partial \delta}{\partial r} \frac{dr}{\sqrt{r^2 - x^2}} \quad 2.12$$

since  $\frac{\partial r}{\partial x} = \frac{x}{r}$ ,  $\frac{\partial y}{\partial r} = \frac{r}{y}$ , and  $r^2 = x^2 + y^2$  [28]. Here  $r$  is the radial coordinate,  $y$  is the line of sight direction, and  $x$  is the offset distance from the jet axis. Applying the Abel inverse integral transform then allows for the refractive index field,  $\frac{d\delta}{dr}$ , to be solved for as follows [29]:

$$\delta(r) = \frac{-1}{\pi} \int_r^R \varepsilon(x) \frac{dx}{\sqrt{x^2 - r^2}}, \quad 2.13$$

which, to avoid measurement uncertainties due to divergence at the lower integration limit, can be expressed in dot product summation since the measured deflection angles are point values [32].

$$\delta(r_i) = \sum_{j=i}^{N+1} D_{ij} \varepsilon_j \quad 2.14$$

Here  $\varepsilon(r_j)$  is the deflection angle information at an incremental pixel spacing  $\Delta r$ ,  $\delta(r_i)$  represents the discrete refractive index difference, and  $r_j = (j - 1)\Delta r$  is the radial distance from the axisymmetric centerline to the pixel location. In this case  $\Delta r$  is 0.1 mm per pixel based on the spatial resolution provided by the camera.  $N$  describes the number of steps from the axis of symmetry, or centerline of the spray, to the radial edge of the spray which varies with axial position, and  $i$  and  $j$  refer to data points from 1 to  $N+1$ . The linear operator coefficients  $D_{ij}$  are determined independently of  $\Delta r$  and are found using the highly accurate two-point integration

algorithm [29] in which a linear profile is approximated in each segment between deflection angle points, avoiding singularity at  $y=r$ . These coefficients are found as follows:

$$\begin{aligned}
D_{ij} &= \frac{1}{\pi} (A_{ij} - A_{i,(j-1)} - jB_{ij} + (j-2)B_{i,(j-1)}) \quad \text{if } j > i \text{ and } j \neq 2, \\
&= \frac{1}{\pi} (A_{ij} - jB_{ij} - 1) \quad \text{if } j > i \text{ and } j = 2, \\
&= \frac{1}{\pi} (A_{ij} - jB_{ij}) \quad \text{if } j = i \text{ and } i \neq 1, \\
&= 0 \text{ if } j = i = 1 \text{ or } j < i \\
A_{ij} &= \sqrt{j^2 - (i-1)^2} - \sqrt{(j-1)^2 - (i-1)^2}, \\
B_{ij} &= \ln \left( \frac{j + \sqrt{j^2 - (i-1)^2}}{(j-1) + \sqrt{(j-1)^2 - (i-1)^2}} \right)
\end{aligned} \tag{2.15}$$

The results of this process [29] produce the normalized index of refraction difference,  $\delta$ , along radial planes of the spray. This Abel inversion method is applied independently to both halves of the axisymmetric spray then the information is combined to represent the entire spray.

The Abel inverted results of center plane refractive index difference, based on measured deflection angles, can then be used to determine the amount of fuel present in terms of equivalence ratio at each location in the spray. For areas of the spray treated as an ideal gas mixture of fuel vapor and air, the refractive index is defined as shown in Equation 2.16 and described in [25].

$$\eta = \eta_0(\delta + 1) = 1 + \sum_i \kappa_i \rho_i \tag{2.16}$$

Here,  $\kappa_i$  is the Dale-Gladstone constant and  $\rho_i$  is the partial density of the  $i$ th species. Dale-Gladstone constant values for heptane and air are  $\kappa_f = 0.000518 \text{ m}^3/\text{kg}$  and  $\kappa_a = 0.000226 \text{ m}^3/\text{kg}$  respectively [33]. While not strictly appropriate in all cases/regions, using an

ideal gas assumption, density can be related to thermodynamic properties like temperature, pressure, and mole fraction yielding a refractive index of

$$\eta = 1 + \frac{P}{\bar{R}_u T} \sum_i \kappa_i X_i MW_i, \quad 2.17$$

where  $P$  is the mixture pressure,  $T$  is the mixture temperature,  $\bar{R}_u$  is the universal gas constant,  $MW_i$  is the molecular weight, and  $X_i$  is the species mole fraction. In rearranging Equation 2.17 and assuming air to be a single species, the fuel volume fraction can then be expressed as [25]:

$$X_f = \frac{\frac{\bar{R}_u T}{P} (\eta_0 (\delta + 1) - 1) - \kappa_a MW_a}{\kappa_f MW_f - \kappa_a MW_a} \quad 2.18$$

This displays the ability to solve for the fuel volume fraction assuming an ideal gas mixture of both air and fuel vapor and a known mixture temperature. For isothermal mixing this is a fairly straight forward calculation, however an evaporating fuel spray is clearly not isothermal. In this study, the quantification of the fuel-air mixing process in terms of local equivalence ratio and mixture temperature values is achieved through a unique relation between these local scalar properties based on an assumed thermodynamic equilibrium between fuel and air at a given mixture concentration. As cold fuel mixes with hot air, the relative concentration will determine the equilibrium mixture temperature and thus equivalence ratio and mixture temperature are not independent variables. Equations 2.16 and 2.17 provide this relation for an ideal gas mixture in which the normalized refractive index difference, measured by the RSD technique, can be linked to these local scalar properties. However, it is more appropriate to use real gas relations for the fuel vapor, especially at the high pressure involved in this experiment. Equation 2.19 offers the specific relationship employed in this study that describes the normalized refractive index difference of the fuel and air mixture in the vapor portion jet [26].

$$\eta_0(\delta + 1) = 1 + \kappa_a \frac{P_a X_a}{R_a T_{mix}} + \kappa_f \rho_f \quad 2.19$$

Here,  $P_a$ ,  $X_a$ , and  $R_a$  refer to the pressure, mole fraction, and specific gas constant for air and  $\rho_f$  signifies the density of fuel in the mixture based on the mixture temperature and pressure. This method assumes that the fuel and air still behave as a perfect mixture (i.e. volume mixing is appropriate). Finally, the equivalence ratio can be expressed in terms of the fuel volume fraction, molecular weights of the fuel and air, and the stoichiometric air to fuel ratio on a molar basis  $\overline{AF}_s$ .

$$\Phi = \frac{\overline{AF}_s MW_f}{\left(\frac{1}{X_f} - 1\right) MW_a} \quad 2.20$$

Figure 2.11 graphically represents the particular relationship between the equivalence ratio or mixture temperature versus the normalized refractive index for the test conditions in this study under the assumption that the gases experience adiabatic mixing until reaching thermodynamic equilibrium. The far left points in Figure 2.11 refers to the normalized refractive index of the ambient air which is equal to zero, and correspondingly an equivalence ratio of zero and a ambient air temperature of 825 K. The data points furthest to the right represent a normalized refractive index difference of 0.01 which correlates to an equivalence ratio and mixture temperature around 40 and 460 K, respectively. The relationship illustrated here implies that equivalence ratio and mixture temperature values can be determined once refractive index difference values are attained via Equations 2.13-2.15. The error bars shown in Figure 2.11 are a result of the propagation of uncertainty in hue and are seen to be minimal for equivalence ratios greater than 1.0. Other measurement uncertainties in this experiment include the previously mentioned mean hue uncertainty from the filter calibration curve in Figure 2.6, along with uncertainty due to mathematical singularities and numerical integration errors. However, a robust

inversion algorithm and the high quantity of injections measured to achieve the necessary axisymmetric assumption helps curtail the mathematical and numerical integration methods.

## 2.6 Projected Three-Dimensional Fuel Mass Calculations

As stated in previous sections, the benefit of utilizing a nonintrusive, accurate optical diagnostic technique such as the rainbow schlieren deflectometry apparatus is the capability to characterize the complicated fuel injection process quantitatively and qualitatively for ultimate improvement in fuel efficiency and limiting toxic emissions. Therefore, a more realistic representation of what is occurring during the fuel breakup and eventual combustion mechanism is sought after to relate the results of the diesel engine processes to the aforementioned concerns. Knowledge of the local amount of fuel on a mass basis gives insight not only to the fuel-air mixing process but also to how the mixture will eventually react. To do this, the two-dimensional fuel spray data acquired at each pixel location is “weighted” based on the radial distance from the spray centerline, similar to the method Picket et al. employed [13]. Both halves of the axisymmetric spray are swept 180° by multiplying each pixel in the schlieren image by “ $\pi r$ ” to project the two-dimensional data as a more practical three-dimensional data set. The swept pixel volumes are achieved by Equation 2.20.

$$v_i = \frac{(\pi(r_i + px_{res}))^2 - \pi r_i^2}{2} px_{res} \quad 2.20$$

Here  $v_i$  and  $r_i$  represent the swept pixel volume ( $m^3$ ) and the pixel radial distance (m) from the spray centerline respectively, and  $px_{res}$  is the pixel resolution (m/pixel). Equation 2.20 exhibits how each pixel is converted into a pixel volume for each half of the spray. The pixel volume can

also be defined as a summation of the amount of fuel and air present since those are the only two fluids involved in the system.

$$v_i = v_{f,i} + v_{a,i} \quad 2.21$$

$v_{f,i}$  and  $v_{a,i}$  are the the partial volumes that the fuel and air occupy for each given swept pixel volume. Knowledge of the fuel-air mixture temperature and pressure,  $\{T, P\}_{mix}$  at each pixel location allows for representation of the fuel and air volumes to be

$$v_{f,i} = \frac{m_{f,i}}{\rho_{f,i}\{T, P\}_{mix}}, \quad 2.22$$

$$v_{a,i} = \frac{m_{a,i}}{\rho_{a,i}\{T, P\}_{mix}} \quad 2.23$$

where  $m_{f,i}$  and  $m_{a,i}$  are the masses (kg) of fuel and air present in each pixel volume, respectively. The fuel density,  $\rho_{f,i}$ , is provided by the NIST [34] database and called via a Matlab function at the reference temperature and pressure, and the air density,  $\rho_{a,i}$ , is calculated based on the ideal gas law given the mixture pressure and temperature. The masses of fuel and air in each pixel volume are related by the air-to-fuel ratio,  $AF_i$ , shown in Equation 2.24.

$$AF_i = \frac{m_{a,i}}{m_{f,i}} \quad 2.24$$

The equivalence ratio is also defined as

$$\Phi_i = \frac{AF_s}{AF_i} \quad 2.25$$

where  $AF_s$  is the stoichiometric air to fuel ratio and is a known constant for a heptane-air mixture. Lastly, through substitution and rearrangement of Equations 2.19-2.25, the fuel mass can now be directly solved for using Equation 2.26. The swept pixel volume, densities of air and fuel at a given pressure and temperature, and stoichiometric air to fuel ratio are all known variables.

$$m_{f,i} = \frac{v_i}{\frac{1}{\rho_{f,i}\{T,P\}_{mix}} + \frac{AF_s}{\Phi_i \rho_{a,i}\{T,P\}_{mix}}} \quad 2.26$$

The fuel mass can now be calculated at any given radial position of the projected three-dimensional fuel spray, allowing for further analysis regarding the fuel-air mixing behavior and ultimate combustion.

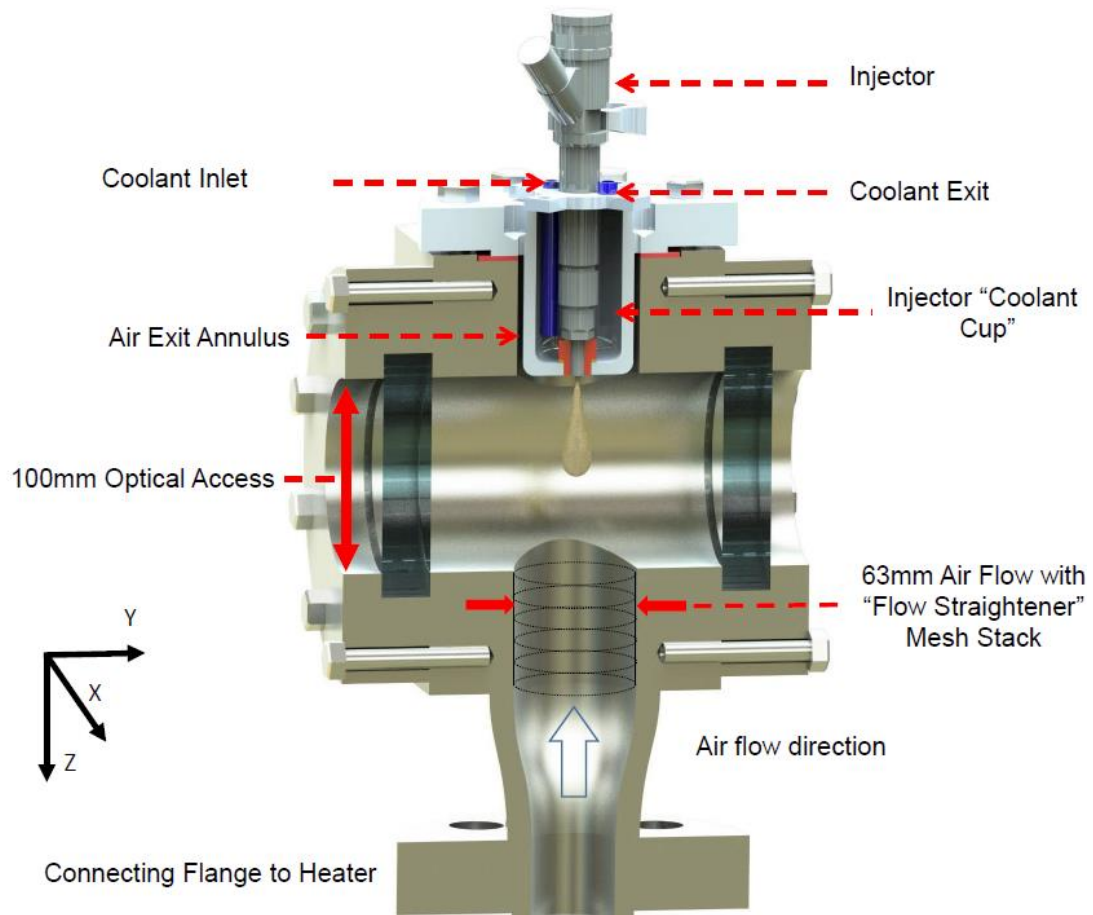


Figure 2.1. Constant pressure flow vessel (CPFV) illustration.

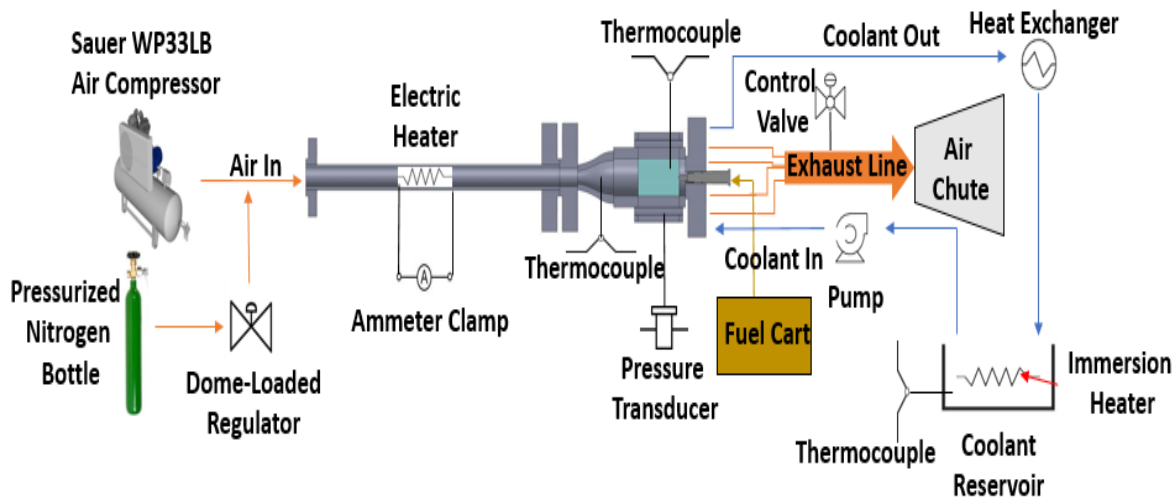


Figure 2.2. Schematic of experimental apparatus (not to scale).

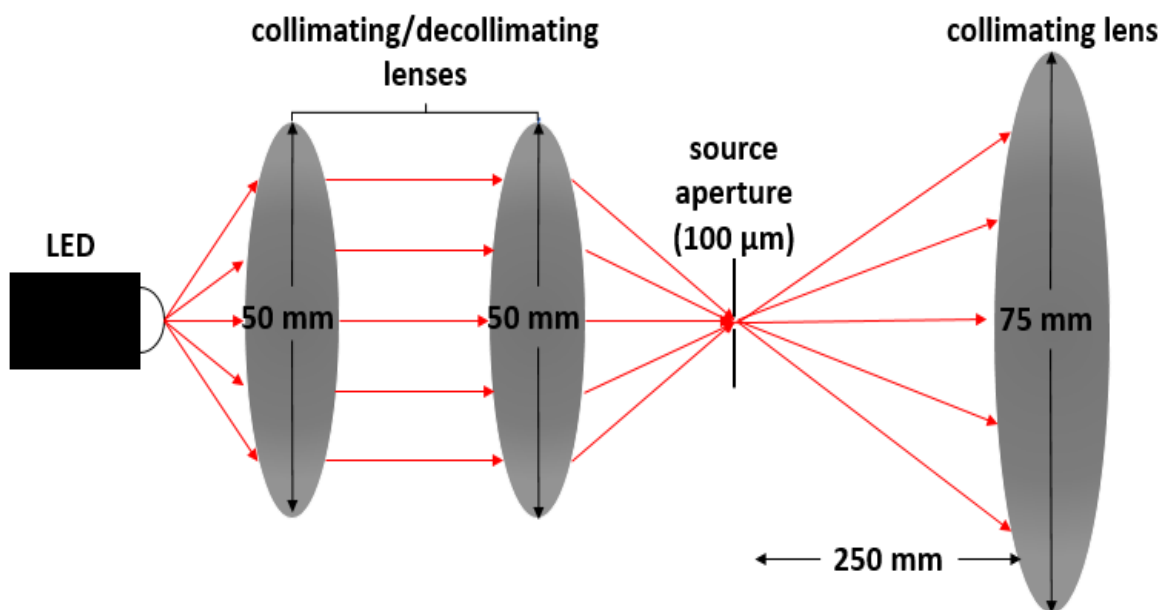


Figure 2.3. Schematic of light collection system on the collimating side of the RSD apparatus (not to scale).

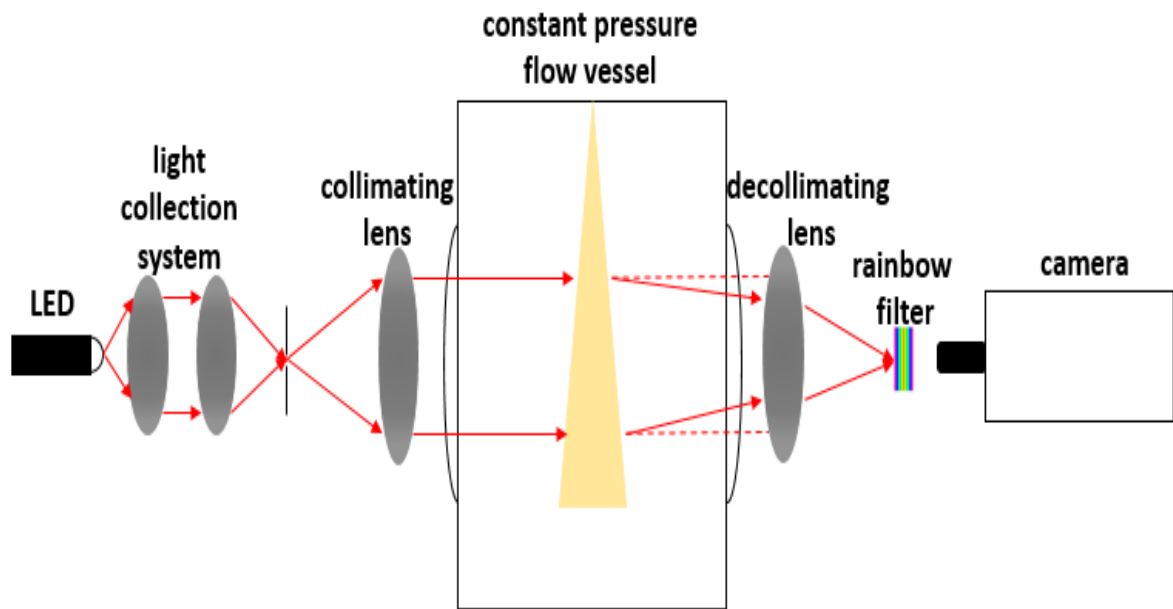


Figure 2.4. Schematic of RSD optical configuration (not to scale).

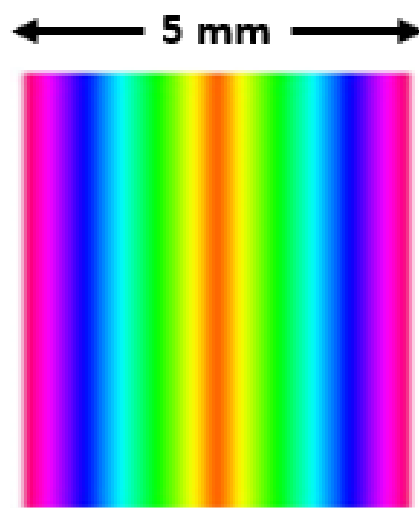


Figure 2.5. Digital symmetric rainbow filter.

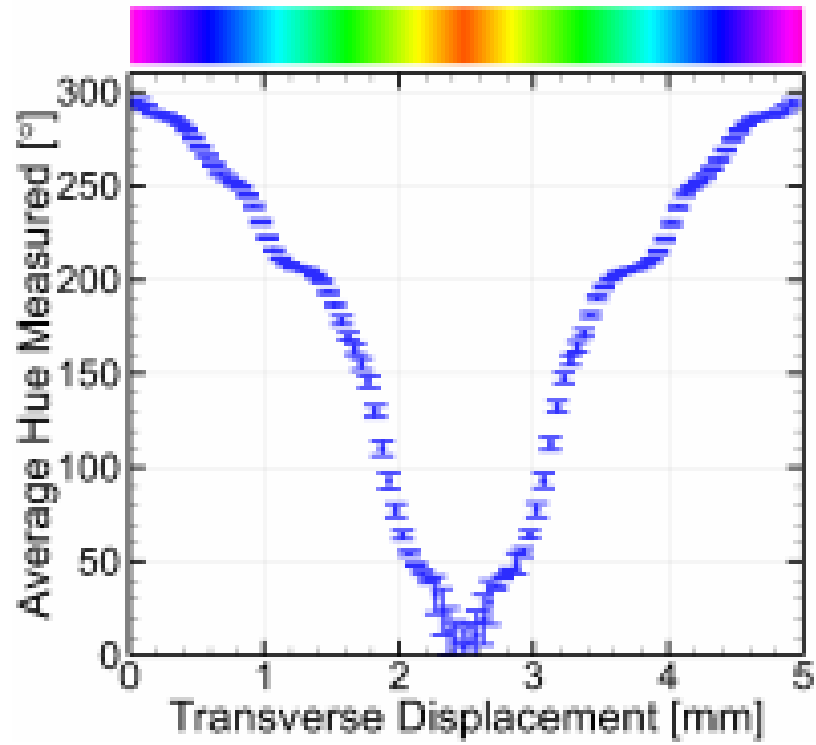


Figure 2.6. Rainbow filter calibration curve with hue range from 20° to 300°. Error bars represent a  $\pm 2\sigma$  deviation in the 100x100 pixel imaging region.

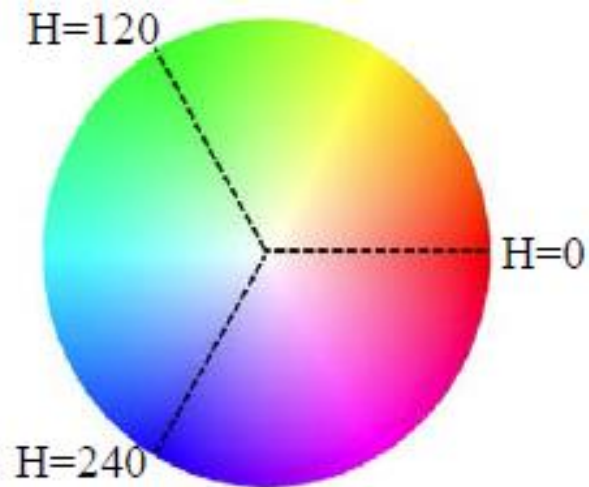


Figure 2.7. Hue color wheel with corresponding values [28].

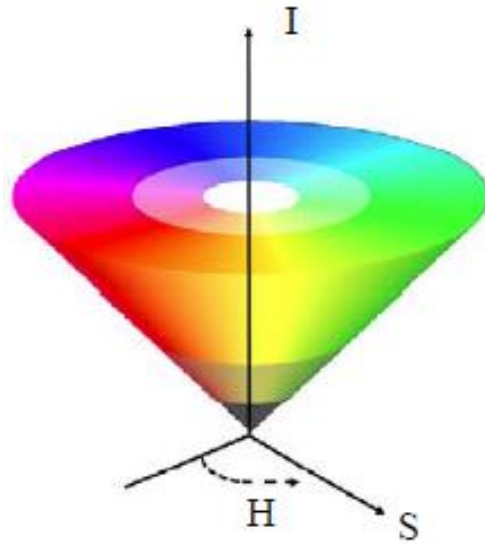


Figure 2.8. Visual representation of Hue, Saturation, and Intensity color model [28].

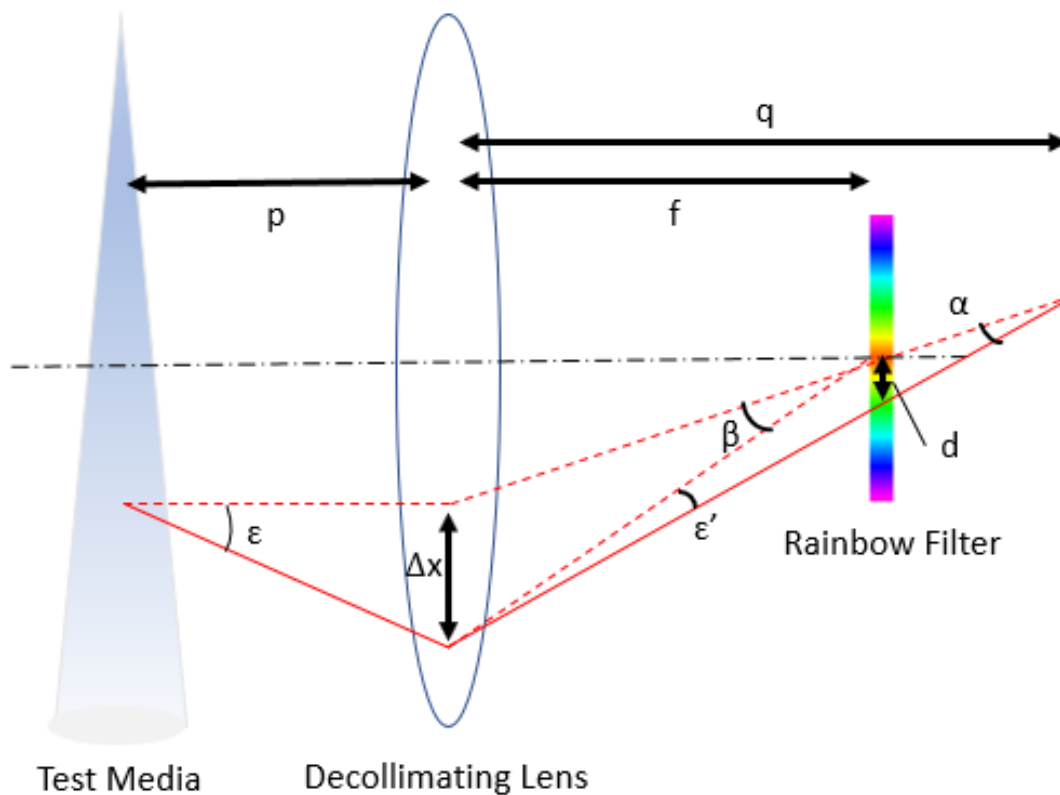


Figure 2.9. Illustration (not to scale) of a deflected light ray transversely displaced on color filter. Solid red line represents a light ray deflected by the test media whereas the dashed red line represents the path of an undeflected light ray crossing the center of the color filter.

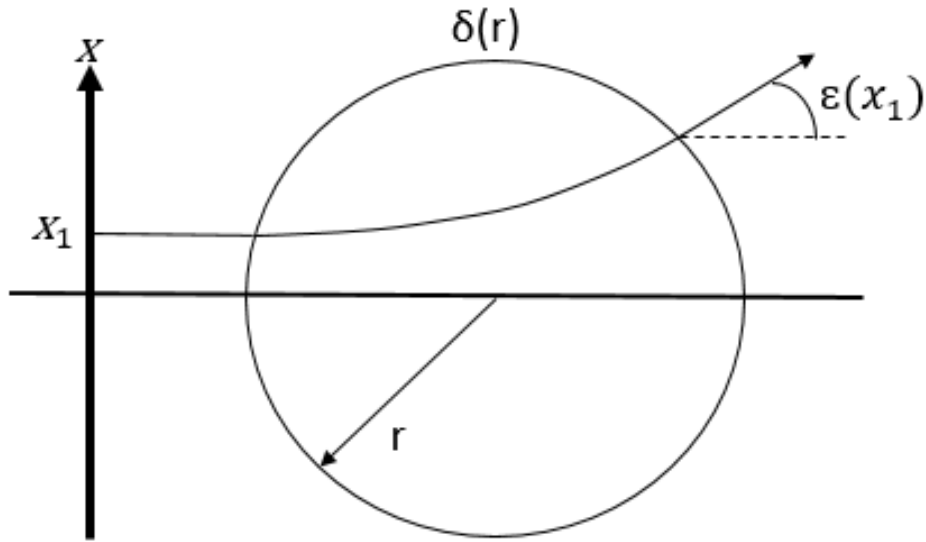


Figure 2.10. Geometrical representation of a deflected light ray passing through an axisymmetric inhomogeneous refractive index field of radius  $r$ . Light rays are deflected in the transverse or  $x$  direction at an angle  $\epsilon(x_i)$  based on the refractive index difference  $\delta(r_i)$  of the path the rays pass through.

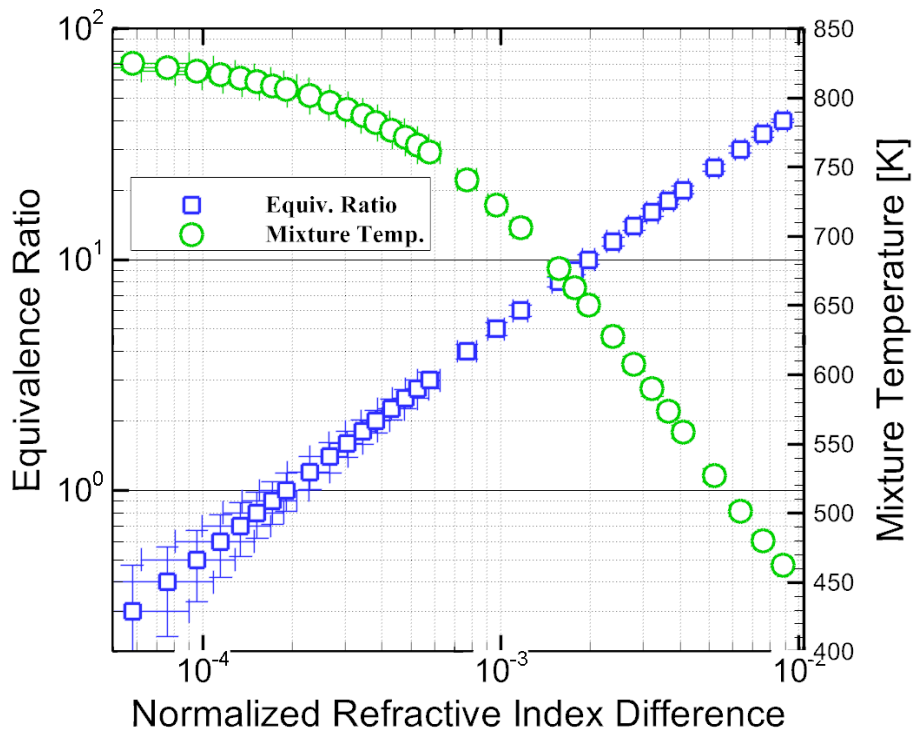


Figure 2.11. Equilibrium thermodynamic mixing relating the normalized refractive index difference to equivalence ratio and mixture temperature.

## CHAPTER 3

### RESULTS AND DISCUSSION

#### 3.1 Overview

Experiments were performed with ambient air conditions in the CPFV at a pressure of 28 bar and a temperature of 825 K to emulate practical diesel engine conditions. Injections of *n*-heptane were conducted at a supply pressure of 1000 bar every five seconds to let the fluid from the previous experiment to be swept from the test section. The ability to conduct successive experiments in a quick fashion with the CPFV allows for 50 injections to be recorded in a matter of minutes. The test conditions are described in Table 3.1. This is critical as the Abel inversion technique requires an axisymmetric test media, and thus the measured deflection angle data must be ensemble averaged to account for the asymmetry inherent in instantaneous images of turbulent flows. The measured data for an individual image at its respective time step is averaged on a pixel by pixel basis for each of the 50 injections. Every experiment involves 60 frames captured per injection in 25  $\mu$ s increments for a total of about 1.5 ms per injection. In regards to the spray coordinate system,  $\pm x$  and  $z > 0$  represent the transverse (radial) and axial location, respectively. Figure 3.1 illustrates how the ensemble average value at a few example pixels stabilizes as the number of injections averaged approaches the 50 captured in this work. The deflection angle data is averaged at a steady axial location  $z = 26.7$  mm and three different radial locations ( $x = 1.5, 2,$  and  $2.5$  mm) to illustrate the convergence at locations with various mixture compositions and properties in the spray. As you can see from the instantaneous sprays in Figure

3.2, the spray development and mixture formation may be similar and relatively steady at each time step, but still vary from spray to spray, especially with the turbulent mixing occurring at the radial boundary. This is why it is necessary to ensemble average the deflection angle data in order to validate an axisymmetric assumption.

**Table 3.1. Test Conditions.**

Ambient Pressure	28 bar
Ambient Temperature	825 K
Fuel Temperature	363 K
Injection Pressure	1000 bar
Injection Duration	1.5 ms
Number of Injections	50

### 3.2 Spray Evolution

A sample of the RSD images captured during a single injection is shown in Figure 3.3. The same data is shown in two formats. The left column of images shows the raw RSD images as captured directly on the camera sensor (no processing at all). In the right column the pixel intensity and saturation values have been increased to a maximum to make the hue variations more visually distinct to human eyes. As the RGB values are converted to HSI the hue signal is retained in this process, therefore not affecting the processed results. In addition, a lower limit intensity threshold is utilized to blackout the injector and thermocouple in the images.

The instantaneous images in Figure 3.3 illustrate the hue variations that the RSD signal measures during the fuel injection process. The orange/red background in each of the images represents the undeflected light rays passing through the ambient air in the test section that are focused at the center of the color filter with a measured hue of about  $25^\circ$ . Also, notice the relatively large-scale motionless structures of the air in the background, indicative of a quiescent ambience. The density gradients of the fuel, relative to the ambient air, injected into the test section cause deflections of the collimated light rays represented by color gradations at the filter

plane. The initial jet at  $t = 0.075$  ms aSOI portrays mainly blue and purple colors symbolizing relatively significant deflections due to the dense fuel present at this time. As the jet evolves, the fuel entrains and mixes with the ambient air causing smaller density gradients at the radial boundary and axially downstream of the dense liquid core. These smaller gradients are represented by a variety of colors such as light blue, yellow, and green while the near injector region maintains its darker blue/purple color throughout the injection duration. The jet tip extends to an axial distance of  $z = 42$  mm by  $t = 0.75$  ms aSOI which equates to an average jet velocity of 56 m/s, again proving a quiescent ambience with an air flow two orders of magnitude less than the jet velocity.

From  $t = 0.325$  ms aSOI to  $t = 0.75$  ms aSOI, the jet continues to penetrate downstream in the axial direction and spread in the radial direction as entrained ambient air continues to mix with the vapor jet. As the jet evolves to  $t = 1.175$  ms aSOI, it is evident that chemical kinetics are operating in conjunction with early stage fuel breakdown, releasing heat and raising local mixture temperatures to the extent that the refractive index is indifferentiable from that of the ambient air. Low temperature heat release (LTHR) is well underway as the RSD signal of the jet has noticeably retracted in the radial direction at  $z > 30$  mm and  $x > 3$  mm. Physically, it would be expected that the jet continues to penetrate downstream in the axial direction from  $t = 0.75$  ms aSOI to  $t = 1.175$  ms aSOI. However, the tip of the jet actually appears to recede at  $z > 40$  mm as RSD detection has been eliminated and the previously described LTHR zone forms. Although the fuel-air mixture has achieved a refractive index similar to that of the ambience and cannot be visibly differentiated, the fine scale turbulent structures inherent to the jet flow are still apparent between  $30 \text{ mm} < z < 50 \text{ mm}$  at  $t = 1.175$  ms aSOI, signifying the presence of the vapor jet mixture. The area involving the presence of the fuel-air mixture recognized by the fine scale

turbulent structures at  $t = 1.175$  ms aSOI has been outlined in the right column of Figure 3.3 to show that the jet is still continuing to develop downstream even though the RSD signal has diminished in this region. This interpretation is justified by the reintroduction of the RSD signal in the downstream combustion region at  $t = 1.475$  ms aSOI, where large density gradients are evident just past  $z = 50$  mm.

### 3.3 Transient Fuel-Air Mixing

The evolution of the jet is displayed in Figure 3.4 by means of equivalence ratio and mixture temperature contours to describe the transient fuel-air mixing process. These measurements are shown downstream of the liquid length region ( $z \approx 10$  mm) and only include RSD data from pixels in the vapor region of the jet. Characterization of the fuel-air mixing process is crucial because it determines the fuel and air distribution at each point in the jet. This information coupled with the temperature distribution will ultimately determine how the mixture will react.

At  $t = 0.15$  ms aSOI, there is a fuel-rich core along the centerline of the jet containing high equivalence ratio ( $\phi$ ) values along with low temperatures, and vice versa along the boundary of the jet. There is enough entrainment of the hot ambient air by this point to vaporize the spray, however not a sufficient amount of time for the fuel-air mixing to infiltrate the fuel-rich jet core. By  $t = 0.45$  ms aSOI, the equivalence ratio in the fuel-rich core of the jet is seen to decrease with increasing axial position due to air entrainment and subsequent exchange of transport properties in the shear layer. This introduction of air into the jet then causes radial expansion with increasing axial distance. At  $t = 0.75$  ms aSOI, the turbulent mixing of the air into the jet causing flow inhomogeneities gives rise to the local transport of mass, momentum,

and heat driven by gradients in concentration, velocity, and temperature between the two fluids. This behavior has induced more fuel-air mixing as the once fuel-rich core becomes hotter and leaner, represented by the radial shrinking of the red and orange region. Here the jet is at the maximum axial penetration length recognized by the RSD signal, and LTHR is assumed to begin as fuel breakdown at the radial edge of the jet has caused mixture temperatures and chemical kinetics to commence. As seen at  $t = 1.175$  ms aSOI, the fuel vapor in the LTHR zone between a radial location of about  $2 \text{ mm} < x < 3 \text{ mm}$  contains mixtures with  $\phi < 4$  and a temperature of about 750 K. At around  $z = 3 \text{ mm}$ , the mixture temperature is around 800 K with  $1 < \phi < 2$ . Both of these radial locations possess equivalence ratio and temperature combinations prone to ignition, which is validated by this region losing the RSD signal and eventually reacting. Although the center of the jet upstream of the tip is still relatively fuel rich and cool in the LTHR zone shown, one can infer that mixing will continue between  $t = 0.75$  ms aSOI and  $t = 1.175$  ms aSOI to make the fuel-air mixture in this area ignitable since the RSD signal retracts along the axial centerline as well (see Figure 3.3).

### 3.4 Fuel Mass Analysis Procedure

The fuel mass calculations are focused on the portion of the spray downstream of the liquid length ( $\approx 10 \text{ mm}$ ) as quantitative RSD measurements are valid only in the vapor region of the jet. While the vapor region offers transparency allowing the light rays to pass through and the deflections to be measured by the hue value they illuminate on the color filter, the liquid portion of the spray (near injector) absorbs more light than the vapor phase making it difficult to quantify deflections. The light absorption and scattering by the dense liquid core are evident in the measured intensity values from the HSI model. The implementation of a white LED light source

containing a uniform color spectrum avoids issues with spectral distribution intensity deficiencies at the color filter. For liquid phase recognition a procedure developed in [35] is applied with the following providing a brief overview. The background intensity distribution is obtained by averaging the intensity values of the first frame, before the fuel is injected into the test section, of each injection at every pixel location. The background intensity values at each pixel are subtracted from the measured intensity values of the subsequent images with the test media present to account for any inhomogeneities causing unwanted light absorption or scattering from optical components or the test media, and to acquire a relative intensity at each location of the spray. This relative intensity is then used to set a threshold in which any pixel containing a value lower than the threshold value is determined to be in the liquid phase, and vice versa for the vapor phase. Once all the pixels are identified as either above or below the set threshold, a search algorithm is employed at each axial location which starts at the center of the spray and marches radially until the first relative intensity value above the threshold (indicating vapor phase) is detected. The radial locations at which this occurs for each axial location are then marked to define a liquid boundary as indicated by the black solid and dashed lines in the near-field (~10mm) of Figure 3.5. The solid inner line represents the average boundary while the dashed outer line represents the average boundary location plus the one standard deviation outward from the average based on the 50 injections captured. This procedure maintains a very similar resolution in liquid boundary detection as the Mie-scatter technique as demonstrated in [35].

The equivalence ratio and mixture temperature values are found at each pixel location of the vapor region in the schlieren image via the adiabatic mixing relation shown in Figure 2.11 based on the measured normalized refraction index difference values. These local quantities

provide information of the fuel and air distribution along with the thermodynamic conditions of the fuel-air mixture throughout the spray. Once the mixture properties are known throughout the spray, the fuel mass calculation process defined in Equations 2.20-2.26 is applied. The pixel locations that are considered to be a part of the jet are determined by a similar marching method to identify the liquid region based on relative intensity values. In the case of vapor phase recognition, an algorithm is applied at each axial location to start at the center of the spray and search outward radially until reaching a pixel containing an equivalence ratio value that is less than a set threshold recognized as ambient air. This practice is done on both halves of the spray for each frame to provide a jet boundary throughout the evolution of the jet. Next, each pixel contained within the spray boundary is weighted based on its radial distance from the centerline as described in Equation 2.20 to obtain a three-dimensional pixel volume. The fuel mass for each pixel volume is then calculated via Equation 2.26, providing an amount of fuel present for corresponding equivalence ratio and mixture temperature values.

### 3.5 Low Temperature Heat Release Zone Analysis Procedure

The low temperature heat release (LTHR) zone in this study refers to the region of the spray development in which the jet visually disappears along with the RSD signal. This is due to the heat release during initial fuel breakdown causing the density gradients from thermal variations and concentration variations to oppose each other to the point that the refractive index of the fuel-air mixture becomes indifferentiable with the refractive index of the ambient gas. The procedure in identifying the LTHR zone involves: 1) determining the last frame before LTHR begins in which the RSD recognized jet retracts, and establishing the vapor jet boundary at this moment. This is done by visually analyzing the spray images and digitally finding the frame at

which the RSD signal detects the maximum vapor jet penetration length; 2) locating the frame at which the main ignition has begun but the non-reacting near-injector RSD based boundary is stable, and then digitally identifying the vapor jet boundary that the RSD signal recognizes; 3) subtracting the vapor jet boundary location of the frame during this steady combustion period from the vapor jet boundary of the frame just before LTHR begins. This procedure provides an isolated region of the pixels for which the RSD signal is lost and where the ignition process is observed to begin.

As broadly described in the Section 3.1 above, a visualization of this phenomenon is displayed in the instantaneous rainbow schlieren images of the spray evolution displayed in Figure 3.3. It can be seen here that the vapor jet appears to recede both radially and axially from  $t = 0.75$  ms after start of injection (aSOI) to  $t = 1.175$  ms aSOI, corresponding to the last frame before LTHR occurs and the last frame before combustion begins in the transient injection process, respectively. The LTHR zone is further identified in the equivalence ratio and mixture temperature contours for the jet evolution in Figure 3.4, where the vapor jet boundary retraction is evident between  $t = 0.75$  ms aSOI and  $t = 1.175$  ms aSOI. The isolated LTHR zone is then shown at the bottom of Figure 3.4, representing the difference between the previously discussed vapor jet boundaries.

This is a region of interest as it symbolizes the fuel-air mixture formation that will eventually combust, as seen at  $t = 1.475$  ms aSOI in Figure 3.3. Therefore, this pre-ignition zone is isolated to analyze the amount of fuel present at corresponding mixture temperatures and equivalence ratios to give an indication of how these mixtures will react. In calculating the fuel mass distribution in the LTHR zone, it is assumed that the amount of fuel present here at the frame just before LTHR commences ( $t = 0.75$  ms aSOI) is relatively constant until injection ends

(previous work demonstrates the rapidity in which the spray stabilizes [26]). This implies that the mixture state in this LTHR region is quasi-steady and thus it is appropriate to consider the data in this region from the measured RSD data at  $t = 0.75$  ms aSOI. Since the RSD signal starts to vanish once LTHR begins, it is not possible to quantify local scalar properties in the LTHR zone nor determine how the mixing continues after the jet penetrates past  $t = 0.75$  ms aSOI.

The reduced vapor jet boundary at  $t = 1.175$  ms aSOI is found using the same algorithmic procedure as previously described, and its pixel locations are superimposed on the vapor jet at  $t = 0.75$  ms aSOI. To aid in the portrayal of this process, imagine overlaying the jet at  $t = 1.175$  ms aSOI on top of the jet at  $t = 0.75$  ms aSOI, then subtracting the area occupied by the superimposition. The portion of the jet still remaining is considered the LTHR zone. An algorithm is then employed to march on a pixel by pixel basis, at each axial location downstream of the liquid length, radially outward from the boundary (as opposed to the center of the jet previously) of the jet at  $t = 1.175$  ms aSOI to the maximum penetration jet boundary at  $t = 0.75$  ms aSOI. All the pixels falling in between the two vapor jet boundaries are considered to be part of the LTHR zone. The deflection information and thermodynamic properties at each pixel in the LTHR region are then exported to ANSYS Chemkin. An equilibrium calculation of the vapor-phase mixtures is then used to solve for the adiabatic flame temperatures, providing the maximum temperature combustion could attain given the initial conditions at each pixel location [36].

### 3.6 Fuel Mass Measurements

Determining the amount of fuel mass present in the vapor portion of the jet is beneficial in gaining a better understanding of fuel-air distributions and of how the eventual combustion

process may occur. Since the amount of fuel mass in a combustible mixture determines the energy and potential heat released during the reaction process, it is valuable to know the fuel mass present at corresponding mixture temperatures and equivalence ratios susceptible to ignition. The characterization and manipulation of the vapor jet in this manner will then allow for optimization in ultimately increasing fuel efficiency and limiting toxic emissions in the combustion process.

Figure 3.6 represents the amount of fuel present at corresponding equivalence ratios for different time steps throughout the spray as well as the low temperature heat release (LTHR) zone. This data set is obtained by first incrementally locating pixels from the RSD averaged images based on the equivalence ratio values in steps of  $\Delta\phi = 0.1$  from  $\phi = 0.5$  to  $\phi = 10$ . The fuel mass values at each pixel location are then found using the aforementioned analysis procedure and are summed together to attain a total fuel mass for each respective equivalence ratio. The data shown in Figure 3.6 has been slightly post processed through a zero-phase filter to suppress oscillation amplitudes. As expected, the total amount of fuel increases with each progressing time step because there is more fuel being injected into the system. The general trend for all three time steps includes a majority of the fuel mass being located at  $0.8 < \phi < 1.1$ , alluding to the entrained air mixing well with the vapor jet. Also, notice that only the  $\phi < 5$  fuel mass allocation increases as more fuel is injected into the system from  $t = 0.45$  ms aSOI to  $t = 0.75$  ms aSOI. This is indicative of the fuel-rich upstream portion of the jet reaching steady-state quickly so that the additional injected fuel only contributes to the  $\phi < 5$  portion as the jet penetrates downstream. This explanation is supported by the equivalence ratio contours in Figure 3.4 in which the leaner green and blue portions grow, while the richer red and orange core remains stable in the near-field. More of the fuel mass containing leaner equivalence ratios also

makes sense physically in that the lean mixtures further away from the center of the spray occupy a greater jet volume than the rich mixtures located near the spray center.

In reference to the contours of Figure 3.4, the fuel mass distribution for the LTHR zone in Figure 3.6 is composed of equivalence ratios that are likely to react given adequate mixture temperatures, displaying almost all the fuel mass with  $\phi < 4$  and again a majority of the fuel around  $\phi = 1.0$ . Recall that the data from the LTHR zone is merely a subset of the data from the jet at  $t = 0.75$  ms aSOI, representing the area between the jet boundary at this time and at  $t = 1.175$  ms aSOI at which the RSD signal is lost. These values are leaner because, as shown in Figure 3.4, the ignition begins at the tip of the jet consisting of mainly green and blue corresponding to  $\phi < 4$ . Again, the blue values at the boundary of the LTHR zone representing  $\phi = 1.0$  have more fuel mass present due to being the furthest distance from the center of the jet and thus corresponding to a large volume fraction of the overall LTHR region, corroborating the peak location in Figure 3.6.

The energy released during the combustion process is reliant upon the amount of fuel available to burn. However, too much fuel present relative to available oxygen during the reaction process will lead to incomplete combustion, leaving unused potential for energy production. A stoichiometric equivalence ratio indicates that there is enough oxidizer, in this case air, available for the present fuel mass to react. Therefore, the more fuel mass present at stoichiometric equivalence ratios entails that proportionally more air will accompany the fuel, leading to optimal potential for heat release and energy production from a given mass of fuel. A majority of the fuel mass in the LTHR zone containing equivalence ratios around 1.0, as depicted in Figure 3.6, is accordingly most advantageous from a fuel efficiency and toxic emissions standpoint.

Figures 3.7 and 3.8 illustrate contour maps to show the relative concentration of fuel mass at respective equivalence ratio and mixture temperature values. In order to produce these figures, the pixels containing equivalence ratio values between  $0.5 < \phi < 20$  are first identified. Then, much like the procedure employed to generate Figure 3.6, except now with the added dimension of mixture temperature, the ranges of equivalence ratio and mixture temperature are spanned in incremental segments such that  $\Delta \phi = 0.1$  and  $\Delta T_{\text{mix}} = 10 \text{ K}$ . Each combination of these incremental segments creates what is considered a “bin”. The pixels are then distributed to respective bins based on the equivalence ratio and mixture temperature information accordingly. For example, a pixel measured to have an equivalence ratio and mixture temperature of 1.24 and 781 K respectively would be assigned to the bin covering  $1.2 < \phi < 1.3$  and  $780 < T_{\text{mix}} < 790 \text{ K}$ . The calculated fuel mass from each pixel in every respective bin is then summed, creating a total fuel mass for each incremental equivalence ratio and temperature combination. The summed fuel mass values allocated to each bin are then slightly smoothed through a Gaussian filter to generate the contour maps – this filtering minimally affects the trends and primarily serves to make the contours more visible to the reader’s eye.

The relative fuel mass concentration for the vapor jet with respect to equivalence ratio and mixture temperature for the jet evolution is shown in Figure 3.7. A greater amount of fuel is seen to contain leaner equivalence ratios and hotter mixture temperatures as the jet develops and more fuel-air mixing occurs. This mixing process occurs along the adiabatic mixing line described in Figure 2.11, but the slight Gaussian filter shows a wider distribution again for the purpose of making the figure more easily interpreted by the reader. At  $t = 0.15 \text{ ms aSOI}$ , the thinner nature of the contour plot in Figure 3.7 is due to less fuel being present in the system – as the peaks get higher the Gaussian filter will spread the contour out slightly more. This is

supported by the noticeably small amount of fuel mass across  $0.5 < \phi < 10$  for  $t = 0.15$  ms aSOI in Figure 3.6. At this early stage the initial high-velocity turbulent fuel injection is able to entrain enough air to vaporize the fuel downstream of  $z = 10$  mm but lacks the time for the ambient air to significantly influence the mixture composition in the jet core region. This is illustrated by the thick pink rich region in the equivalence ratio contour in Figure 3.4 and by a large amount of the fuel mass being widely distributed above  $\phi > 5$  and below  $T_{\text{mix}} < 700$  K in Figure 3.7. Still, due to the larger weighting of pixels towards the edge of the jet there is still a localized concentration of fuel near  $\phi=1$  and  $T_{\text{mix}} = 800$  K. This highlights the importance of not only analyzing the contours in Figure 3.4 as one may think more of the fuel is rich and cold due to the large rich core.

As more fuel enters the system by  $t = 0.45$  ms aSOI, the red and orange regions begin to appear in Figure 3.7 down and to the right, indicating more fuel mass containing hotter mixture temperatures and leaner equivalence ratios. By this time, it is evident that the vapor jet has entrained enough air in the shear layer to cause radial expansion and expedite the fuel-air mixing process, resulting in more fuel mass at hotter and leaner conditions. This mechanism is reinforced by the observed radial expansion and increasing of the lean green and blue portions of equivalence ratio contour in Figure 3.4, and likewise the growing of the hot red, orange and yellow portions of the temperature contour. Figure 3.6 also explains this trend as the fuel mass values increase with decreasing equivalence ratios to up to  $\phi = 1.0$ . At this point, the mixing in the vapor jet is working towards creating ignitable mixtures based on the local scalar properties measured. All three figures are demonstrating an increase in fuel mass at mixture compositions and temperatures prone to ignition. The mixing process will continue until the proper balance is

found between the fluid mechanics and chemical behavior that will ultimately lead to combustion.

At  $t = 0.75$  ms aSOI, Figure 3.7 reveals again that as additional fuel mass is injected into the system, more fuel mass moves down and to the right along the contour line, becoming relatively leaner and hotter. This is portrayed by the pink region emerging and the red region thickening at  $\phi < 5$  and  $T_{\text{mix}} > 750$  K. This trend occurs because the fuel-rich core of the vapor jet reaches a seemingly steady-state, exhibited in the Figure 3.4 contours, and the supplementary injected fuel continues to penetrate and mix downstream of  $z = 35$  mm. Here the green and red regions become more prominent for the equivalence ratio and mixture temperature contours respectively, representing increased zones of mixtures with properties susceptible to ignition. Figure 3.6 further depicts the mixture composition of the fuel mass added as the only equivalence ratio values where the fuel mass is measured to increase is at  $\phi < 5$  from  $t = 0.45$  ms aSOI to  $t = 0.75$  ms aSOI. Figures 3.4, 3.6, and 3.7 illustrate common trends in the fuel-air mixing behavior that produces leaner and hotter mixtures and characterize the majority of the fuel mass concentration to have mixture properties likely to react at  $t = 0.75$  ms aSOI.

In the fuel injection process, the fluid behavior determines the equivalence ratio at each point in the mixture, which coupled with the mixture temperature governs the combustion process. Once the energy of a mixture composition is raised to a sufficiently excitable state on a molecular level, radicals form and chemical kinetics coupled with fluid mechanics determine how the mixture will burn. After a flame is formed it will propagate and consume surrounding fuel-air mixtures, potentially at faster reaction rates than mixing rates. The mixture properties and amount of fuel mass in regions prone to ignition are therefore of great importance in influencing the potential heat release and products of the combustion process. As can be seen at  $t$

= 1.475 ms aSOI in Figure 3.3, combustion first occurs near the radial center and axial tip of the jet. The maximum penetration length of the jet detected by the RSD signal (frame before the tip begins to visually recede) is at  $t = 0.75$  ms aSOI. Therefore, the local mixture properties and amount of fuel mass in the far-field at this time step are very impactful in determining the subsequent combustion behavior. Most of the fuel mass being at equivalence ratios around 1.0 in the LTHR zone, as shown in this study, is beneficial for reasons detailed in the next section.

Figure 3.8 displays a contour plot of the fuel mass concentration in the LTHR zone at measured mixture temperature and equivalence ratio values (labeled “pre-ignition”). This plot is generated using the same procedure employed for Figure 3.7. The data from each pixel in this region is passed through a chemical equilibrium solver via ANSYS Chemkin in which the adiabatic flame temperature is computed from the given mixture properties. The results from this process are shown (labeled “post-ignition”) to describe the initial combustion behavior and are overlaid on a heat map containing regions in which diesel fuel reacting in a 21% ambient oxygen environment has been measured to emit soot and  $\text{NO}_x$ . Note the equivalence ratio range being cut off at  $\phi = 5.0$  and the temperature scale covering a much larger range than that of Figure 3.7, making the pre-ignition contour appear visually thinner. Again, a Gaussian filter is the cause of the post-ignition contour appearing more spread out, not the measured data.

The pre-ignition data describes most of the fuel mass at  $\phi < 1.5$  and at mixture temperatures between 750-800 K, which is expected for this well mixed region downstream of the liquid length and agrees with the results from Figures 3.6-3.7. The adiabatic flame temperature calculations provide some interesting insight to how these mixtures initially react. The hottest flame temperatures correspond to initial conditions with near stoichiometric equivalence ratios, invading the  $\text{NO}_x$  region as high combustion temperatures are known to do.

This area illustrated by red color shows that most of the fuel mass at  $1.0 < \phi < 1.2$  will reach flame temperatures around 2500 K, which is where the most heat release potential exists with sufficient oxygen to react with the fuel present. Realistically, the flame temperature is not likely to reach those high of magnitudes as the adiabatic flame temperature calculations do not take into account heat losses nor potential chemical kinetic and transport property limitations present in actual practice [36]. As equivalence ratio values move away from this region, the flame temperatures decrease in either direction due to rich mixtures not having enough oxygen present for complete combustion, or lean mixtures lacking the amount of fuel to reach higher temperatures. This effect is evident in the fuel mass concentration moving to green and blue colors, indicating that each incremental change in equivalence ratio causes a relatively a significant drop in flame temperature.

Qualitatively it can be seen that these initial combustion events will avoid significant soot production while approaching flame temperatures subject to high  $\text{NO}_x$  emissions. While the equilibrium solver employed in this process explains how these mixtures will initially react, it does not characterize the entire combustion event. Ignition begins at near-stoichiometric equivalence ratios but no further detail is provided regarding the reaction behavior. It is possible that the carbon particles from the incomplete combustion in the richer core of the jet are consumed as they pass through the hotter stoichiometric part of the flame. It is also conceivable that the combustion becomes rich by nature after combustion first occurs at near-stoichiometric conditions as the flame may propagate to richer mixtures and react at a faster rate than mixing occurs.

These theories are substantiated by the optical image sequence displayed in Figure 3.9, where a combustion process at slightly different test conditions (ambient temperature and

pressure are 785 K and 33 bar, respectively) is captured at a 20 kHz framing rate. It is clear in this sequence that ignition initially occurs at near-stoichiometric conditions resulting in complete combustion symbolized by the high-temperature, blue colored flame at  $t = 2.15$  ms aSOI. As the frames progress the chemical kinetics propagate the flame front to nearby mixtures containing a richer fuel composition indicated by the blue color slowly dissipating, signifying reactions becoming cooler. At  $t = 2.65$  ms aSOI the first sign of an orange/yellow flame appears, conveying incomplete combustion of fuel rich mixtures. By  $t = 3.25$  ms aSOI, the bright orange/yellow color of the flame appears to form at the radial center of the jet, hinting that the soot as a product from nearby incomplete combustion in the fuel-rich jet core is being consumed by the propagating flame front. Although the equilibrium solver provides insight to the initial reaction behavior of the measured mixture properties, it does not assess the behavior of the entire combustion event.

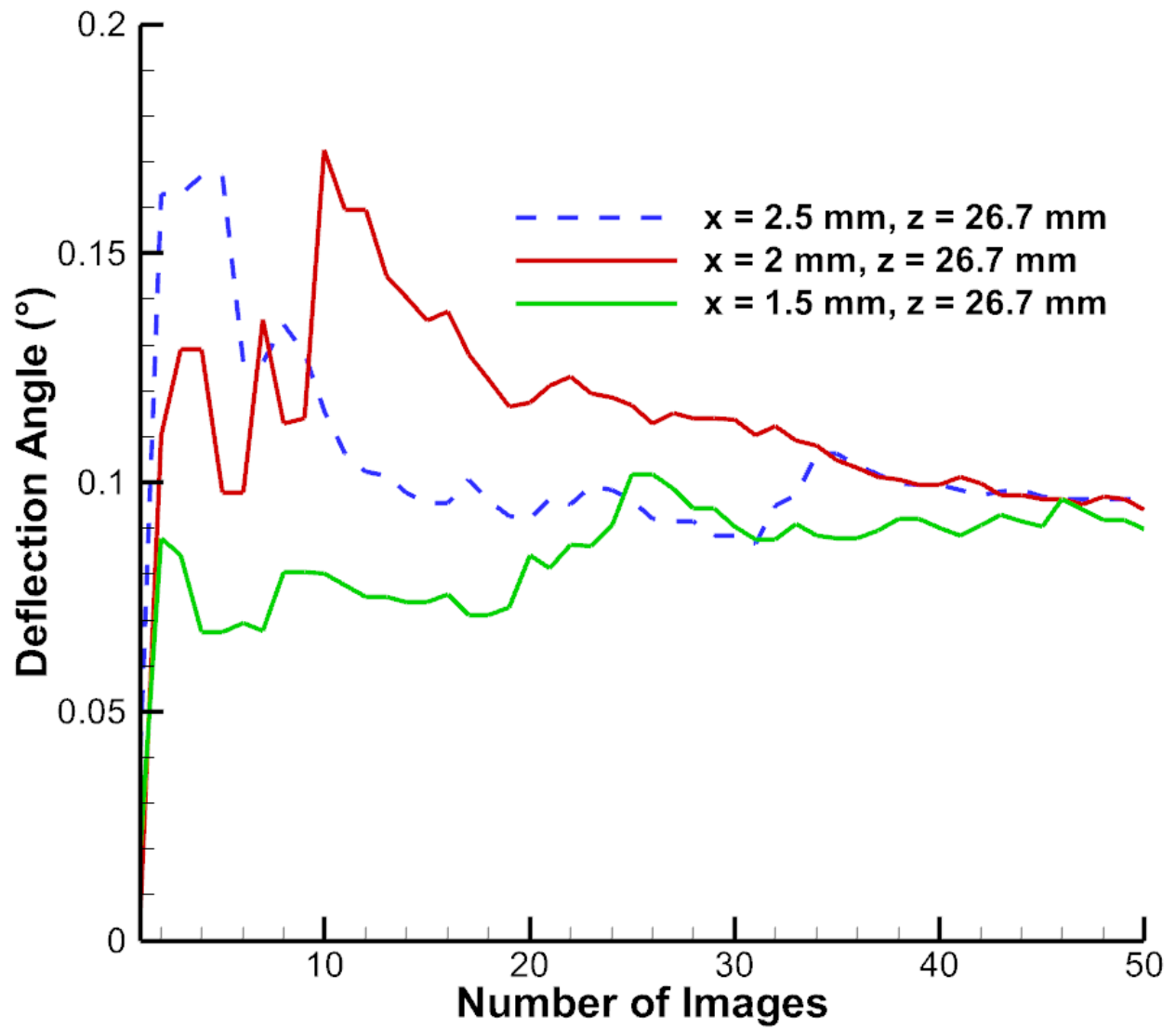


Figure 3.1. Effect of amount of image samples on average deflection angle at specific locations.

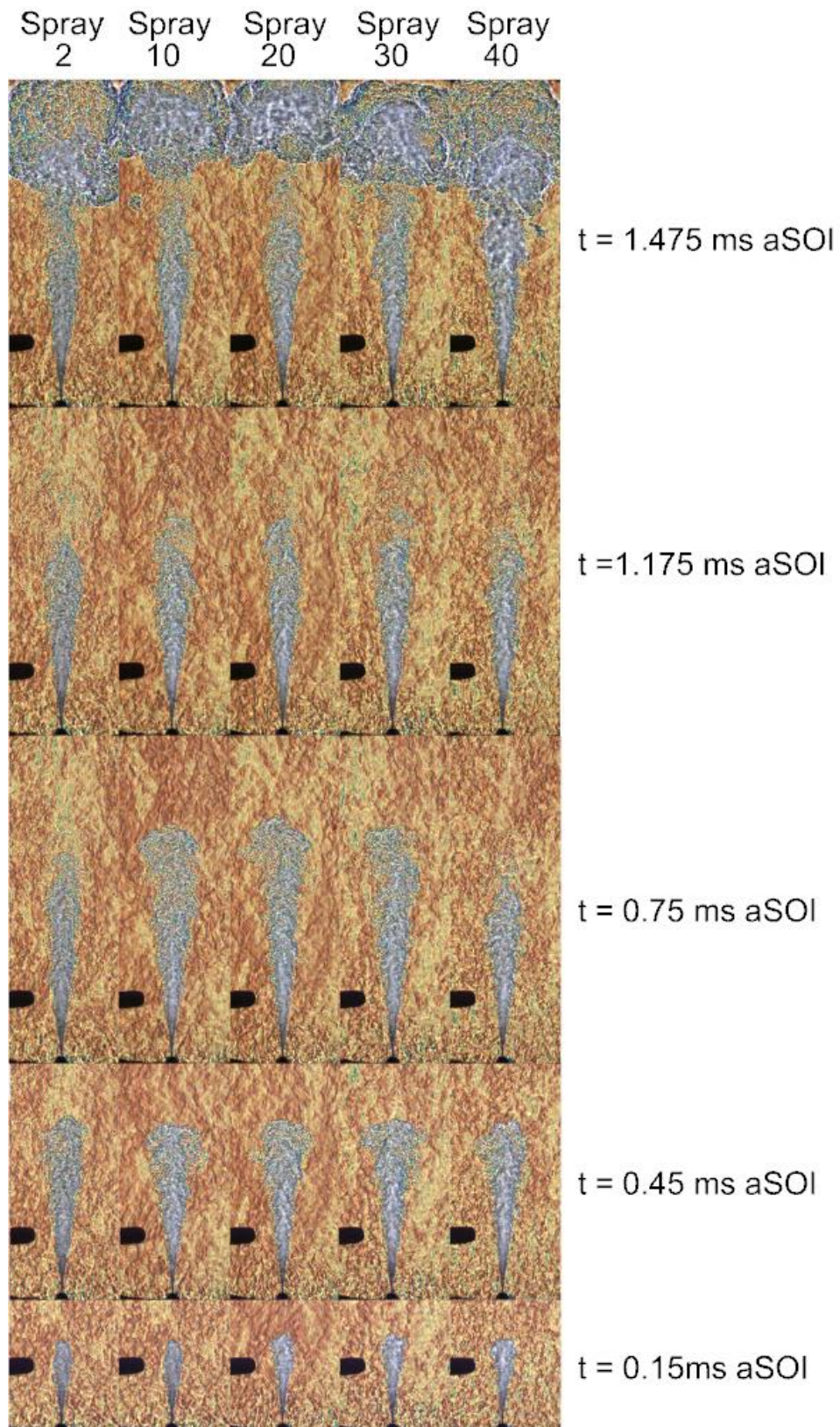


Figure 3.2. Instantaneous RSD images tracking the spray evolution from five separate fuel injections for comparison.

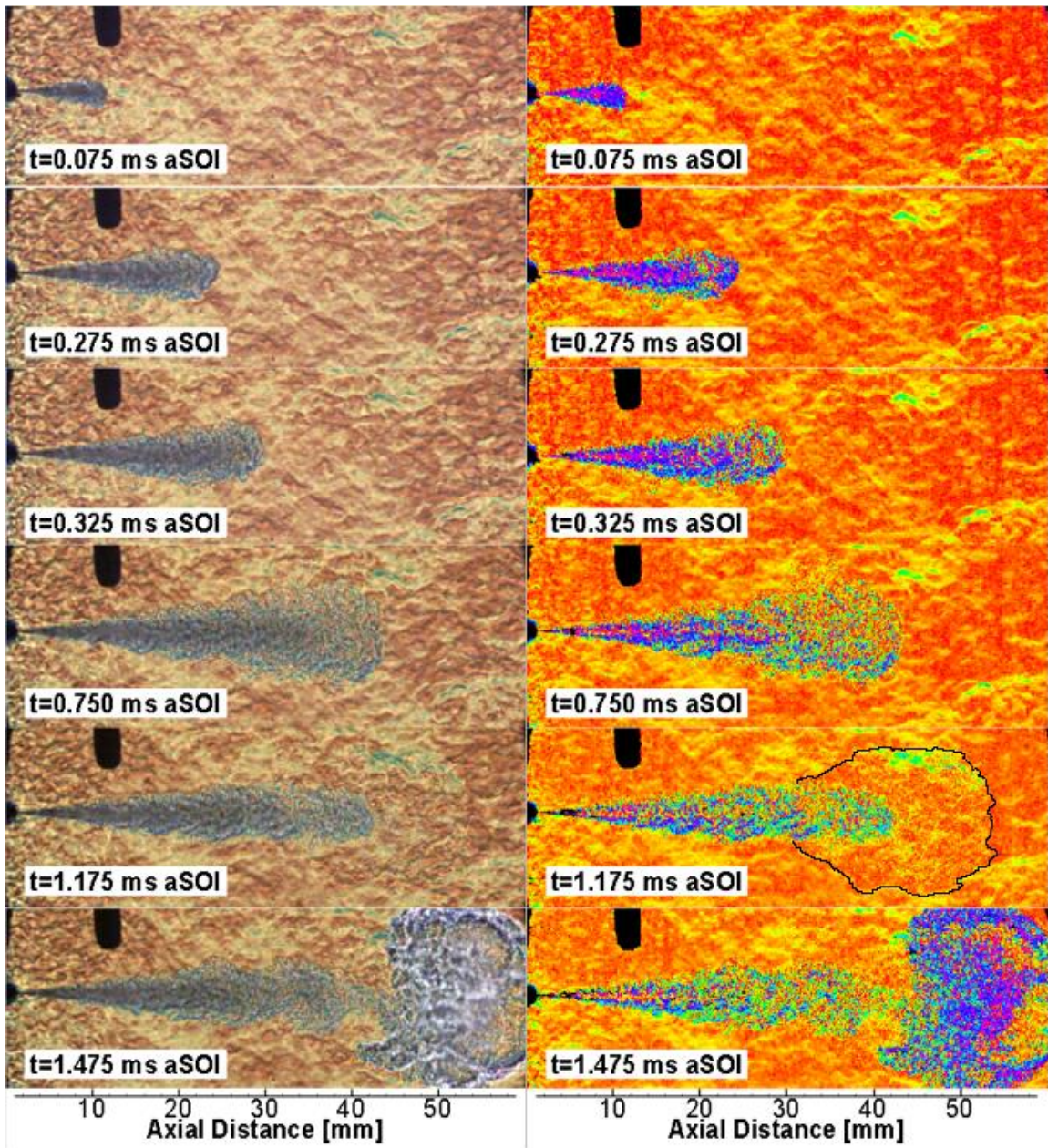


Figure 3.3. Instantaneous RSD images illustrating the spray evolution for a single injection, displaying the measured hue as color. The raw images (left) and the images with maximized intensity and saturation values (right) are shown for visual comparison. For each image the injector (left) and thermocouple (top-left) are blacked-out.

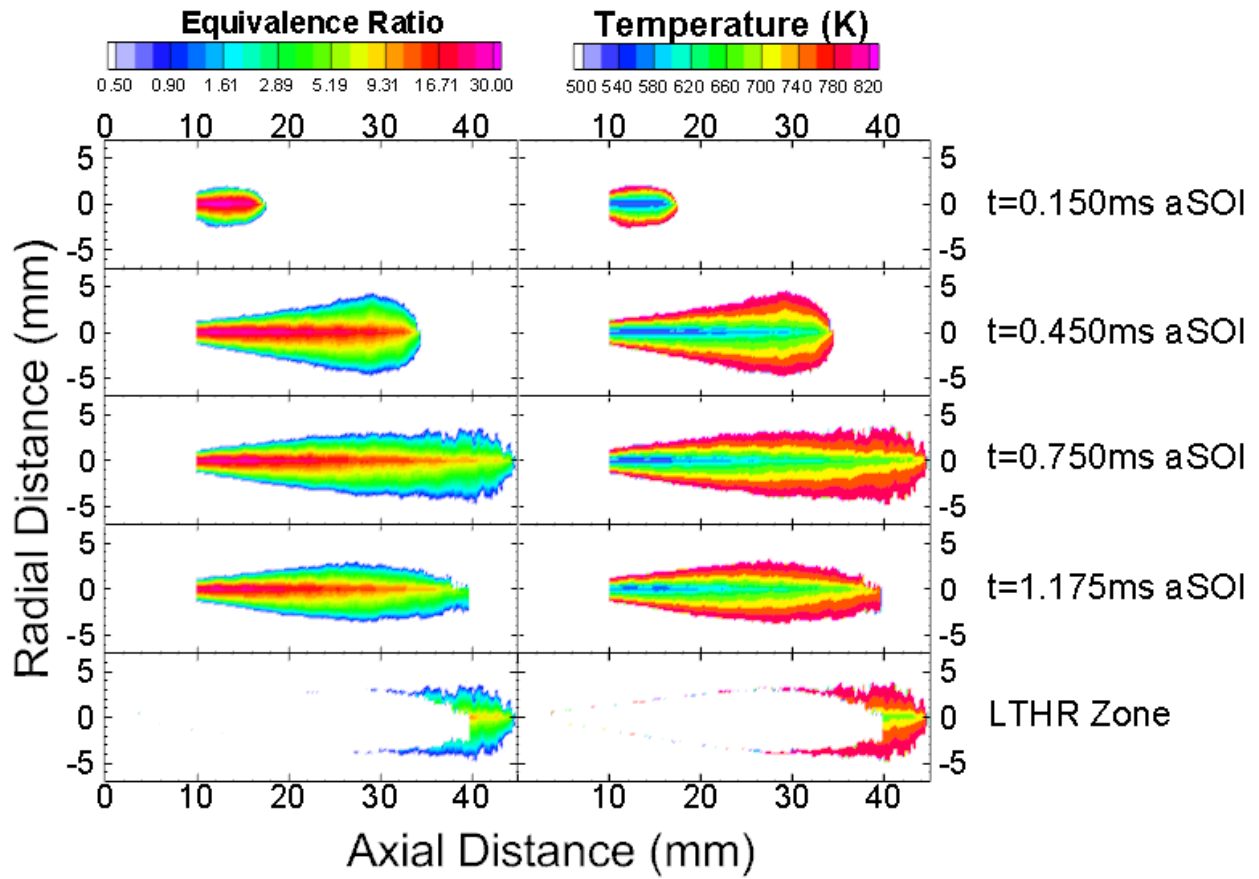


Figure 3.4. Equivalence ratio (left) and temperature (right) contours of jet evolution and for the LTHR zone.

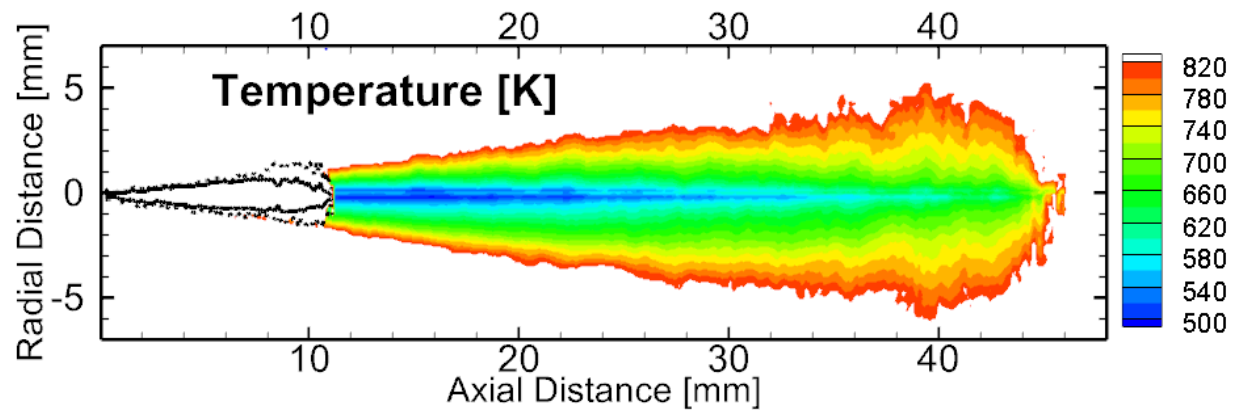


Figure 3.5. Example of liquid boundary detection using relative intensity threshold procedure [26].

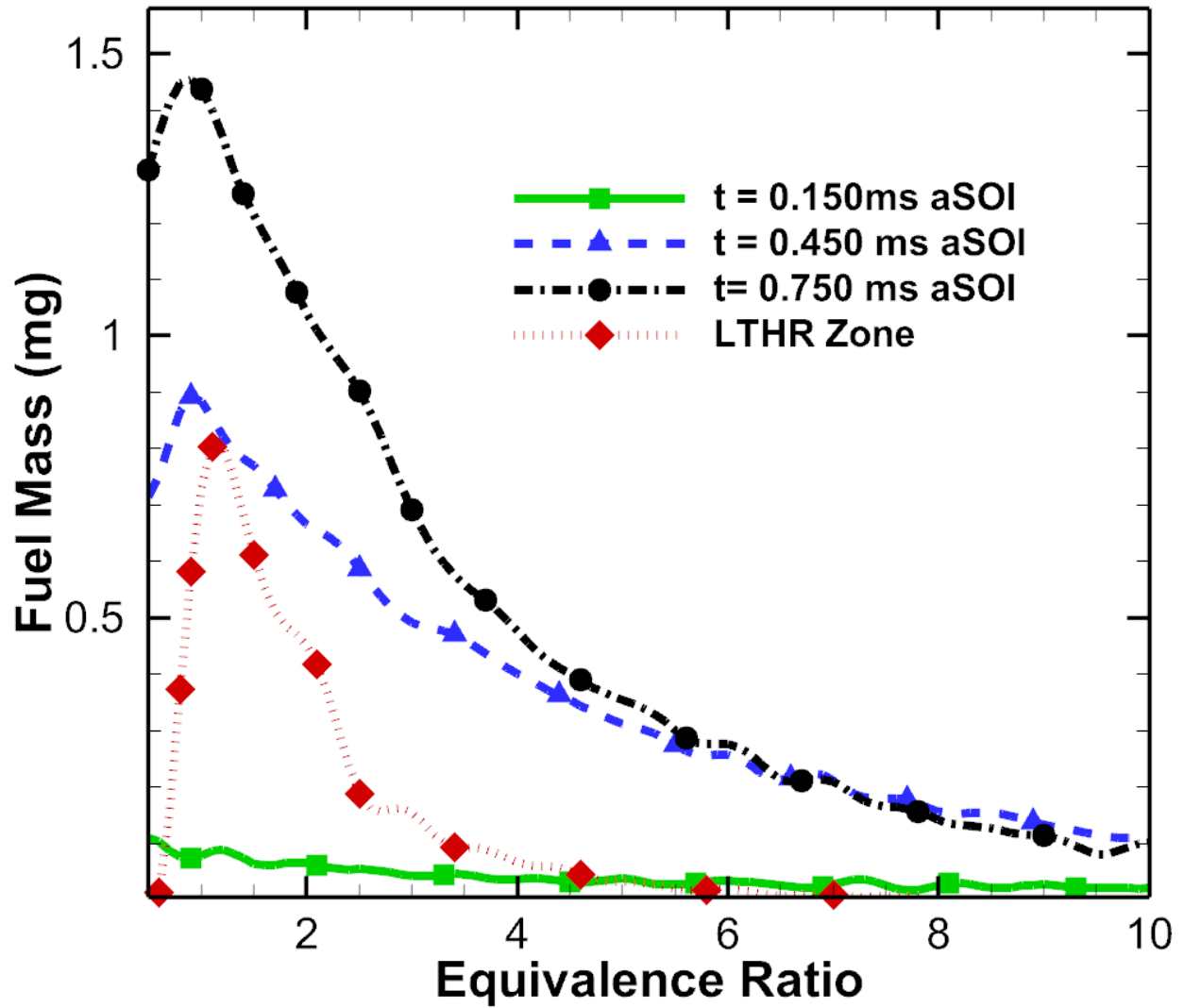


Figure 3.6. Fuel mass present at corresponding equivalence ratios for different time steps of the spray evolution.

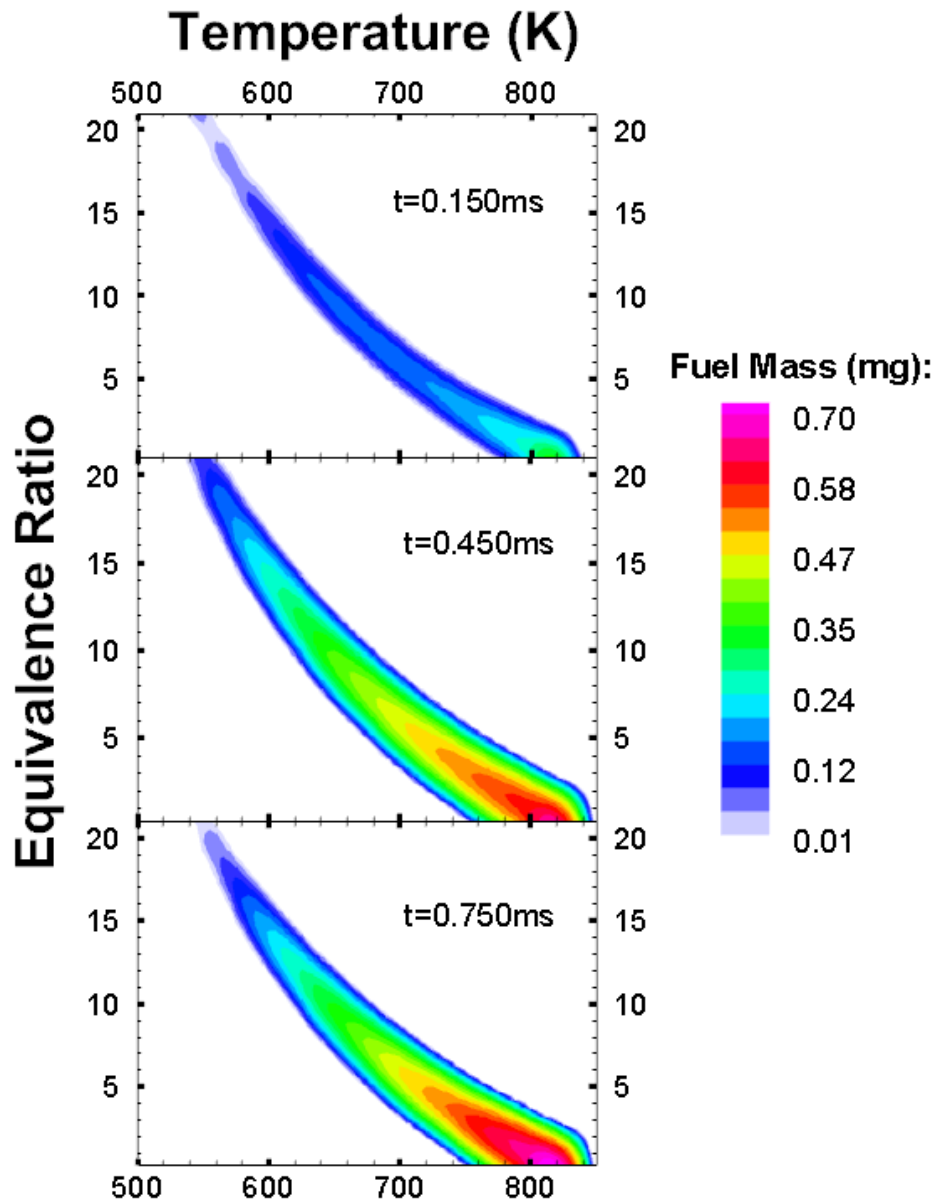
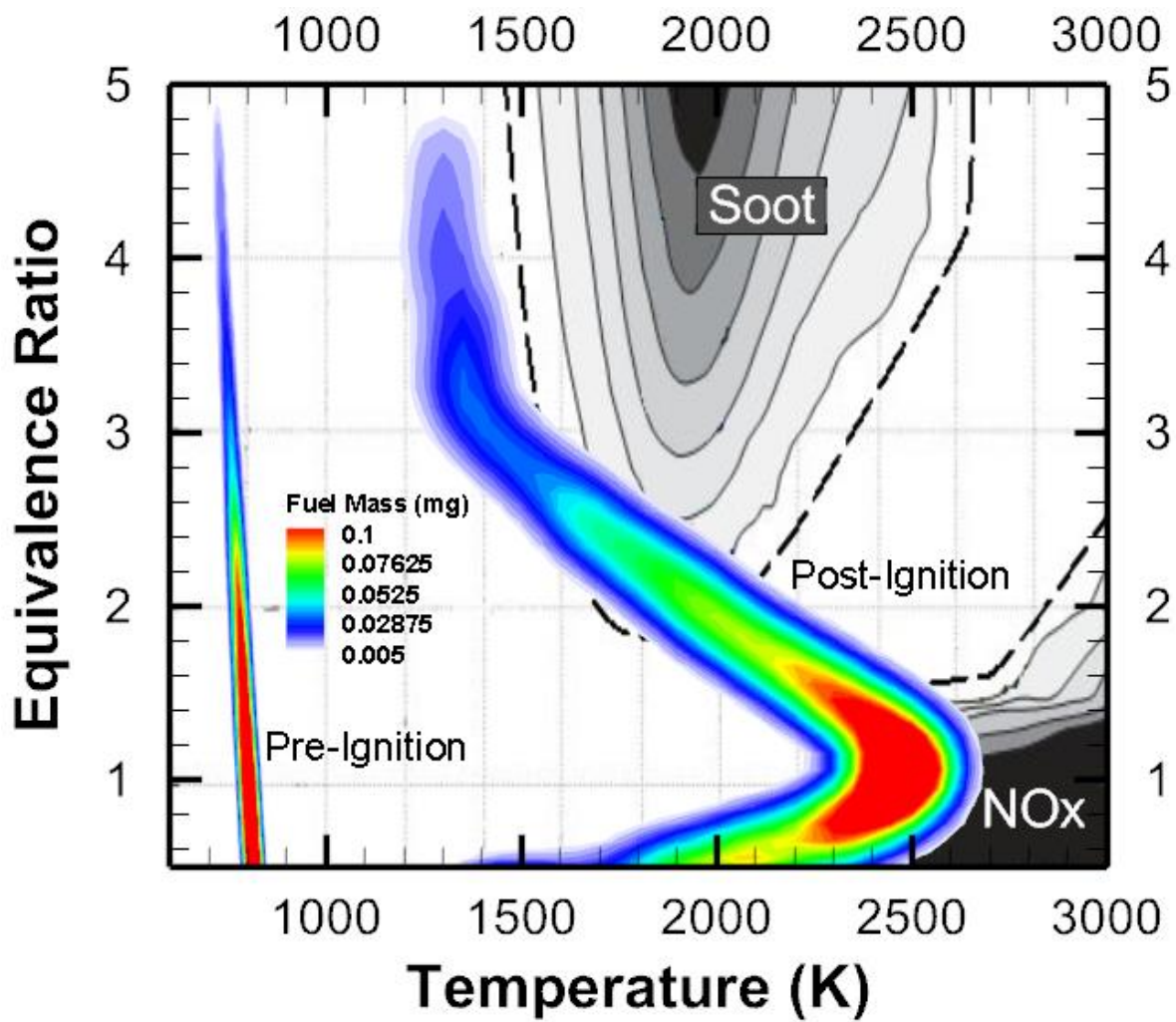
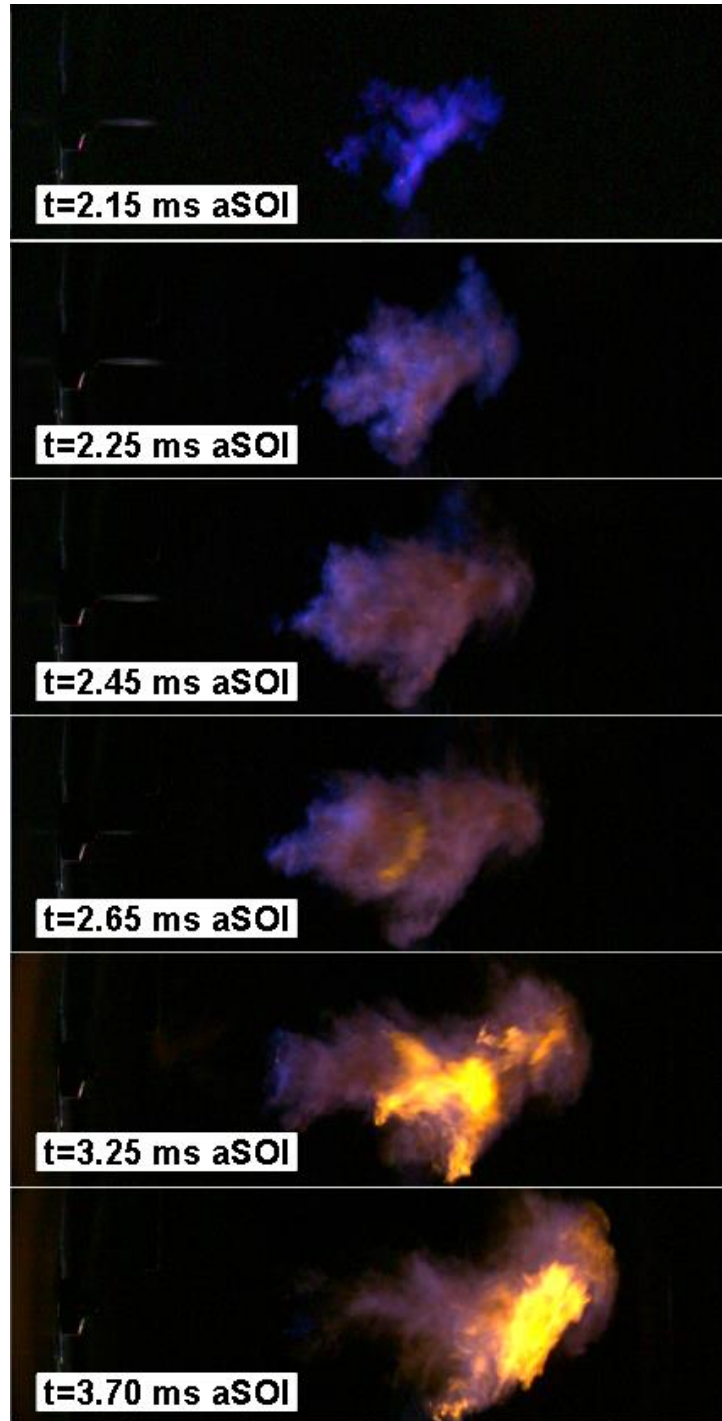


Figure 3.7. Contour map relating the amount of relative fuel mass concentration to equivalence ratio and mixture temperature (K) at different time steps in the spray evolution.



*Figure 3.8.* Contour plot relating the relative fuel mass concentration to equivalence ratio and mixture temperature (K) in the LTHR zone. Pre-ignition (left) refers to the calculated fuel mass in the LTHR zone and post-ignition represents the adiabatic flame temperature results via ANSYS Chemkin.



*Figure 3.9.* Instantaneous optical images of flame combustion and flame propagation at similar experimental conditions: *n*-heptane injected into 33 bar, 785K air.

## CHAPTER 4

### CONCLUSIONS AND RECOMMENDATIONS

With increasing emphasis directed towards limiting toxic emissions and optimizing fuel efficiency in direct-injection IC engine processes, it is necessary to further our understanding of the fuel and air mixing behavior occurring preceding ignition. Various optical diagnostic techniques possess the ability to qualitatively and, in some cases, quantitatively characterize the injection process, however face limitations such as issues with cross-sensitivity in multi-phase regions, requiring virtually particle-free environments, etc. In this study, Rainbow Schlieren Deflectometry provides the capability to quantify local scalar properties of the heterogeneous fuel-air vapor jet downstream of the detected liquid length through line-of-sight deflection measurements. The RSD apparatus, including the constant pressure flow vessel (CPFV), allows for the capturing of 50 injections in a matter of minutes at an excellent framing rate and resolution (40 kHz and 0.1 mm/pixel, respectively) in order to analyze the fuel breakup and mixing processes spanning less than a millisecond. The measured local scalar properties help describe the evolution of the jet and transient fuel-air mixing process, then are used to determine the amount of fuel mass present in a projected three-dimensional jet mixture. The fuel mass coupled with the mixture properties are then put through a chemical equilibrium solver to produce adiabatic flame temperatures via ANSYS Chemkin to predict how combustion ensues following the mixture process.

From the acquired results, one can see that the ambient air mixes well with the initial fuel jet, as enough air is entrained to create relatively lean and hot mixtures as the jet evolves. Fuel mass is recognized to grow in ignition-favorable regions, with equivalence ratios  $0.8 < \phi < 4.0$  and mixture temperatures  $T_{\text{mix}} > 700 \text{ K}$ , as the jet evolves as well. This is likely a result of the rich core of the vapor jet reaching steady state quickly, and subsequent injected fuel penetrating and mixing further downstream axially. Turbulent mixing in the shear layer of this fuel-rich core region contributes to increased fuel-air mixing. The low temperature heat release (LTHR) zone, identified as the region between the jet boundary of the frame before LTHR begins and the jet boundary of the frame before combustion commences, is isolated because the RSD signal is lost in this area. It becomes evident in this region that chemical kinetics are operating in conjunction with early stage fuel breakdown, releasing heat and raising local mixture temperatures to the extent that the refractive index is indistinguishable from that of the ambient air. This makes it impossible to quantify the local scalar properties in this region, but the behavior and eventual combustion can still be inferred from existing measured data. Contour plots exhibit most of the fuel mass initially reacting at near-stoichiometric equivalence ratios, perhaps leading to  $\text{NO}_x$  production from the high-temperature combustion events yet mostly avoiding the dangerous soot generation. While the adiabatic flame temperature does not characterize the entire combustion event, it still provides relevant and useful information in describing how the relative fuel mass concentrations will react.

While there are assumptions made in regards to the mathematical procedures and modeling aspect, as well as inherent measurement uncertainties involved in data acquisition, this study ultimately provides local quantification of the convoluted injection process. Future improvements can be made to more accurately describe this process. For example, if there was a

way to receive an RSD signal in the LTHR region at the frame before combustion occurs as opposed to before LTHR begins, it would provide a more accurate representation of the jet mixture properties immediately before burning. If it remains impossible to attain measurements in this region, then an algorithm predicting subsequent fuel-air mixing and/or jet penetration would assist in more accurately characterizing the reaction process. Also, energy or heat release measurements would assist in detailing the combustion event given the initial mixture conditions. Although the convergence in deflection angle is observed at the 50 image mark, averaging more injections could always improve prediction of the jet behavior.

## REFERENCES

- [1] Davy, M. H., Williams P.A., and Anderson R.W. (2000). Effects of Fuel Composition on Mixture Formation in a Firing Direct-Injection Spark-Ignition (DISI) Engine: An Experimental Study Using Mie-Scattering and Planar Laser-Induced Fluorescence (PLIF) Techniques.” SAE Technical Paper Series, 2000, doi:10.4271/2000-01-1904.
- [2] Adam, A., Leick, P., Bittlinger, G., & Schulz, C. (2009). Visualization of the evaporation of a diesel spray using combined Mie and Rayleigh scattering techniques. *Experiments in Fluids*, 47(3), 439-449. doi:10.1007/s00348-009-0673-y.
- [3] Espey, C., Dec, J., Litzinger, T. and Santavicca, D. (1997). Planar laser rayleigh scattering for quantitative vapor-fuel imaging in a diesel jet. *Combustion and Flame*, 109(1-2), pp.65-86.
- [4] Zhao, H. and Ladommatos, N. (1998). Optical diagnostics for in-cylinder mixture formation measurements in IC engines. *Progress in Energy and Combustion Science*, 24(4), pp.297-336.
- [5] Settles, G. and Covert, E. (2002). Schlieren and Shadowgraph Techniques: Visualizing Phenomena in Transport Media. *Applied Mechanics Reviews*, 55(4), p.B76.
- [6] Siebers, Dennis L. (1998). Liquid-Phase Fuel Penetration in Diesel Sprays. SAE Technical Paper Series, 1998, doi:10.4271/980809.
- [7] Siebers, Dennis L. (1999). Scaling Liquid-Phase Fuel Penetration in Diesel Sprays Based on Mixing-Limited Vaporization. SAE Technical Paper Series, Jan. 1999, doi:10.4271/1999-01-0528.
- [8] Musculus, Mark P. B., and Kattke, Kyle. (2009). Entrainment Waves in Diesel Jets. *SAE International Journal of Engines*, vol. 2, no. 1, 2009, pp. 1170–1193., doi:10.4271/2009-01-1355.
- [9] Pickett, Lyle M., et al. (2011). Relationship Between Diesel Fuel Spray Vapor Penetration/Dispersion and Local Fuel Mixture Fraction. *SAE International Journal of Engines*, vol. 4, no. 1, Dec. 2011, pp. 764–799., doi:10.4271/2011-01-0686.
- [10] Idicheria, Cherian A., and Pickett, Lyle M. (2007). Quantitative Mixing Measurements in a Vaporizing Diesel Spray by Rayleigh Imaging. SAE Technical Paper Series, 2007, doi:10.4271/2007-01-0647.
- [11] Pickett, L., Kook, S. and Williams, T. (2009). Transient Liquid Penetration of Early-Injection Diesel Sprays. *SAE International Journal of Engines*, 2(1), pp.785-804.

- [12] Pickett, Lyle M., et al. (2009). Visualization of Diesel Spray Penetration, Cool-Flame, Ignition, High-Temperature Combustion, and Soot Formation Using High-Speed Imaging. *SAE International Journal of Engines*, vol. 2, no. 1, 2009, pp. 439–459., doi:10.4271/2009-01-0658.
- [13] Idicheria, C. and Pickett, L. (2007). Effect of EGR on diesel premixed-burn equivalence ratio. *Proceedings of the Combustion Institute*, 31(2), pp.2931-2938.
- [14] Fisher, B., Bittle, Wang, J., and Mirynowski E. (2015). Experimental Measurements of n-Heptane Liquid Penetration Distance and Spray Cone Angle for Steady Conditions Relevant to Early Direct-Injection Low-Temperature Combustion in Diesel Engines. *International Journal of Engine Research*, vol. 17, no. 4, July 2015, pp. 371–390., doi:10.1177/1468087415580916.
- [15] Schardin, Hubert. (1947). Toepler's schlieren method: basic principles for its use and quantitative evaluation. Navy Department, David Taylor Model Basin.
- [16] Howes, Walton L. (1983). Rainbow Schlieren. Technical Report TP-2166, National Aeronautics and Space Administration, Scientific and Technical Information Branch, 1983.
- [17] Greenberg, Paul S., et al. (1995). Quantitative Rainbow Schlieren Deflectometry. *Applied Optics*, vol. 34, no. 19, Jan. 1995, p. 3810., doi:10.1364/ao.34.003810.
- [18] Hargather, Michael J., and Gary S. Settles, G.S. (2012). A Comparison of Three Quantitative Schlieren Techniques. *Optics and Lasers in Engineering*, vol. 50, no. 1, 2012, pp. 8–17., doi:10.1016/j.optlaseng.2011.05.012.
- [19] Agrawal, A. K., et al. (2002). Application of Rainbow Schlieren Deflectometry to Measure Temperature and Oxygen Concentration in a Laminar Gas-Jet Diffusion Flame. *Experiments in Fluids*, vol. 32, no. 6, 2002, pp. 689–691., doi:10.1007/s00348-002-0422-y.
- [20] Agrawal, A. K., et al. (1998). Three-Dimensional Rainbow Schlieren Tomography of a Temperature Field in Gas Flows. *Applied Optics*, vol. 37, no. 3, 1998, p. 479., doi:10.1364/ao.37.000479.
- [21] Albers, B. and Agrawal, A. (1999). Schlieren analysis of an oscillating gas-jet diffusion flame. *Combustion and Flame*, 119(1-2), pp.84-94.
- [22] Wong, T. and Agrawal, A. (2006). Quantitative measurements in an unsteady flame using high-speed rainbow schlieren deflectometry. *Measurement Science and Technology*, 17(6), pp.1503-1510.
- [23] Satti, R., Kolhe, P., Olcmen, S. and Agrawal, A. (2007). Miniature rainbow schlieren deflectometry system for quantitative measurements in microjets and flames. *Applied Optics*, 46(15), p.2954.
- [24] Kolhe, P. and Agrawal, A. (2009). Density Measurements in a Supersonic Microjet Using Miniature Rainbow Schlieren Deflectometry. *AIAA Journal*, 47(4), pp.830-838.

- [25] Mirynowski, E., Agrawal, A. K. and Bittle, J. (2017). High-Speed Rainbow Schlieren Deflectometry of n-Heptane Sprays Using a Common Rail Diesel Injector. *Journal of Energy Resources Technology*, 139(6), p.062205.
- [26] Wanstall, T., Agrawal, A., Bittle, J. (2018, May). Quantifying Transient Fuel-Air Mixing in a High Pressure Reacting Spray. Combustion Institute Central States Meeting, Minneapolis, Minnesota. *Applied Optics*, vol. 56, no. 30, 2017, p. 8385., doi:10.1364/ao.56.008385.
- [27] Oefelein, Joseph, et al. (2012). Detailed Modeling and Simulation of High-Pressure Fuel Injection Processes in Diesel Engines. *SAE International Journal of Engines*, vol. 5, no. 3, 2012, pp. 1410–1419., doi:10.4271/2012-01-1258.
- [28] Agrawal, A.K., Wanstall, C.T. (2018). Rainbow Schlieren Deflectometry for Scalar Measurements in Fluid Flows. Manuscript submitted for publication.
- [29] Kolhe, P. and Agrawal, A. (2009). Abel inversion of deflectometric data: comparison of accuracy and noise propagation of existing techniques. *Applied Optics*, 48(20), p.3894.
- [30] Goldstein, R.J., and Kuehn, T.H. (1996). *Optical Systems for Flow Measurement: Shadowgraph, Schlieren, and Interferometric Techniques*. Fluid Mechanics Measurements. Taylor & Francis. New York: Routledge.
- [31] Rubinstein, R. and Greenberg, P. (1994). Rapid inversion of angular deflection data for certain axisymmetric refractive index distributions. *Applied Optics*, 33(7), p.1141.
- [32] Dasch, C.J. (1992). One-dimensional tomography: a comparison of Abel, onion-peeling, and filtered backprojection methods, *Appl. Opt.* 31, 1146–1152 .
- [33] Gardiner, W., Hidaka, Y. and Tanzawa, T. (1981). Refractivity of combustion gases. *Combustion and Flame*, 40, pp.213-219.
- [34] Lemmon, E.W. McLinden M.O., and Friend, D.G., "Thermophysical Properties of Fluid Systems " in *NIST Chemistry WebBook*, NIST Standard Reference Database Number 69, Eds. P.J. Linstrom and W.G. Mallard, National Institute of Standards and Technology, Gaithersburg MD, 20899, doi:10.18434/T4D303.
- [35] Agrawal, A. K., Bittle, J., and Taber Wanstall, C. (2018, May). Quantifying liquid boundary and vapor distributions in a fuel spray by rainbow schlieren deflectometry. *Applied Optics*, 56(30), p.8385.
- [36] ANSYS CHEMKIN 17.0 (15151), ANSYS Reaction Design: San Diego, 2016.

## APPENDIX A

### DATA PROCESSING FOR AVERAGE DEFLECTION ANGLE

This section includes the Matlab code for calculating the deflection angle in the steady portion of the vapor jet and developing the data used to create Figure 3.1. Also included is the Abel inversion technique to find the normalized refractive index difference based on deflection angles throughout the spray, and mixture properties from the normalized refractive index difference.

**%% Average Deflection Code for steady region**

```
[importsettings] = ImportSettingsSetup(2);  
doneback = 0;  
doneavg = 0;
```

**%% Read raw data in**

```
if exist('importsettingsout','var')  
    if ~isequaln(importsettingsout,importsettings)  
        disp('Start Read Raw Data')    end  
end
```

```
[rawdata,importsettingsout,vidheader] = readRSDcine(importsettings,2);
```

```
else  
    disp('Skipping Read Raw Data')  
end
```

```
else  
    disp('Start Read Raw Data')end
```

```
[rawdata,importsettingsout,vidheader] = readRSDcine(importsettings,2);
```

```
end  
load(importsettings.filtercalfileName)  
vidHeight=vidheader.biHeight;  
vidWidth=vidheader.biWidth;
```

**%% convert importsettings to local variables**

```
nInjections=importsettings.nInjectionsread;  
numberofframestoread=importsettings.numberoffframestoread;
```

```

injectortip=importsettings.injectortip;

px_per_mm= importsettings.px_per_mm;
focalLength = importsettings.focalLength; % mm
filtersize_mm=importsettings.filtersize_mm;

total_hue = 360;
filterhue_max = maxhue;
filterhue_min = minhue;
satthreshold =importsettings.satthreshold; %the higher the threshold the more color points in the
spray
valthreshold=importsettings.valthreshold; %higher value means darker liq core and tc
appearance % throws it away if dark this accounts for light not penetrating liquid medium in the
very dense region the Signal to Noise ratio is too low.

%% Read Background
if doneback==0;
    disp('Start Read Background')
    tic
    hue_bg=zeros(vidHeight,vidWidth);
    pixelcount=zeros(vidHeight,vidWidth,'uint16');% intializes the pixelcount %uint16 converts
to unsigned 16-bit integers
    for i = 1:nInjections
        if i ~= importsettings.skipinjections
            hsvframe=rgb2hsv(rawdata(:,:,importsettings.SOIframe,i)); % use second frame for
background data
            hue=hsvframe(:,:,1);

checkbright=(hsvframe(:,:,2)>satthreshold&hsvframe(:,:,3)>valthreshold&hue>filterhue_min/tot
al_hue&hue<filterhue_max/total_hue); %more zeros when threshold is higher% the & only goes
if both are true and returns 1 or 0 if satisfied
            checkhuerange=(hue>filterhue_min/360&hue<filterhue_max/360);
            x=interp1(huefinal,locfinal,hue*total_hue);
            checkisnan=~isnan(x);
            x(~checkisnan)=0;
            allchecks=checkbright.*checkhuerange.*checkisnan;
            hue_bg = hue_bg+hue.*allchecks;

            pixelcount=pixelcount+cast(allchecks,'uint16') ;
        end
    end

    hue_bg=hue_bg./cast(pixelcount,'double')*total_hue; %pixel count factors in bad pixels so no
false average
    hue_bg_small=hue_bg(vidHeight/4:3*vidHeight/4,vidWidth/4:3*vidWidth/4);

```

```

    avg_hue_bg = median(median(hue_bg_small(isfinite(hue_bg_small)))); %taking the avg of
the avg of hue values in square
    xbackground=interp1(huefinal,locfinal,avg_hue_bg);
    doneback=1;
else
    disp('Skipping Read Background')
end

%% average code
if doneavg==0
    disp('Start Process Average')
    deflection=zeros(vidHeight,vidWidth,numberofframestoread,nInjections,'single');

    startframesteady = 30;
    endframesteady = 60;
    for k = startframesteady:endframesteady
        pixelcount=zeros(vidHeight,vidWidth,'uint16');% intializes the pixelcount %uint16 converts
to unsigned 16-bit integers

        for i = 1:nInjections % goes through the nth frame of each injection
            hsvframe=rgb2hsv(rawdata(:,:,:,k,i));

            checkbright=(hsvframe(:,:,2)>satthreshold&hsvframe(:,:,3)>valthreshold&hsvframe(:,:,1)>filterh
ue_min/total_hue&hsvframe(:,:,1)<filterhue_max/total_hue); %more zeros when threshold is
higher% the & only goes if both are true and returns 1 or 0 if satisfied
            try
                x=interp1(huefinal,locfinal,hsvframe(:,:,1)*total_hue);
            catch
                x = nan;
            end
            checkisnan=~isnan(x);
            x(~checkisnan)=0;
            deflection(:,:,k,i) = abs((x-xbackground))/focalLength; .*allchecks; % adding all the hue
in order to average
        end

        deflectionsteady = deflection(:,:,startframesteady:endframesteady,:);
        D = reshape(deflectionsteady,vidHeight,vidWidth,nInjections* (endframesteady-
startframesteady+1));

        doneavg=1;
    end

%% To create deflection angle vs number of images plot
for i = 1:800
    MovingDeflection_far(i) = nanmean(D(70,280,1:i));
end

```

```

    MovingDeflection_med(i)= nanmean(D(75,280,1:i));
    MovingDeflection_close(i)= nanmean(D(80,280,1:i));
end
figure
plot(MovingDeflection_far); hold on
plot(MovingDeflection_med)
plot(MovingDeflection_close)
hold off

%% Send to Tecplot
Ddata=[];
Ddata.Nvar=3;

Ddata.varnames={ 'MovingDeflection_far','MovingDeflection_med','MovingDeflection_close'};
Ddata.lines(1).zonename='R =2.5 mm ';
Ddata.lines(1).x=[1:800];
Ddata.lines(1).y=MovingDeflection_far*180/pi();

Ddata.lines(2).zonename='R = 2.0 mm';
Ddata.lines(2).x=[1:800];
Ddata.lines(2).y=MovingDeflection_med*180/pi();

Ddata.lines(3).zonename='1.5 mm';
Ddata.lines(3).x=[1:800];
Ddata.lines(3).y=MovingDeflection_close*180/pi();

mat2tecplot(Ddata,'Deflection_Angle_Data.plt')

clearvars
load('calibration_5mm_40k.cine.mat')
tdata = [];
tdata.Nvars = 3;
tdata.lines.x = locfinal;
tdata.lines.y = huefinal;
tdata.lines.z = huedevfinal;

tdata.varnames = {'Transverse Displacement [mm]','Measured Filter Hue Value','error'};
mat2tecplot(tdata,'cal_curve.plt')

%% Inversion Calculation
function [del, xf, xferror, Tmix, Tmixerror, Pfuel, Pfuelerror, phi, phierror, ID,
IDerror]=inversion(deflection,P_kPa,T_K,asym,center,edges,injectortip,currenttiploc,calfilenam
e)

```

```

persistent Dm xfcaldata

if isempty(Dm)
    if exist('presolvedDM.mat','file')
        load('presolvedDM.mat')
    else
        error('presolvedDM.mat file not in path');
    end
end

if isempty(xfcaldata)
    if exist(calfilename,'file')
        load(calfilename)
    else
        error([calfilename '.mat file not in path']);
    end
end

% Chamber Operating Conditions
P_chamb=P_kPa;% kPa
T_chamb=T_K; %K
R_bar=8.314;% kPam3/kmolK

% Optical and Spatial Setup settings
k_f= .000518; % gladstone dale afor c7h16 [m3/kg]
MW_f = 100; % molecular weight of heptane [kg/kmol]
k_air = .000226; % gladstone dale for air [m3/kg]
MW_air =28.97; % molecular weight of air [kg/kmol]
AFs_bar=11*4.76;

% One time calculations
kMW_f=k_f*MW_f;
kMW_air=k_air*MW_air;
rho_Bar=P_chamb/T_chamb/R_bar; %kmol/cm3
n_o = 1+rho_Bar*kMW_air; %background refractive index

deflection(isnan(deflection))=0;
del=zeros(size(deflection));
for ax=injectortip:currenttiploc
    toploc=max(3+center(ax),edges(1,ax));
    botloc=min(center(ax)-3,edges(2,ax));

    def_bottom=deflection(center(ax):-1:botloc,ax);
    def_top=deflection(center(ax)+1:toploc,ax);
end

```

```

%Perform Abel inversion of both top and bottom of image
[m_bot,~] = size(def_bottom);
[m_top,~] = size(def_top);
if(asym==0)
    InversionData_Bot = Dm{m_bot}*def_bottom;
else
    InversionData_Bot = -Dm{m_bot}*def_bottom;
end
InversionData_Top = Dm{m_top}*def_top;

%Combine top and bottom inversion data into one image
if(asym==1)
    del(botloc:toploc,ax)=[flipud(InversionData_Bot); InversionData_Top]';
else
    del(botloc:toploc,ax)=-[flipud(InversionData_Bot); InversionData_Top]';
end
end
del=flipud(del);

delcaldata=xfcaldata(1,:);
del(del>max(delcaldata))=max(delcaldata);
del(del<min(delcaldata))=min(delcaldata);

xf=interp1(xfcaldata(:,1),xfcaldata(:,7),del);
xferror=interp1(xfcaldata(:,1),xfcaldata(:,8),del);
phi=interp1(xfcaldata(:,1),xfcaldata(:,9),del);
phierror=interp1(xfcaldata(:,1),xfcaldata(:,10),del);
Tmix=interp1(xfcaldata(:,1),xfcaldata(:,3),del);
Tmixerror=interp1(xfcaldata(:,1),xfcaldata(:,4),del);
Pfuel=interp1(xfcaldata(:,1),xfcaldata(:,5),del);
Pfuelerror=interp1(xfcaldata(:,1),xfcaldata(:,6),del);
ID=interp1(xfcaldata(1:19,11),xfcaldata(1:19,13),del);
IDerror=interp1(xfcaldata(1:19,11),xfcaldata(1:19,14),del);

end

```

## APPENDIX B

### DATA PROCESSING FOR SPRAY EVOLUTION

This section reveals the Matlab code used to generate the equivalence ratio and mixture temperature contour plots seen in the results section.

```
clf;
clear phi_tr Tmix_tr r rc roundc edge Tmix_int phi_int phi_interest T_interest react_phi react_T
T_vect phi_vect a b;
saveoutvideo=1;
if(saveoutvideo)
    v = VideoWriter('newfile.mp4','MPEG-4');
    v.FrameRate=5;
    open(v);
end
px_per_mm=importsettings.px_per_mm;
vidHeight=200;
vidWidth=608;
startframe=40;
endframe=57;
k=40; % frame before LTHR
j=57; % frame before combustion
center_new=105;
phithresh=0.25;
currenttiploc(endframe)=397; % was 586 % frame before combustion

%% Phi Contour and Phi-T Cloudplot Evolution Video
f=figure(99);
f.Name='Cloudplot and Contour Evolution';
f.Color='w';
for frame=startframe:endframe
    dim = [.4 .25 .3 .3];
    str = ['t = ' sprintf('%.3f',(cast((frame),'double')*importsettings.framestep-
importsettings.SOIframe)*importsettings.period/1000) 'ms aSOI'];
    annotation('textbox',dim,...
        'String',str,...
        'BackgroundColor',[1,1,1],...
        'FitBoxToText','on');
```

```

for ax=1:currenttiploc(frame)
top=min(find(phi(center_new:end,ax,frame)<phithresh,1,'first')-1,vidHeight-
importsettings.injectortip(2));
bot=find(phi(center_new:-1:1,ax,frame)<phithresh,1,'first')-1;
edge(:,ax,frame)=[center_new+top center_new-bot];
szedge=size(edge);
edge_j=zeros(szedge);
overlay_phi=zeros(2,436);
overlay_pos=zeros(2,436);
halfwidth(ax)=(edge(1,ax,frame)-center_new);
top_edge(ax,frame)=edge(1,ax,k);
bot_edge(ax,frame)=edge(2,ax,k);

```

**%Edge of Frame Before Ignition to Overlay on Max Penetration Frame**

```

for axj= 1:currenttiploc(j)

```

```

top_j=min(find(phi(center_new:end,axj,j)<phithresh,1,'first')-1,vidHeight-
importsettings.injectortip(2));
bot_j=find(phi(center_new:-1:1,axj,j)<phithresh,1,'first')-1;
edge_j(:,axj,j)=[center_new+top_j center_new-bot_j];
overlay_phi(:,axj,j)=[phi(edge_j(1,axj,j),axj,k) phi(edge_j(2,axj,j),axj,k)];
overlay_pos(:,axj,j)=[(edge_j(1,axj,j)) (edge_j(2,axj,j))];

```

```

end

```

```

end

```

**%Phi-T CloudPlot**

```

subplot(2,2,1);
axis equal;
Range=[0:20:200];
cloudPlot(Tmix(:, :, frame), phi(:, :, frame), [650 800 0 15], [], [100 100], xlabel('Temperature (K)'),
ylabel('Phi'); colorbar('YTick', Range, 'YTickLabel', Range); set(colorbar, 'ylim', [0
200]); caxis([0, 200]);
colormap('jet')

```

**%Phi Contour**

```

subplot(2,2,2);
axis equal;
Contours=logspace(log(.1)/log(10),...
log(100)/log(10),20);
contourf(log(phi(:, :, frame)), log(Contours), 'edgecolor', 'none');
colorbar('Ytick', log(Contours(2:2:end)), 'Yticklabel', Contours(2:2:end)); colormap(jet);
set(gca, 'XTick', [10 20 30 40 50 60]*px_per_mm)
set(gca, 'XTickLabel', [10 20 30 40 50 60])
set(gca, 'YTick', importsettings.injectortip(2) + [-10 -5 0 5 10]*px_per_mm)

```

```

set(gca, 'YTickLabel', [-10 -5 0 5 10])
ylabel('Radial distance [mm]')
xlabel('Axial Position [mm]')
title('Phi Contour')

%phi PDF
subplot(2,2,3);
a=phi(:, :, frame);
b=a(:);
[y, loc]= find(5> b & b > 0.1037);
b_chemk= b(y);
rich=b_chemk(b_chemk>1.1);
rich=sortrows(rich);
lean=b_chemk(b_chemk<.9);
lean=sortrows(lean);
middle=b_chemk(.9<b_chemk & b_chemk<1.1);
middle=sortrows(middle);
lean_spacing=lean(1:30:end);
rich_spacing=rich(1:30:end);
middle_spacing=middle(1:15:end);
phi_vect=[lean_spacing;middle_spacing;rich_spacing];
[point, loc]=find(phi_vect);
histfit(b, [], 'kernel'), xlim([.25 10]), ylim([0 1000]), xlabel('Phi');

%Temperature PDF
subplot(2,2,4);
at=Tmix(:, :, frame);
bt=at(:);
bt_chemk= bt(y);
T_vect= bt_chemk(point);
histfit(bt, [], 'kernel'), xlim([400 850]), ylim([0 1000]), xlabel('Temperature');

    pause(.1)
end

if(saveoutvideo==1)

    close(v);
end
%% Phi and Tmix for LTHR Region and Max Penetration Region
inner_top=overlay_pos(1,:);
inner_bot=overlay_pos(2,:);
inner_top(397:436)=105;
inner_bot(397:436)=105;
outer_top=edge(1, :, 40);

```

```

outer_bot=edge(2, :, 40);

phi_ign_bot=zeros(size(phi));
phi_ign_top=zeros(size(phi));
T_ign_bot=zeros(size(Tmix));
T_ign_top=zeros(size(Tmix));
phi_pen_top=zeros(size(phi));
phi_pen_bot=zeros(size(phi));
T_pen_top=zeros(size(phi));
T_pen_bot=zeros(size(phi));

    for m = 1:length(inner_top)
% Ignition Region
        phi_ign_bot(outer_bot(m)+1:inner_bot(m),m,40)=phi(outer_bot(m)+1:inner_bot(m),m,40);
        phi_ign_top(inner_top(m)+1:outer_top(m),m,40)=phi(inner_top(m)+1:outer_top(m),m,40);
T_ign_bot(outer_bot(m)+1:inner_bot(m),m,40)=Tmix(outer_bot(m)+1:inner_bot(m),m,40);
T_ign_top(inner_top(m)+1:outer_top(m),m,40)=Tmix(inner_top(m)+1:outer_top(m),m,40);

% Max Penetration Region
        phi_pen_bot(outer_bot(m)+1:center_new,m,40)=phi(outer_bot(m)+1:center_new,m,40);
        phi_pen_top(center_new+1:outer_top(m),m,40)=phi(center_new+1:outer_top(m),m,40);
        T_pen_bot(outer_bot(m)+1:center_new,m,40)=Tmix(outer_bot(m)+1:center_new,m,40);
        T_pen_top(center_new:outer_top(m),m,40)=Tmix(center_new:outer_top(m),m,40);
    end
% Phi-T for LTHR Region Formatted for Import to Chemkin
phi_frame_ign_top=phi_ign_top(:, :, 40);
phi_frame_ign_bot=phi_ign_bot(:, :, 40);
phi_frame_ign=phi_ign_top+phi_ign_bot;

T_frame_ign_top=T_ign_top(:, :, 40);
T_frame_ign_bot=T_ign_bot(:, :, 40);
a_top=phi_frame_ign_top(:);
a_bot=phi_frame_ign_bot(:);
b_top=T_frame_ign_top(:);
b_bot=T_frame_ign_bot(:);
[y_top, loc]=find(5 > a_top & a_top > 0.1037);
[y_bot, loc]=find(5 > a_bot & a_bot > 0.1037);
a_top_thresh=a_top(y_top);
a_bot_thresh=a_bot(y_bot);
b_top_thresh=b_top(y_top);
b_bot_thresh= b_bot(y_bot);
phi_ign=[a_top_thresh(:); a_bot_thresh(:)];
T_ign=[b_top_thresh(:); b_bot_thresh(:)];
Ign_val1=[phi_ign T_ign];
Ign_val=sortrows(Ign_val1);
[lean, loc]=find(Ign_val(:, 1)<0.9);

```

```

[rich, loc]=find(Ign_val(:,1)>1.1);
[middle, loc]=find(.901<Ign_val(:,1) & Ign_val(:,1)<1.101);
lean_spacing = lean(1,1):25:lean(end);lean_spacing =lean_spacing';
rich_spacing = rich(1,1):25:rich(end);rich_spacing =rich_spacing';
middle_spacing= middle(1,1):10:middle(end);middle_spacing=middle_spacing';
effic_phi_lean=Ign_val(lean_spacing);
effic_phi_rich=Ign_val(rich_spacing);
effic_phi_middle=Ign_val(middle_spacing);
effic=[lean_spacing;middle_spacing;rich_spacing];
effic_phi=[effic_phi_lean;effic_phi_middle;effic_phi_rich];
[point, loc]=find(effic_phi);
effic_T=T_ign(effic);
Chemkin=[effic_phi effic_T];

```

### %Phi-T for Max Penetration for Import to Chemkin

```

phi_pen_ign_top=phi_pen_top(:,40);
phi_pen_ign_bot=phi_pen_bot(:,40);
T_pen_top_frame=T_pen_top(:,40);
T_pen_bot_frame=T_pen_bot(:,40);
a_pen_top=phi_pen_ign_top(:);
a_pen_bot=phi_pen_ign_bot(:);
b_pen_top=T_pen_top_frame(:);
b_pen_bot=T_pen_bot_frame(:);
[y_pen_top,loc]=find(5> a_pen_top & a_pen_top > 0.1037);
[y_pen_bot,loc]=find(5> a_pen_bot & a_pen_bot > 0.1037);
a_top_pen_thresh=a_pen_top(y_pen_top);
a_bot_pen_thresh=a_pen_bot(y_pen_bot);
b_top_pen_thresh=b_pen_top(y_pen_top);
b_bot_pen_thresh= b_pen_bot(y_pen_bot);
phi_pen_thresh=[a_top_pen_thresh(:); a_bot_pen_thresh(:)];
T_pen_thresh=[b_top_pen_thresh(:); b_bot_pen_thresh(:)];
pen_val1=[phi_ign T_ign];
pen_val=sortrows(Ign_val1);
[lean_pen, loc]=find(pen_val(:,1)<0.9);
[rich_pen, loc]=find(pen_val(:,1)>1.1);
[middle_pen, loc]=find(.901<pen_val(:,1) & pen_val(:,1)<1.101);
lean_spacing_pen = lean_pen(1,1):25:lean_pen(end);lean_spacing_pen =lean_spacing_pen';
rich_spacing_pen = rich_pen(1,1):25:rich_pen(end);rich_spacing_pen =rich_spacing_pen';
middle_spacing_pen=
middle_pen(1,1):10:middle_pen(end);middle_spacing_pen=middle_spacing_pen';
effic_phi_lean_pen=Ign_val(lean_spacing);
effic_phi_rich_pen=Ign_val(rich_spacing);
effic_phi_middle_pen=Ign_val(middle_spacing);
effic_pen=[lean_spacing_pen;middle_spacing_pen;rich_spacing_pen];
effic_phi_pen=[effic_phi_lean_pen;effic_phi_middle_pen;effic_phi_rich_pen];
effic_T_pen=T_pen_thresh(effic_pen);

```

### %Chemkin Equilibrium Flame Temperature

T\_eq=[1121.622 1121.622 1382.133 1419.688 1447.835 1457.017 1447.829  
1472.164 1480.116 1508.341 1536.757 1528.544 1545.04 1589.174 1615.44  
1616.767 1630.582 1648.444 1667.428 1717.495 1723.577 1760.244 1802.584  
1811.062 1869.396 1923.484 1929.051 1944.182 1936.392 1985.702 1996.33  
1997.95 2023.681 2044.502 2026.432 2090.167 2090.785 2078.21 2114.651  
2135.829 2153.11 2187.343 2167.483 2159.872 2188.273 2250.931 2271.101  
2277.562 2289.114 2303.57 2297.539 2307.853 2352.558 2340.44 2324.33 2347.18  
2366.561 2381.58 2427.218 2437.245 2438.364 2427.419 2460.082 2453.008  
2461.752 2443.772 2470.417 2472.792 2468.561 2471.307 2484.261 2447.044  
2481.53 2483.861 2477.955 2491.972 2473.83 2498.157 2473.332 2505.874  
2498.257 2470.971 2507.551 2490.476 2506.415 2513.338 2523.502 2496.336  
2484.124 2518.982 2516.063 2518.653 2524.768 2526.765 2530.543 2532.637  
2532.968 2534.378 2535.197 2535.602 2535.177 2535.92 2536.77 2531.771 2524.38  
2534.607 2523.213 2519.72 2519.295 2514.544 2505.254 2492.911 2494.508  
2493.011 2472.125 2465.209 2448.209 2433.83 2422.245 2436.98 2423.138  
2383.514 2386.911 2351.298 2348.577 2324.612 2333.947 2328.559 2284.565  
2290.02 2259.074 2254.317 2247.877 2231.414 2201.679 2200.706 2194.3 2126.079  
2127.036 2130.285 2115.168 2040.427 2060.941 2053.316 2034.375 2036.176  
1966.006 1966.278 1962.332 1952.332 1942.629 1934.855 1850.726 1852.54  
1843.352 1831.29 1814.233 1802.536 1706.761 1699.573 1693.429 1683.597  
1672.347 1632.745 1614.343 1599.52 1505.093 1516.806 1479.138 1468.508  
1380.488 1370.273 1386.98 1409.385 1340.085 1372.874 1362.704 1356.968  
1357.975 1356.431 1356.831 1347.969 1338.514 1326.247 1315.321 1316.687  
1317.791 1320.469 1321.145 1311.571]';

### %Correponding Chemkin Equivalence Ratios

phi\_eq=[0.128694 0.128694 0.229097 0.251668 0.257882 0.261508 0.267339  
0.273086 0.281624 0.29127 0.297459 0.304176 0.311723 0.321888 0.334199  
0.341298 0.347064 0.355884 0.369846 0.383961 0.408039 0.421228 0.439136  
0.456574 0.476091 0.488621 0.498563 0.507154 0.513313 0.522725 0.529224  
0.541554 0.553256 0.562189 0.572099 0.583124 0.596973 0.606573 0.621846  
0.629123 0.638041 0.65322 0.662439 0.673164 0.682177 0.692613 0.701898  
0.709765 0.722642 0.736309 0.745017 0.757132 0.771889 0.785844 0.798584  
0.810668 0.824142 0.837499 0.849827 0.862578 0.872213 0.89105 0.901395  
0.906166 0.910475 0.913623 0.917146 0.919829 0.923132 0.926319 0.935954  
0.93862 0.941938 0.948524 0.954308 0.95789 0.965152 0.971807 0.977501  
0.986398 0.991369 0.996039 0.998669 1.002539 1.009369 1.016368 1.021929  
1.025938 1.029671 1.035384 1.038978 1.050111 1.057606 1.064397 1.069091  
1.074334 1.079255 1.084295 1.090022 1.093872 1.097935 1.100034 1.110977  
1.124876 1.146736 1.155937 1.180179 1.197702 1.211547 1.225733 1.244815  
1.261653 1.276324 1.289174 1.306366 1.323405 1.345503 1.365058 1.379923  
1.391314 1.414176 1.431584 1.451608 1.472868 1.49469 1.511123 1.527559  
1.548661 1.579008 1.593652 1.617169 1.640484 1.660404 1.690933 1.711199  
1.735046 1.762382 1.778323 1.805744 1.831827 1.865735 1.893825 1.915947  
1.944789 1.981004 2.000812 2.023706 2.050333 2.084368 2.126473 2.161949

```

2.189076  2.224126  2.255564  2.289164  2.327128  2.365902  2.40024  2.444525
2.497556  2.537334  2.580909  2.621578  2.679506  2.733313  2.793168  2.835137
2.883231  2.966046  3.021234  3.072465  3.141307  3.217053  3.289777  3.360162
3.439881  3.513172  3.586493  3.675259  3.779577  3.846675  3.96239  4.063479
4.159978  4.3023  4.392064  4.490452  4.66109  4.768895  4.87712];
clf;
figure(1)
%low-pass filter
ex=fir1(60,0.1);
plex=filtfilt(ex,1,T_eq);
%phi-T plot of LTHR Region, Post and Pre-Ignition
plot(T_ign,phi_ign,'r'); hold on
plot(plex,phi_eq,'b'); %hold on
plot(T_eq,phi_eq,'g'), legend('Initial Conditions', 'Filtered Flame Temp','Original Flame Temp'),
xlabel('Temperature (K)'), ylabel('Equivalence Ratio')
hold off
%% %phi-T Cloudplot of LTHR Region, Post and Pre-Ignition
T_cloudplot=[T_eq; effic_T];
phi_cloudplot=[phi_eq;effic_phi];
figure(2)
axis equal;
cloudPlot(T_cloudplot,phi_cloudplot,[0 2600 0 5], [], [100 100]),xlabel('Temperature (K)'),
ylabel('Phi'); colorbar; %hold on%('YTick',Range,'YTickLabel',Range);set(colorbar,'ylim',[0
200]);caxis([0,200]);
colormap('jet')

```

## APPENDIX C

### FUEL MASS CALCULATION

In this section, the code used to create pixel volumes for each location throughout the spray is displayed. Likewise, the fuel mass is calculated and weighted according to the pixel volumes. The code for the fuel concentration contour plots is also included.

```
%% Fuel Mass Calculations
```

```
m_air=28.97; P_air=2800;R_air=.287; AF_s=15.1;  
mass_fuel=AF_s*m_air*phi;
```

```
T_frame_ign=T_ign_top+T_ign_bot;  
phi_frame_ign40=phi_frame_ign(:,:,40);  
phi_max_pen_bot=zeros(size(phi));  
phi_max_pen_top=zeros(size(phi));  
T_max_pen_top=zeros(size(phi));  
T_max_pen_bot=zeros(size(phi)); mass_fuel_weight=zeros(size(phi));  
v_cell=zeros(size(phi)); rho_air=zeros(size(phi));rho_fuel=zeros(size(phi));
```

```
clear phi_low phi_high ;  
clear outer_top_frame outer_bot_frame edge_frame top_frame bot_frame X_pen Y_pen evolu;  
saveoutvideo=1;  
if(saveoutvideo)  
    v = VideoWriter('newfile.mp4','MPEG-4');  
    v.FrameRate=5;  
    open(v);  
end  
clf;  
f=figure(98);  
f.Name='Mass-Phi Evolution';  
f.Color='w';
```

```
%%
```

```
for evol=16:40
```

```
    dim = [.6 .1 .3 .3];  
    str = ['t = ' sprintf('% .3f',(cast((evol),'double'))*importsettings.framestep-  
importsettings.SOIframe)*importsettings.period/1000) 'ms aSOI'];
```

```

annotation('textbox',dim,...
    'String',str,...
    'BackgroundColor',[1,1,1],...
    'FitBoxToText','on');
dim = [.3 .1 .3 .3];
str1 = ['frame = ' sprintf('%.0f',(cast((evol),'double')))];
annotation('textbox',dim,...
    'String',str1,...
    'BackgroundColor',[1,1,1],...
    'FitBoxToText','on');

for mi = 106:currenttiploc(evol)

%identify boundary of jet in each frame
    top_frame=min(find(phi(center_new:end,mi,evol)<phithresh,1,'first')-1,vidHeight-
importsettings.injectortip(2));
    bot_frame=find(phi(center_new:-1:1,mi,evol)<phithresh,1,'first')-1;
    edge_frame(:,mi,evol)=[center_new+top_frame center_new-bot_frame];
    outer_top_frame(mi,evol)=edge_frame(1,mi,evol);
    outer_bot_frame(mi,evol)=edge_frame(2,mi,evol);

%Mixture temp for each location in jet
T_max_pen_bot(outer_bot_frame(mi,evol)+1:center_new,mi,evol)=Tmix(outer_bot_frame(mi,e
vol)+1:center_new,mi,evol);

T_max_pen_top(center_new+1:outer_top_frame(mi,evol),mi,evol)=Tmix(center_new+1:outer_t
op_frame(mi,evol),mi,evol);

T_max_pen=T_max_pen_top+T_max_pen_bot;

%Equivalence Ratio for each location in jet
phi_max_pen_bot(outer_bot_frame(mi,evol)+1:center_new,mi,evol)=phi(outer_bot_frame(mi,ev
ol)+1:center_new,mi,evol);

phi_max_pen_top(center_new+1:outer_top_frame(mi,evol),mi,evol)=phi(center_new+1:outer_to
p_frame(mi,evol),mi,evol);

phi_max_pen=phi_max_pen_top+phi_max_pen_bot;

for n=1:vidHeight;
    if Tmix(n,mi,evol) ~= 0
dist=abs(105-n);
dist_mm=dist*1/importsettings.px_per_mm;
rho_air(n,mi,evol)=P_air/(R_air*Tmix(n,mi,evol));
rho_fuel(n,mi,evol)=refpropm2D('D','T', Tmix(n,mi,evol), 'P',2800,'heptane');

```

```

%Pixel Volume based on radial distance from centerline
v_cell(n,mi,evol)=(((pi*(dist_mm+1/importsettings.px_per_mm)^2pi*dist_mm^2)*1/importsetti
ngs.px_per_mm))/2*10^-9;
%Fuel Mass for each location in spray
mass_fuel_weight(n,mi,evol)=v_cell(n,mi,evol)/(1/rho_fuel(n,mi,evol)+AF_s/(phi_max_pen(n,
mi,evol)*rho_air(n,mi,evol)))*10^6;
%Fuel Mass for LTHR zone
mass_fuel_weight_ign(n,mi,evol)=v_cell(n,mi,evol)/(1/rho_fuel(n,mi,evol)+AF_s/(phi_frame_ig
n(n,mi,evol)*rho_air(n,mi,evol)))*10^6;
    end
    end

    end

%% Fuel and Air Densities at each pixel
v_cell_frame=v_cell(:, :,evol);
v_cellframe_col=v_cell_frame(:);

rho_fuel_frame=rho_fuel(:, :,evol);
rho_fuelframe_col=rho_fuel_frame(:);

rho_airframe=rho_air(:, :,evol);
rho_airframe_col=rho_airframe(:);

phi_pen_frame=phi_max_pen(:, :,evol);
phi_penframe_col=phi_pen_frame(:);

%Ignition Variables
phi_frame_ign40_col=phi_frame_ign40(:);

T_frame_ign40=T_frame_ign(:, :,40);
T_frame_ign40_col=T_frame_ign40(:);

count=0;
delta_phi=0.1;

%Calculating Fuel Mass in delta_phi=0.1 steps for fuel concentration contour plots

for phi_low=0.5:delta_phi:20;
    count=count+1;
%Max penetration mass
evolu(evol).test(count).cdata:=(count+1)/10;
Test(count)=(count+1)/10;
phi_high=phi_low+ delta_phi;

```

```

evolu(evol).pen_loc(count).cdata(:)= find(phi_max_pen(:, :, evol)>phi_low &
phi_max_pen(:, :, evol)<phi_high);
evolu(evol).v_cell_pen_loc(count).cdata(:)=v_cellframe_col(evolu(evol).pen_loc(count).cdata(:)
);
evolu(evol).rho_fuel_pen_loc(count).cdata(:)=rho_fuelframe_col(evolu(evol).pen_loc(count).cdata(:));
evolu(evol).rho_air_pen_loc(count).cdata(:)=rho_airframe_col(evolu(evol).pen_loc(count).cdata(:));
evolu(evol).phi_pen_unweight(count).cdata(:)=phi_pen_frame(phi_penframe_col>phi_low &
phi_penframe_col<phi_high); % max penetration phi unweighted

evolu(evol).A_pen(count).cdata(:)=AF_s/evolu(evol).phi_pen_unweight(count).cdata(:);
evolu(evol).B_pen(count).cdata(:)=evolu(evol).A_pen(count).cdata(:)./
evolu(evol).rho_air_pen_loc(count).cdata(:);
evolu(evol).C_pen(count).cdata(:)=1./ evolu(evol).rho_fuel_pen_loc(count).cdata(:);
evolu(evol).Mf_pen_weight(count).cdata(:)=evolu(evol).v_cell_pen_loc(count).cdata(:)/(evolu(
evol).C_pen(count).cdata(:)+evolu(evol).B_pen(count).cdata(:))*10^6;

% LTHR Zone Fuel Mass
evolu(evol).ign_loc(count).cdata(:)= find(phi_frame_ign(:, :, 40)>phi_low &
phi_frame_ign(:, :, 40)<phi_high);
evolu(evol).v_cell_ign_loc(count).cdata(:)=v_cellframe_col(evolu(evol).ign_loc(count).cdata(:))
;
evolu(evol).rho_fuel_ign_loc(count).cdata(:)=rho_fuelframe_col(evolu(evol).ign_loc(count).cdata(:));
evolu(evol).rho_air_ign_loc(count).cdata(:)=rho_airframe_col(evolu(evol).ign_loc(count).cdata(:));
evolu(evol).phi_ign_unweight(count).cdata(:)=phi_frame_ign40(phi_frame_ign40_col>phi_low
& phi_frame_ign40_col<phi_high);

evolu(evol).A_ign(count).cdata(:)=AF_s/evolu(evol).phi_ign_unweight(count).cdata(:);
evolu(evol).B_ign(count).cdata(:)=evolu(evol).A_ign(count).cdata(:)./
evolu(evol).rho_air_ign_loc(count).cdata(:);
evolu(evol).C_ign(count).cdata(:)=1./ evolu(evol).rho_fuel_ign_loc(count).cdata(:);
evolu(evol).Mf_ign_weight(count).cdata(:)=evolu(evol).v_cell_ign_loc(count).cdata(:)/(evolu(
evol).C_ign(count).cdata(:)+evolu(evol).B_ign(count).cdata(:))*10^6;

evolu(evol).sum_Mf_pen_weight(count).cdata(:)=sum(evolu(evol).Mf_pen_weight(count).cdata(
:));
evolu(evol).sum_Mf_ign_weight(count).cdata(:)=sum(evolu(evol).Mf_ign_weight(count).cdata(
:));

end
    pause(.1)
% Summing the Fuel Mass in each equivalence ratio step

```

```

for ii=1:length(Test)
Y_pen(ii,evol)=evolu(evol).sum_Mf_pen_weight(ii).cdata(:);
X_pen(ii,evol)=evolu(evol).test(ii).cdata(:);

Y_ign(ii,evol)=evolu(evol).sum_Mf_ign_weight(ii).cdata(:);
X_ign(ii,evol)=evolu(evol).test(ii).cdata(:);
end
subplot(2,2,1)
axis equal;
Contours=logspace(log(.1)/log(10),...
    log(100)/log(10),20);
contourf(log(phi_max_pen(:,evol)),log(Contours),'edgecolor','none');
colorbar('Ytick',log(Contours(2:2:end)),'Yticklabel',Contours(2:2:end)); colormap(jet);
set(gca, 'XTick', [10 20 30 40 50 60]*px_per_mm)
set(gca, 'XTickLabel', [10 20 30 40 50 60])
set(gca, 'YTick', importsettings.injectortip(2) + [-10 -5 0 5 10]*px_per_mm)
set(gca, 'YTickLabel', [-10 -5 0 5 10])
ylabel('Radial distance [mm]')
xlabel('Axial Position [mm]')
title('Phi Contour')
subplot(2,2,2)
plot(X_pen(:,evol),Y_pen(:,evol)), xlabel('Phi'), ylabel('Fuel Mass (mg)'), xlim([0 20]), ylim([0
2]), title('Phi-Mass Evolution')

end
if(saveoutvideo==1)
    close(v);
end

%% Get T_reaction from phi ignition zone by interpolating with T_eq and phi_eq
mass_frame_ign40=mass_fuel_weight_ign(:,:,40);
mass_frame_ign40_col=mass_frame_ign40(:);

% Organizing Equivalence Ratio, Mixture Temperature, and Fuel Mass into similar formats for
Tecplot
[x_lean, loc]=find(0.1037<phi_frame_ign40_col & phi_frame_ign40_col<1.2257); %to make all
points unique before interpolating
[x_rich, loc]=find(1.2257<phi_frame_ign40_col & phi_frame_ign40_col<5);
phi_frame40_lean=phi_frame_ign40_col(x_lean);
phi_frame40_rich=phi_frame_ign40_col(x_rich);
T_frame40_lean=T_frame_ign40_col(x_lean);
T_frame40_rich=T_frame_ign40_col(x_rich);
mass_frame40_lean=mass_frame_ign40_col(x_lean);
mass_frame40_rich=mass_frame_ign40_col(x_rich);
phi_cloudy=[phi_frame40_lean;phi_frame40_rich];
T_cloudy=[T_frame40_lean;T_frame40_rich];

```

```

mass_cloudy=[mass_frame40_lean;mass_frame40_rich];
phi_flame_lean=phi_eq(1:110,:); T_flame_lean=T_eq(1:110,:);
phi_flame_rich=phi_eq(111:end,:); T_flame_rich=T_eq(111:end,:);
smthphi_lean=smooth(phi_flame_lean);
smthT_lean=smooth(T_flame_lean);
smthphi_rich=smooth(phi_flame_rich);
smthT_rich=smooth(T_flame_rich);
T_reactlean=interp1(smthphi_lean,smthT_lean,phi_frame40_lean); %interpolating Chemkin
values to apply to entire LTHR zone phi
T_reactrich=interp1(smthphi_rich,smthT_rich,phi_frame40_rich);
T_react=[T_reactlean;T_reactrich];
[rid, loc]=find(isnan(T_react));
T_react(rid)=0;
T_cloudy(rid)=0;
phi_cloudy(rid)=0;
T_react_tec=reshape(T_react,2276,2);
phi_tec=reshape(phi_cloudy,2276,2);
T_tec=reshape(T_cloudy,2276,2);
mass_tec=reshape(mass_cloudy,2276,2);

```

#### %% Mass-Phi Plots with filters

```

ex40=fir1(64,.3);ex28=fir1(64,.3);ex16=fir1(64,.3);exign=fir1(64,.3);
Y_ign(isnan(Y_ign))=0;
filter40=filtfilt(ex40,1,Y_pen(:,40));
filter28=filtfilt(ex28,1,Y_pen(:,28));
filter16=filtfilt(ex16,1,Y_pen(:,16));
filterign=filtfilt(exign,1,Y_ign(:,40));

```

#### % Add (0,0) to beginning

```

X_pen40shift=X_pen(4:end,40);X_pen28shift=X_pen(4:end,28);X_pen16shift=X_pen(4:end,16)
;X_penignshift=X_ign(4:end,40);
Y_pen40shift=Y_pen(4:end,40);Y_pen28shift=Y_pen(4:end,28);Y_pen16shift=Y_pen(4:end,16)
;Y_penignshift=Y_ign(4:end,40);
filter_shift40=filtfilt(ex40,1,Y_pen40shift); filter0_shift40=[0;filter_shift40];
filter_shift28=filtfilt(ex28,1,Y_pen28shift); filter0_shift28=[0;filter_shift28];
filter_shift16=filtfilt(ex16,1,Y_pen16shift);filter0_shift16=[0;filter_shift16];
filter_shiftign=filtfilt(exign,1,Y_penignshift);filter0_shiftign=[0;filter_shiftign];

```

```

X0_pen40=[0;X_pen40shift];X0_pen28=[0;X_pen28shift];X0_pen16=[0;X_pen16shift];X0_pen
ign=[0;X_penignshift];
Y0_pen40=[0;Y_pen40shift];Y0_pen28=[0;Y_pen28shift];Y0_pen16=[0;Y_pen16shift];Y0_pen
ign=[0;Y_penignshift];
clf;
figure(93)
plot(X0_pen40,Y0_pen40,'--b'); hold on

```

```
plot(X0_pen28,Y0_pen28,'--k')
plot(X0_pen16,Y0_pen16,'--g')
plot(X0_penign,Y0_penign,'--c')
plot(X0_pen40,filter0_shift40,'b')
plot(X0_pen28,filter0_shift28,'k')
plot(X0_pen16,filter0_shift16,'g')
plot(X0_penign,filter0_shiftign,'c')
hold off
```

```
figure(94)
plot(X_pen(:,40),Y_pen(:,40),'--b');hold on
plot(X_pen(:,28),Y_pen(:,28),'--k')
plot(X_pen(:,16),Y_pen(:,16),'--g')
plot(X_ign(:,40),Y_ign(:,40),'--c')
plot(X_pen(:,40),filter40,'b')
plot(X_pen(:,28),filter28,'k')
plot(X_pen(:,16),filter16,'g')
plot(X_ign(:,40),filterign,'c')
hold off
```

## APPENDIX D

### MATLAB TO TECPLOT

Once the calculations have been completed, the data is exported to Tecplot to generate the figures displayed in the results section. The Matlab code representing this process is shown in this section.

```
%% Fuel Mass vs Equivalence Ratio
edata=[];
edata.Nvar=3;
edata.varnames={'Phi','Original Fuel Mass (mg)','Filtered Fuel Mass (mg)'};
edata.lines(1).zonename='Frame 40';
edata.lines(1).x=X_pen(:,40);
edata.lines(1).y=Y_pen(:,40);
edata.lines(1).z=filter40;
edata.lines(2).zonename='Frame 28';
edata.lines(2).x=X_pen(:,28);
edata.lines(2).y=Y_pen(:,28);
edata.lines(2).z=filter28;
edata.lines(3).zonename='Frame 16';
edata.lines(3).x=X_pen(:,16);
edata.lines(3).y=Y_pen(:,16);
edata.lines(3).z=filter16;
edata.lines(4).zonename=' LTHR Zone';
edata.lines(4).x=X_ign(:,40);
edata.lines(4).y=Y_ign(:,40);
edata.lines(4).z=filterign;
%
mat2tecplot(edata,'Mass-Phi Frames 16-40.plt')

zdata=[];
zdata.Nvar=3;
zdata.varnames={'Phi','Original Fuel Mass (mg)','Filtered Fuel Mass (mg)'};
zdata.lines(1).zonename='Frame 40';
zdata.lines(1).x=X0_pen40;
zdata.lines(1).y=Y0_pen40;
zdata.lines(1).z=filter0_shift40;
```

```

zdata.lines(2).zonename='Frame 28';
zdata.lines(2).x=X0_pen28;zdata.lines(2).y=Y0_pen28;
zdata.lines(2).z=filter0_shift28;
zdata.lines(3).zonename='Frame 16';
zdata.lines(3).x=X0_pen16;
zdata.lines(3).y=Y0_pen16;
zdata.lines(3).z=filter0_shift16;
zdata.lines(4).zonename=' LTHR Zone';
zdata.lines(4).x=X0_penign;
zdata.lines(4).y=Y0_penign;
zdata.lines(4).z=filter0_shiftign;
%
mat2tecplot(zdata,'Mass-Phi Frames 16-40 Zero Shift.plt')

%%Phi-T Contours
X_mesh1=(1:1:608)-importsettings.injectortip(1))*1/importsettings.px_per_mm;
Y_mesh1=(1:1:200]-center_new))*1/importsettings.px_per_mm;
[X_mesh, Y_mesh]=meshgrid(X_mesh1, Y_mesh1);
igndata=[];
igndata.Nvar=3;
igndata.varnames={'Axial Distance','Radial Distance', 'Phi'};
igndata-surfaces(1).zonename=' LTHR Region';
igndata-surfaces(1).x= X_mesh;
igndata-surfaces(1).y=Y_mesh;
igndata-surfaces(1).z=phi_frame_ign(:,:,40);
mat2tecplot(igndata,'Phi-T Ignition Contours.plt')

%%Equivalence Ratio Contours
X_mesh1=(1:1:608]-importsettings.injectortip(1))*1/importsettings.px_per_mm;
Y_mesh1=(1:1:200]-center_new))*1/importsettings.px_per_mm;
[X_mesh, Y_mesh]=meshgrid(X_mesh1, Y_mesh1);
igndata=[];
igndata.Nvar=3;
igndata.varnames={'Axial Distance','Radial Distance', 'Phi'};
igndata-surfaces(1).zonename=' LTHR Region';
igndata-surfaces(1).x= X_mesh;
igndata-surfaces(1).y=Y_mesh;
igndata-surfaces(1).z=phi_frame_ign(:,:,40);
mat2tecplot(igndata,'Phi-T Ignition Contours.plt')

X_mesh1=(1:1:608]-importsettings.injectortip(1))*1/importsettings.px_per_mm;
Y_mesh1=(1:1:200]-center_new))*1/importsettings.px_per_mm;
[X_mesh, Y_mesh]=meshgrid(X_mesh1, Y_mesh1);
igndata=[];

```

```

igndata.Nvar=3;
igndata.varnames={'Axial Distance','Radial Distance', 'Phi'};
igndata-surfaces(1).zonename='Frame 16';
igndata-surfaces(1).x= X_mesh;
igndata-surfaces(1).y=Y_mesh;
igndata-surfaces(1).z=phi_max_pen(:, :, 16);
mat2tecplot(igndata, 'Frame 16 Phi-T Contour.plt')

```

```

X_mesh1=( [1:1:608]-importsettings.injectortip(1))*1/importsettings.px_per_mm;
Y_mesh1=( [1:1:200]-center_new)*1/importsettings.px_per_mm;
[X_mesh, Y_mesh]=meshgrid(X_mesh1, Y_mesh1);
igndata=[];
igndata.Nvar=3;
igndata.varnames={'Axial Distance','Radial Distance', 'Phi'};
igndata-surfaces(1).zonename='Frame 28';
igndata-surfaces(1).x= X_mesh;
igndata-surfaces(1).y=Y_mesh;
igndata-surfaces(1).z=phi_max_pen(:, :, 28);
mat2tecplot(igndata, 'Frame 28 Phi-T Contour.plt')

```

```

X_mesh1=( [1:1:608]-importsettings.injectortip(1))*1/importsettings.px_per_mm;
Y_mesh1=( [1:1:200]-center_new)*1/importsettings.px_per_mm;
[X_mesh, Y_mesh]=meshgrid(X_mesh1, Y_mesh1);
igndata=[];
igndata.Nvar=3;
igndata.varnames={'Axial Distance','Radial Distance', 'Phi'};
igndata-surfaces(1).zonename='Frame 40';
igndata-surfaces(1).x= X_mesh;
igndata-surfaces(1).y=Y_mesh;
igndata-surfaces(1).z=phi_max_pen(:, :, 40);
mat2tecplot(igndata, 'Frame 40 Phi-T Contour.plt')

```

```

X_mesh1=( [1:1:608]-importsettings.injectortip(1))*1/importsettings.px_per_mm;
Y_mesh1=( [1:1:200]-center_new)*1/importsettings.px_per_mm;
[X_mesh, Y_mesh]=meshgrid(X_mesh1, Y_mesh1);
igndata=[];
igndata.Nvar=3;
igndata.varnames={'Axial Distance','Radial Distance', 'Phi'};
igndata-surfaces(1).zonename='Frame 40';
igndata-surfaces(1).x= X_mesh;
igndata-surfaces(1).y=Y_mesh;
igndata-surfaces(1).z=phi_max_pen(:, :, 57);
mat2tecplot(igndata, 'Frame 57 Phi-T Contour.plt')

```

%% Temperature Contours

```

X_mesh1=( [1:1:608]-importsettings.injectortip(1))*1/importsettings.px_per_mm;

```

```

Y_mesh1=(1:1:200)-center_new)*1/importsettings.px_per_mm;
[X_mesh, Y_mesh]=meshgrid(X_mesh1, Y_mesh1);
igndata=[];
igndata.Nvar=3;
igndata.varnames={'Axial Distance','Radial Distance', 'Temperature (K)'};
igndata-surfaces(1).zonename='Frame 16';
igndata-surfaces(1).x= X_mesh;
igndata-surfaces(1).y=Y_mesh;
igndata-surfaces(1).z=T_max_pen(:,,16);
mat2tecplot(igndata,'Frame 16 Temp Contour.plt')

X_mesh1=(1:1:608]-importsettings.injectortip(1))*1/importsettings.px_per_mm;
Y_mesh1=(1:1:200]-center_new)*1/importsettings.px_per_mm;
[X_mesh, Y_mesh]=meshgrid(X_mesh1, Y_mesh1);
igndata=[];
igndata.Nvar=3;
igndata.varnames={'Axial Distance','Radial Distance', 'Temperature (K)'};
igndata-surfaces(1).zonename='Frame 28';
igndata-surfaces(1).x= X_mesh;
igndata-surfaces(1).y=Y_mesh;
igndata-surfaces(1).z=T_max_pen(:,,28);
mat2tecplot(igndata,'Frame 28 Temp Contour.plt')

X_mesh1=(1:1:608]-importsettings.injectortip(1))*1/importsettings.px_per_mm;
Y_mesh1=(1:1:200]-center_new)*1/importsettings.px_per_mm;
[X_mesh, Y_mesh]=meshgrid(X_mesh1, Y_mesh1);
igndata=[];
igndata.Nvar=3;
igndata.varnames={'Axial Distance','Radial Distance', 'Temperature (K)'};
igndata-surfaces(1).zonename='Frame 40';
igndata-surfaces(1).x= X_mesh;
igndata-surfaces(1).y=Y_mesh;
igndata-surfaces(1).z=T_max_pen(:,,40);
mat2tecplot(igndata,'Frame 40 Temp Contour.plt')

X_mesh1=(1:1:608]-importsettings.injectortip(1))*1/importsettings.px_per_mm;
Y_mesh1=(1:1:200]-center_new)*1/importsettings.px_per_mm;
[X_mesh, Y_mesh]=meshgrid(X_mesh1, Y_mesh1);
igndata=[];
igndata.Nvar=3;
igndata.varnames={'Axial Distance','Radial Distance', 'Temperature (K)'};
igndata-surfaces(1).zonename='T Ignition Region';
igndata-surfaces(1).x= X_mesh;
igndata-surfaces(1).y=Y_mesh;
igndata-surfaces(1).z=T_frame_ign(:,,40);
mat2tecplot(igndata,'Temperature Ignition Contours.plt')

```

```

X_mesh1=(1:1:608)-importsettings.injectortip(1))*1/importsettings.px_per_mm;
Y_mesh1=(1:1:200]-center_new)*1/importsettings.px_per_mm;
[X_mesh, Y_mesh]=meshgrid(X_mesh1, Y_mesh1);
igndata=[];
igndata.Nvar=3;
igndata.varnames={'Axial Distance','Radial Distance', 'Temperature (K)'};
igndata-surfaces(1).zonename='Frame 40';
igndata-surfaces(1).x= X_mesh;
igndata-surfaces(1).y=Y_mesh;
igndata-surfaces(1).z=T_max_pen(:, :,57);
mat2tecplot(igndata,'Frame 57 Temp Contour.plt')

```

### %Fuel Mass vs Equivalence Ratio

```

philow=.25;
phihigh=5;
phistep=.1;
phi_step=.10;

Tlow=400;
Thigh=850;
Tstep=8.65;

T_low=400;
T_high=3000;
T_step=25;

phibins=[philow:phistep:phihigh];
Tbins=[Tlow:Tstep:Thigh];

Tbins1=[T_low:T_step:T_high];
phibins1=[philow:phi_step:phihigh];

figure(1);
clf;
tic
for frame=40:40
    Tplot=Tmix(:, :,frame);
    phiplot=phi(:, :,frame);
    Tplotign=T_frame_ign(:, :,frame);
    phiplotign=phi_frame_ign(:, :,frame);

```

```
[weighthemfigndata]=phiTmassdistributionign(phiplotign,Tplotign,mass_fuel_weight_ign(:, :, frame),phibins,Tbins);
```

```
[weigthedmfdata]=phiTmassdistributionign(phi_tec(:, :),T_react_tec(:, :),mass_tec(:, :),phibins1,Tbins1);
```

```
filtered_weigthedmfdata=imgaussfilt(weigthedmfdata,1.2);
```

```
frame
```

```
figure(1)
```

```
contourf(log(Tbins),log(phibins),imgaussfilt(weighthemfigndata,1.5), 'LineColor','none');
```

```
colorbar
```

```
colormap('jet')
```

```
caxis([0 .2]);
```

```
pause(0.1)
```

```
figure(2)
```

```
contourf(Tbins1,phibins1,weigthedmfdata, 'LineColor','none');
```

```
colorbar
```

```
colormap('jet')
```

```
caxis([0 .2]);
```

```
figure(3)
```

```
contourf(Tbins1,phibins1,filtered_weigthedmfdata, 'LineColor','none');
```

```
colorbar
```

```
colormap('jet')
```

```
caxis([0 .1]);
```

```
pause(0.1)
```

```
end
```

```
toc
```

### %%Fuel Mass Concentration Contours

```
[T_bins, phi_bins]=meshgrid(Tbins,phibins);
```

```
clouddata=[];
```

```
clouddata.Nvar=3;
```

```
clouddata.varnames={'Temperature (K)', 'Equivalence Ratio', 'Fuel Mass (mg)'};
```

```
clouddata-surfaces(1).zonename='Frame 16 mass';
```

```
clouddata-surfaces(1).x= T_bins;
```

```
clouddata-surfaces(1).y= phi_bins;
```

```
clouddata-surfaces(1).z=imgaussfilt(weigthedmfdata,2);
```

```
mat2tecplot(clouddata, 'Frame 16 Mass Cloudplot.plt')
```

```
%
```

```
[T_bins, phi_bins]=meshgrid(Tbins,phibins);
```

```
clouddata=[];
```

```
clouddata.Nvar=3;
```

```
clouddata.varnames={'Temperature (K)', 'Equivalence Ratio', 'Fuel Mass (mg)'};
```

```
clouddata-surfaces(1).zonename='Frame 28 mass';
```

```

clouddata-surfaces(1).x= T_bins;
clouddata-surfaces(1).y= phi_bins;
clouddata-surfaces(1).z=imgaussfilt(weigthedmfddata,2);
mat2tecplot(clouddata,'Frame 28 Mass Cloudplot filt.plt')

```

```

[T_bins, phi_bins]=meshgrid(Tbins,phibins);
clouddata=[];
clouddata.Nvar=3;
clouddata.varnames={'Temperature (K)', 'Equivalence Ratio', 'Fuel Mass (mg)'};
clouddata-surfaces(1).zonename='Frame 40 mass';
clouddata-surfaces(1).x= T_bins;
clouddata-surfaces(1).y= phi_bins;
clouddata-surfaces(1).z=imgaussfilt(weigthedmfddata,2);
mat2tecplot(clouddata,'Frame 40 Mass filt Cloudplot.plt')

```

```

[T_bins, phi_bins]=meshgrid(Tbins,phibins);
[T_bins1,phi_bins1]=meshgrid(Tbins1,phibins1);
clouddata=[];
clouddata.Nvar=3;
clouddata.varnames={'Temperature (K)', 'Equivalence Ratio', 'Fuel Mass (mg)'};
clouddata-surfaces(1).zonename=' LTHR Zone mass';
clouddata-surfaces(1).x= T_bins1;
clouddata-surfaces(1).y= phi_bins1;
clouddata-surfaces(1).z=imgaussfilt(weigthedmfddata,1.5);

```

```

clouddata-surfaces(2).zonename=' LTHR Zone reacted mass';
clouddata-surfaces(2).x= T_bins;
clouddata-surfaces(2).y= phi_bins;
clouddata-surfaces(2).z=imgaussfilt(weighthemfigndata,1.5);
mat2tecplot(clouddata,'Pract LTHR Zone react Mass diff Cloudplot.plt')

```

```

[T_bins, phi_bins]=meshgrid(Tbins,phibins);
clouddata=[];
clouddata.Nvar=3;
clouddata.varnames={'Temperature (K)', 'Equivalence Ratio', 'Fuel Mass (mg)'};
clouddata-surfaces(1).zonename='Frame 28 mass';
clouddata-surfaces(1).x= T_eq;
clouddata-surfaces(1).y= phi_eq;
clouddata-surfaces(1).z=imgaussfilt(weigthedmfigndata,2);
mat2tecplot(clouddata,'Reacted filt.plt')

```

## APPENDIX E

### FILTER CALIBRATION

This section contains the experimental information and code used to generate the calibration curve in Figure 2.6.

```
case 2
%% filenames
importsettings.vidfileName='550C_30bar_40k_3us.cine';
importsettings.filtercalfileName='calibration_5mm_20k.cine.mat';

importsettings.deltoxfcalfile='heptane_Tamb_833K_Pamb_2.8MPa_Tfin_363K_calibration.mat'
;

%% frame read range, injection count, etc.
importsettings.startframe=1;
importsettings.endframe=100;
importsettings.framestep=1;
importsettings.nInjectionstot=50;
importsettings.nInjectionsread=50;
importsettings.skipinjections=[2];
importsettings.SOIframe=10;
importsettings.startframesteadyll=38;
importsettings.endframesteadyll=53;
importsettings.period=25; %us
importsettings.numberofframestoread=cast((importsettings.endframe-
importsettings.startframe+1)/importsettings.framestep,'uint16');

%% data storage and threshold options
importsettings.storeshift=1;
importsettings.satthreshold =.01; %the higher the threshold the more color points in the
spray (red in the core)% throws it way not saturated enough too grayscale
importsettings.valthreshold=0.15; %higher value means darker liq core and tc appearance %
throws it away if dark this accounts for light not penetrating liquid medium in the very dense
region the Signal to Noise ratio is too low
```

```

%% thermodynamic conditions
importsettings.P_chamb = 2800; %kPa
importsettings.T_chamb = 550+273; %K
importsettings.T_fuel=90+273;

```

```

%% geometry of injection, optics, filters
importsettings.injectortip=[12,94];
importsettings.px_per_mm= 9.44;
importsettings.focalLength = 250; % mm
importsettings.filterasym=0;
importsettings.filtersize_mm=5;
importsettings.startaxialshift=25;

```

## %% Calibration Code

```

clearvars
tic
ii = 2;
ifsave = 1;
Case = {'5mm'};
[importsettings] = ImportSettingsSetupCalibration(ii);
[rawdata,importsettingsout,vidheader] = readRSDcine(importsettings,0);
[vidHeight,vidWidth,~,~] = size(rawdata);
%%

calibrationrows=100;
calibrationcols=100;
hue = zeros(calibrationrows+1,calibrationcols+1,importsettings.numberofframestoread);
frames = importsettings.numberofframestoread;
filtersize = importsettings.filtersize_mm;
for i=1:frames
    Image = rgb2hsv(rawdata(:,:,i));
    hue(:,:,i) = Image(round(vidHeight/2-...
        calibrationrows/2:vidHeight/2+calibrationrows/2),...
        round(vidWidth/2-calibrationcols/2:vidWidth/2+...
        calibrationcols/2),1)*360;
    huebox = hue(:,:,i);
    if i>(frames/2-20)&&i<=(frames/2+20)
        hueFinal(i) = mean(huebox(huebox>0&huebox<150));
        hueDev(i)=2*std(huebox(huebox>0&huebox<200));
    else
        hueFinal(i) = mean(huebox(huebox>20&huebox<300));
    end
end

```

```

        hueDev(i)=2*std(std(huebox(huebox>20&huebox<300)));
    end
end
%%
figure
hold on
plot(hueFinal)
plot(12,hueFinal(12),'rx')
plot(numel(hueFinal)-2,hueFinal(end-2),'rx')
%%
hueDev(1:10)=[];
hueDev(end)=[];
hueFinal(1:10)=[];
hueFinal(end)=[];
locfinal = linspace(-filtersize/2,filtersize/2,numel(hueFinal));
figure
plot(locfinal,hueFinal)
hue1 = hueFinal(1:numel(hueFinal)/2);
hue2 = hueFinal(numel(hueFinal)/2+1:end);
hue1 = fliplr(hue1);
hueDev1 = hueDev(1:numel(hueFinal)/2);
hueDev2 = hueDev(numel(hueFinal)/2+1:end);
hueDev1 = fliplr(hueDev1);
huefinal = (hue1+hue2)/2;
hueDev = (hueDev1+hueDev2)/2;
locfinal(1:numel(hueFinal)/2)=[];
figure
hold on
plot(hue1)
plot(hue2)
figure
plot(locfinal,huefinal)
%%
figure
errorbar(locfinal,huefinal,hueDev)
%%

locfinal(1:7)=[];
locfinal = locfinal-locfinal(1);
huefinal(1:7)=[];
hueDev(1:7)=[];
%%
figure
errorbar(locfinal,huefinal,hueDev,'bs')
ylabel('Hue (degree)');

```

```
xlabel('Displacement from center (mm)');
ylim([0 350])
xlim([0 locfinal(end)])
minhue = min(huefinal);
maxhue = max(huefinal);

filename = sprintf('%s%s',Case{ii},'.mat');
toc
%%
if ifsave==1
    save(filename,'locfinal','huedev','huefinal','maxhue','minhue')
end
```